AN EXPERIMENTAL INVESTIGATION OF THE EFFECTS OF INLET RADIAL TEMPERATURE PROFILES ON THE AERODYNAMIC PERFORMANCE OF A TRANSONIC TURBINE STAGE

by

Louis N. Cattafesta, III

B.S.M.E., Pennsylvania State University (1986)

SUBMITTED IN PARTIAL FULFILLMENT

OF THE REQUIREMENTS OF THE

DEGREE OF

MASTER OF SCIENCE

IN AERONAUTICS AND ASTRONAUTICS

at the

MASSACHUSETTS INSTITUTE OF TECHNOLOGY

August 1988

© Massachusetts Institute of Technology, 1988

Signature of Author _____
Department of Aeronautics and Astronautics
August 4, 1988

Certified by _____
Professor Alan H. Epstein
Thesis Supervisor
Department of Aeronautics and Astronautics

Accepted by _____
Professor Harold Y. Wachman
Chairman, Departmental Graduate Committee

MASSACHUSETTS INSTITUTE OF TECHNOLOGY
SEP 07 1988
LIBRARIES

WITHDRAWN
M.I.T.
LIBRARIES

An Experimental Investigation of the Effects of Inlet Radial Temperature Profiles on the Aerodynamic Performance of a Transonic Turbine Stage

by

Louis N. Cattafesta, III

Submitted to the Department of Aeronautics and Astronautics
on August 3, 1988 in partial fulfillment of the
requirements for the degree of Master of Science in
Aeronautics and Astronautics

Abstract

This work describes an experimental effort to investigate the effects of inlet radial temperature profiles on the aerodynamic performance of a transonic turbine stage. The thesis consists of two parts. First, the probe designs to make accurate measurements of total pressure and total temperature in a short duration turbomachinery test facility, the MIT Blowdown Turbine (BDT), are described. The BDT, which rigorously simulates the operational environment of current and future engines, can significantly reduce the cost of performance testing due to its short test time (0.5 sec). Performance testing in the BDT, however, places strict requirements on the accuracy and frequency response of the probes. The design of a vented kiel-head total pressure rake is described which uses externally mounted Kulite strain gauge type differential pressure transducers. The probe is shown to have more than adequate frequency response (1 atm step input response of 25 msec) and accuracy of approximately 0.7% for this application. In addition, the design of two vented kiel-head total temperature rakes are described which use 20 μm diameter by 2.5 μm thick type K thermocouple disc junctions on 50 L/D quartz insulated supports. The rakes use AD597AH preamps for electronic ice point compensation and amplification, and are electrically heated to the approximate gas temperature to reduce the conduction error of the probe. A temperature probe model is developed, validated, and used to determine the accuracy and time response of the probes (approximately 0.12% in under 400 msec). An error analysis is also performed which shows that the net uncertainty in efficiency measurement is $\sim$ 0.85%. Techniques for reducing this uncertainty level are also discussed.

Second, the effects of inlet radial temperature profiles on stage efficiency are discussed. The design of a heat exchanger which is capable of producing both axisymmetric and skewed inlet radial temperature profiles is described. Seven tests in the BDT, which was configured with a 0.5 m diameter, high pressure, transonic turbine stage, were successfully carried out at the design corrected flow with different corrected speeds and levels of axisymmetric inlet temperature distortion. A comparison between two cases with identical corrected conditions but different inlet temperature profiles (15.2% compared to 9.8%) revealed that the case with the larger profile had a 2.0% higher efficiency. Two other cases which had lower corrected speeds and larger temperature profiles also showed increases in stage efficiency but were lower than the 0.85% uncertainty estimate.

Thesis Supervisor: Dr. Alan H. Epstein
Title: Associate Professor of Aeronautics and Astronautics

ACKNOWLEDGEMENTS

Having completed this work, I am deeply indebted to many people for their contributions. Therefore, I would like to take this opportunity to offer my sincerest thanks to those people (at least the ones I could remember). First, I would like to offer my appreciation to the Air Force, General Electric, and MIT for the opportunity to study and work under the assistance of the Air Force Research in Aero-Propulsion Technology (AFRAPT) Fellowship. I would like to especiallly thank Professor Epstein for his helpful guidance and advice. He gave me an appreciation for learning things by trying instead of being shown how. I owe a tremendous amount of thanks to the Blowdown Turbine crew for their instruction, patience, and camaraderie: Professor Epstein, Dr. Gerry Guenette, Mr. Charlie Haldeman, Mr. Reza Abhari, and Mr. Andrew Thurling. In addition, I would like to thank Mr. Jim Nash, Mr. Roy Andrews, and Mr. Victor Dubrowski for the lab survival skills they taught me. Special thanks goes to Mr. John Stanley for his assistance with the total temperature probes. I would like to thank Mr. Andy Thurling for his general assistance with the assorted electronic tasks. I also would like to thank Dr. Guenette, Prof. Greitzer, and Dr. Choon Tan for their many helpful comments, and Mr. Bob Haimes and Ms. Dianna Park for their computer aid. In particular, Dr. Guenette's critique of my thesis was very helpful. Others who were part of "LOU AID" and deserve thanks: Dr. Phil Lavrich, Mr. Petros Kotidis, Mr. Yi-Lung Yang, Mr. Gwo-Tung Chen, and Mr. Andy Crook.

On a personal note, I would like to thank my parents for their love and guidance through the years. Most importantly, I would like to dedicate this work to my wife, Carolyn, who helps me keep everything in proper perspective. Her unwavering love and support are more than I deserve.

TABLE OF CONTENTS

LIST OF FIGURES

LIST OF TABLES

Chapter 1 - Introduction

The aircraft gas turbine engine is a tremendously complex system which is composed of many subsystems. Together, these subsystems push the state of the art in many engineering disciplines such as fluid mechanics, heat transfer, stuctural dynamics, controls, etc. As one might expect, such a device has many difficult problems associated with it. This thesis deals with one such subsystem, the high pressure axial turbine stage, and two problems associated with it : steady state aerodynamic performance measurements in a short duration test facility and the investigation of the effects of inlet radial temperature profiles on the stage efficiency. This chapter states the objectives of the thesis and provides some relevant background information.

1.1 - Thesis Objectives

This thesis has four objectives. First, total pressure rake designs are described for steady state aerodynamic performance measurements in the MIT Blowdown Turbine Facility (BDT). The second objective is to describe how accurate measurements of gas total temperature in short duration facilities such as the BDT can be obtained. Third, an error analysis is performed to determine the relative importance of temperature, pressure, and ratio of specific heats in the calculation of stage efficiency. In addition, the error analysis provides the total uncertainty in the calculations. Finally, the effects of inlet radial temperature profiles on the turbine efficiency are presented.

1.2 – Background

1.2.1 – Use of Short Duration Facilities for Performance Testing

As discussed in [1], full-scale testing of an engine component is sometimes necessary and, unfortunately, extremely expensive. The reason for the necessity is that some problems in turbomachinery are not amenable to isolated studies. In a transonic turbine, for example, this is due in part to the presence of shock waves, blade wakes, and secondary flows. Since these interactions are coupled in some sense, it is difficult to separate the effects of one phenomenon from another. Therefore, full-scale tests sometimes become necessary.

Cost scales with the mass flow of the machine and, therefore, its size. Large machines are desirable in order to resolve flow details such as boundary layers and blade wakes and to minimize intrusive probe interference. In addition to size, cost is also proportional to the length of the test time. It is precisely this point which short duration test facilities, such as the BDT [1], capitalize on. They reduce cost by minimizing the test time, not the scale of the experiment.

How long should a test last? Certainly, it should be long enough so that steady state conditions are established and maintained for a period of time. In general, the steady state period should be long enough so that a sufficient number of data points are sampled to be statistically relevant. As far as aerodynamic performance measurments are concerned, the relevant nondimensional parameters should remain nearly constant over the test time: Reynolds number, corrected flow (i.e. axial Mach number), corrected speed (i.e. tip Mach number), and ratio of specific heats. For the BDT, which has a blade passing frequency of 6 kHz and a test time of 300 msec (250 msec – 550 msec), this translates to 1800 blade passings and 3750 data points per low speed

channel (for a 12.5 kHz sampling frequency). This is more than enough for time-averaged total pressure and total temperature measurements, putting aside the question of probe frequency response for now.

1.2.2 – Description of the MIT Blowdown Turbine Facility

A brief description of the BDT is given here, but a more detailed account of the BDT is given in [2]. The BDT is a short duration (0.3 sec) test facility capable of testing a 0.5 meter diameter high-pressure, film-cooled, transonic turbine stage with nozzle guide vanes (NGV's) under conditions which rigorously simulate the actual engine operating environment. The facility matches the nondimensional parameters known to be important to turbine heat transfer and fluid mechanics such as the Reynolds number based on axial chord, Mach number, gas to metal temperature ratios, ratio of specific heats, and Prandtl number.

The tunnel uses an Argon – Freon 12 mixture to obtain the required ratio of specific heats. In addition, the Argon – Freon 12 mixture has a larger molecular weight than that of air. This has multiple benefits. First, the higher molecular weight results in a higher density fluid than air and reduces the pressure level in the supply tank required for Reynolds number similarity. Second, the high molecular weight reduces the speed of sound. This allows for lower rotational speeds for tip Mach number similarity. Also, the lower pressure level and tip speeds reduce the cost of the facility and the frequency response requirements of the instrumentation. Table 1.1 shows the BDT scaling.

Table 1.1 - MIT Blowdown Turbine Scaling

	Full Scale	MIT Blowdown
Fluid	Air	Argon-Freon12
Ratio of Specific Heats	1.27	1.27
Mean Metal Temperature, T_m	1118 K	295 K
Metal/Gas Temperature Ratio, T_m/T_g	0.63	0.63
Inlet Total Temperature, T_g	1780 K	478 K
Cooling Air Temperature	790 K	212 K
Airfoil Cooling Air Flow	12.5%	12.5%
True NGV Chord	8.0 cm	5.9 cm
Reynolds Number*	2.7×10^6	2.7×10^6
Inlet Total Pressure, psia	289	64
Outlet Total Pressure, psia	66	14.7
Outlet Total Temperature	1280 K	343 K
Prandtl Number	0.752	0.755
Rotor Speed, RPM	12,734	6,190
Mass Flow, kg/sec	49.00	16.55
Power, watts	24,880,000	1,078,000
Test Time	continuous	0.3 sec

*Based on NGV chord and isentropic exit conditions

Figure 1.1 shows an external view of the test facility. Essentially, the BDT consists of a supply tank which heats the pressurized gas mixture to its initial temperature, a large diameter valve which delivers smooth flow to the test section, a test section containing the NGV's and rotor, and a dump tank downstream of the test section. Figure 1.2 shows the the turbine facility flow path. Initially, the valve is closed and the tunnel is evacuated. The rotor is then spun up to its desired speed by a d.c. motor drive, and the valve is opened to deliver gas from the supply tank, which acts as a plenum, to the test section. A fraction of the fluid (approximately 30%) is scavenged off by the boundary layer bleeds before entering the NGV's. Once passing through the test section, the flow passes through a set of deswirl vanes and exhausts to the vacuum tank. The power produced by the turbine is absorbed by an eddy current brake whose braking power is set so that the turbine corrected speed is constant over the

test time.

There are six instrumentation window ports for access to the flow field. As shown in Figure 1.3 [3], there are upstream ports placed 9.5 cm upstream of the NGV leading edge (three ports equally spaced 120 degrees apart). In addition, there are three 13 cm wide windows which are equally spaced around the outer wall of the test section. Each window extends from upstream of the NGV's to 11 cm downstream of the rotor.

The BDT uses a high speed data acquisition system which consists of 45 high speed, 12 bit channels with maximum sampling frequencies of 200 kHz. In addition, there are eight groups of 16 low speed channels which are multiplexed from eight high speed channels. These channels, with a maximum sampling frequency of 16.5 kHz, are used for the total pressure and total temperature measurements to be described later. Four programmable clocks control the data sampling rate during the test time. The data is stored in a 32 megabyte solid state random access memory during the test. After the test, the data is downloaded to a host computer for data reduction and analysis.

1.2.3 – Instrumentation Requirements

In conventional test facilities, total temperature rakes and total pressure rakes are used to obtain steady state aerodynamic performance estimates. The same techniques can be employed in short duration facilities provided that care is taken to insure that the frequency response and accuracy of the probes are sufficient. In the BDT the total pressure probes must respond to step inputs in less than 250 msec (approximately 4.0 atmospheres upstream and 1.0 atmospheres downstream) with better than 1.0% accuracy. Similarly, the total temperature probes must respond to step inputs of approximately 178 K upstream and 43 K

downstream in the same time period to better than 0.25% accuracy. Chapter 4 explains why the measurement of total temperature is more crucial than total pressure as far as stage efficiency is concerned. If the natural frequency response and/or accuracy are insufficient, then some means of correction must be used to insure high quality performance estimates (i.e. 0.5%). This is the subject of Chapters 2 and 3.

Chapter 2 - Total Pressure Measurement

2.1 - Introduction

As stated in Chapter 1, aerodynamic performance estimation requires the measurement of total pressure. This usually entails some combination of single-sensor probes, rakes and traverses in the radial and circumferential directions. Some suitable averaging technique is then applied to the total pressure data in order to determine the inlet and exit conditions of the stage. In the BDT both high and low frequency response total pressure probes have been developed and successfully implemented [2], [3], and [4]. Therefore, the design of total pressure rakes for the purpose of measuring the time-averaged total pressure is merely an extension of previous work.

This chapter, then, has five objectives. First, the performance requirements of the total pressure probes are briefly stated. Second, the design of a total pressure rake for use downstream of the turbine stage is described (a six-head total pressure rake for use at the turbine inlet already existed). Third, the online calibration procedure is stated. Fourth, the subject of the frequency response of the probe is addressed briefly. Finally, the total uncertainty in the measurement is estimated.

2.2 - Requirements of the Total Pressure Probes

The total pressure probes are used to measure the time-averaged radial total pressure profiles at the inlet and the exit of the stage. The total pressure probes

are also needed to determine the stage pressure ratio for adiabatic efficiency calculations. It should be mentioned here that one of the guidelines of this work was to design total pressure rakes which are similar to those commonly employed in conventional test facilities. The reason for this is given below.

Some aspects of the total pressure measurement which are peculiar to the upstream and downstream rakes are worth noting. For example, the upstream probe will determine the uniformity of inlet conditions to the stage. This is important since the BDT has the capability of generating inlet radial temperature profiles using a heat exchanger. As explained in Chapter 5, the heat exchanger was designed to generate different levels of radial temperature profiles while providing the turbine with a uniform total pressure distribution [5]. The upstream probe, then, shows to what extent this is achieved. The downstream probe, however, is placed approximately four chord lengths from the rotor as in conventional tests. Because the velocity triangles are determined by the inlet conditions and the rotor speed (which will vary from test to test), the probe here must be insensitive to variations in flow direction.

2.3 – Downstream Total Pressure Probe Design

2.3.1 – Overview

This section describes the design of the downstream total pressure probe only, since the upstream probe had been designed, built, and tested previously. For purposes of illustration, however, Figure 2.1 shows the dimensions of the upstream probe. As one can see from the figure, there are six radial ports. The actual sensors used are mounted external to the tunnel on support brackets for strain relief. The sensors are Kulite Semiconductor 100 psi strain gauge type

differential pressure transducers and are temperature compensated over the 80 ^{o}F – 250 ^{o}F range (model no. XCQ–093–100 D).

As for the downstream probe, the concept behind the design was as follows: since conventional test facilities use impact total pressure rakes, it would be desirable to adapt their designs to the BDT. Consequently, the downstream rake was specifically designed using these standards a guide [6].

When designing the downstream total pressure probe, there are at least two major concerns: accuracy (typically better than 1.0%) and frequency response (must respond to step inputs on the order of 1 atm in less than 250 msec). The accuracy requirement is set by the uncertainty analysis for the adiabatic efficiency calculation. This is described in Chapter 4. The frequency response requirement is set by the environment in which the probe operates. Since the steady state test time is from 250 to 550 msec, the probe has until 250 msec for transients to die out. Initially the probe is in vacuum. When the valve opens and the flow is established (approximately 50 msec later), the probe sees a step input which decays exponentially. Since the transducers will be mounted outside the tunnel, where the environment is more benign and any maintenance is simplified, the dynamics of the flow in the tubes connecting the flowfield to transducer must be carefully considered [1], [7], [8]. These ideas are addressed further below in the sections on pressure uncertainty and frequency response.

2.3.2 – Probe Design Description

Figure 2.2 shows the dimensions of the downstream total pressure probe. The aerodynamically contoured probe body is 49.022 mm (1.93") long and has five ports which are placed at equal area locations. Thus, the probe area–averages the flowfield. Like the upstream probe, the sensors are Kulite Semiconductor

strain gauge type differential pressure transducers and are temperature compensated over the 80 ^{o}F - 250 ^{o}F range (model. no XCQ-093-50 D). The rated pressure of the transducers is 50 psi. Another important feature of the probe is its kiel head design which minimizes errors due to variations in flow angle, a key consideration downstream of a turbine stage. The accuracy specifications are claimed to be less than 1% of the dynamic head with flow incidence angles of up to 27^{o} [6]. It is of interest, then, to determine the nondimensional form of this error. Following the approach taken in [9] gives:

$$\frac{1}{2}\rho V^2 = \frac{1}{2}\rho M^2 a^2 \qquad (2.1)$$

In nondimensional form, this equation becomes:

$$\frac{\frac{1}{2}\rho V^2}{P_t} = \frac{\gamma M^2}{2\left(1 + \frac{\gamma-1}{2} M^2\right)^{\frac{\gamma}{\gamma-1}}} \qquad (2.2)$$

The nondimensional error, then, should be 1% of the value given by Eqn. 2.2. For the nominal conditions downstream of the turbine, M=0.6 and γ=1.28, this amounts to 0.184% of the total pressure. For conditions upstream of the turbine, M=0.0695, Eqn. 2.2 gives the value of the nondimensional error as 0.003%.

2.4 - Online Calibration Procedure

Obviously, some form of calibration procedure must be employed for the total pressure probes. The BDT has the capability for online calibrations just prior to or immediately after a test. This is important since transducer sensitivity and offset can drift with time. For the BDT, however, this problem is minimized by calibrating the transducers just minutes prior to testing. Therefore, transducer

drift from test to test is accounted for by the calibration. In addition, the short test time of the BDT also has the effect of reducing the extent to which the sensors can drift with time. This is a major advantage of short duration test facilities compared to those continuous running facilities which only calibrate before and after a test. The longer the test time, the more likely the transducers will drift. All other things being equal, the net effect is that the uncertainty in the total pressure measurement due to drift is larger for the longer test.

The details of the online calibration are as follows. Since the pressure transducers are differential, the output of the sensor is proportional to the difference between the pressures on both sides of the transducer. One side of the transducer is exposed to the tunnel which is in a vacuum (to within 0.25 torr). The other side of the transducer is alternately exposed to a reference pressure. The reference pressure is either atmospheric (which is determined by a local reference standard) or a vacuum (to within 0.1 mm Hg). A valve is alternately switched to either of the two reference conditions and the output of the transducers, which are low pass filtered and amplified, are recorded by the data acquisition system. Thus, the transducer is subjected to pressure differentials of 0.0 atm or 1.0 atm. In this way the sensitivities (i.e. scales) of the transducers are characterized. Since the initial pressure of the test section is zero, the offsets (i.e. zeros) of the transducers are determined by their respective initial voltage readings during the time when the valve is closed. The end result of the calibration is the equation of a line from which the transducer output voltage is converted to absolute pressure in atmospheres.

2.5 – Frequency Response of the Downstream Total Pressure Probe

In this section we characterize the response of the downstream total pressure

probe. In any pressure measuring system where there is connecting tubing between the transducer and the point where the pressure is actually required, there are dynamic effects which affect the measurement. This is the case for the downstream total pressure probes where the connecting tubes are 152.4 mm long and 1.0414 mm in diameter for all five pressure ports. This is a well known problem which is addressed in [10] and [11] and summarized here.

If the pressure measuring system is modeled as a second order sytem, then the governing equation is:

$$\frac{1}{\omega_n^2}\frac{d^2P}{dt^2} + \frac{2\xi}{\omega_n}\frac{dP}{dt} + P = K\,P_t \qquad (2.3)$$

where:

ω_n = natural frequency (rad/sec)

ξ = damping ratio

K = static sensitivity

P = pressure measured (Pa)

P_t = true total pressure (Pa)

t = time (sec)

and the initial conditions are:

$$P(t=0) = 0$$

and

$$\frac{dP}{dt} = 0 \text{ at } t=0$$

Figure 2.3 shows a schematic of the connecting tube system. When the volume of the connecting tube is comparable to the cavity which contains the sensor (which

is the case here), the following formulas hold [11]:

$$\omega_n = \frac{a}{L(\frac{1}{2} + V/V_t)^{\frac{1}{2}}} \qquad (2.4)$$

and

$$\xi = \frac{16\mu L}{d_t^2 a}(\frac{1}{2} + V/V_t)^{\frac{1}{2}} \qquad (2.5)$$

where:

a = speed of sound (m/sec)

L = length of connecting tube (m)

V = volume of cavity (m^3)

V_t = volume of connecting tube (m^3)

μ = viscosity (kg/m sec)

d_t = connecting tube diameter (m)

Using nominal values downstream of the rotor (M=0.6 and T_t=343 K) gives ω_n=1762 rad/s and ξ=0.166. Using the definition of the natural frequency, one finds that $f=\omega_n/2\pi$=280 Hz. This value is the estimate of the largest frequency which the pressure measuring system can detect. This is more than enough for steady state pressure measurements. Alternatively, since the system is underdamped, the solution can be written as:

$$\frac{P}{KP_t} = -\frac{e^{-\xi\omega_n t}}{(1-\xi^2)^{\frac{1}{2}}} \sin((1-\xi^2)^{\frac{1}{2}}\omega_n t + \phi) + 1 \qquad (2.6)$$

where:

$$\phi = \sin^{-1}(1-\xi^2)^{1/2} \qquad (2.7)$$

Eqn. 2.7 predicts that the nondimensional value of $P/(K \cdot P_t)$ will equal 0.99 approximately 16 msec after the flow reaches the probe. Figure 2.4 shows the typical response of the downstream pressure transducers during a blowdown test. The legend labels the sensors as PT5AR1, PT5AR2, ..., PT5AR5 where the abbreviation can be summarized as: the "PT" signifies total pressure; the "2" signifies the upstream measuring station whereas the "5" signifies the downstream measuring station; the "A" stands for the circumferential position (i.e. window); and the "R#" indicates the radial position of the sensor ("R5" is closest to the hub and "R1" is closest to the tip). In this case, the probe appears to have responded completely to its step input in approximately 25 msec. This is good agreement with the above calculation and shows that the response of the downstream total pressure rake is sufficient for steady state calculations.

2.6 - Total Pressure Uncertainty Estimation

There are many sources of error present when measuring total pressure. Total pressure is defined as the pressure attained when the fluid is brought to rest isentropically. Since no real process is isentropic, an error results. Another source of error is the aerodynamic interference of the probe. This error is reduced by using an airfoil probe body shape. As mentioned above, an error results when the probe is misaligned with the flow direction (kiel head probes help to minimize this error). It is assumed that the error estimation given in section 2.3.2 accounts for these type of measurement errors. In this section, we will examine other sources of uncertainty which are not accounted for in Eqn. 2.2 such as short and long term drift and the effect of temperature on transducer

sensitivity.

2.6.1 – Short Term Drift

As discussed above, the pressure transducers are calibrated for each test. Obviously, an estimate of the uncertainty of the calibration is required. One way to do this is as follows. Although the test time is short, data is taken at low sampling rates from 1.2 sec to 300 sec (i.e. about 10 times the characteristic time constant of the tunnel) to monitor, among other things, the pressure transducers. At 300 sec, there is no flow in the tunnel so that the pressure should be uniform throughout. Assuming this to be true (at least locally, say, at a rake location), then any deviations between the pressure transducers at this time is a conservative estimate of the pretest calibration uncertainty. Alternatively, this can be thought of as the extent to which the transducers have drifted during the test. This is the approach taken here, and this uncertainty will be called short term drift.

Figure 2.5 and Figure 2.6 show this effect for the upstream and downstream total pressure probes. Typical differences at 300 sec are on the order of 0.6–1.0%. For the average pressure levels at 300 sec, this amounts to less than 0.22 psia. Differences of this level can occur due to free convection effects (i.e. difference in the temperature of the hub and tip walls can set up a buoyancy induced flow), small leaks in the facility, and the effects of temperature changes on the transducer sensitivity (discussed is section 2.6.3). Should this occur, then the uncertainty will be overestimated. As we will see shortly, the magnitude of this uncertainty is large compared to the magnitude of the other uncertainties so that this value dictates the net uncertainty in the pressure measurement. Obviously, if this estimate is conservative, then the net uncertainty in the

efficiency calculation (to be described in Chapter 4) will also be conservative.

2.6.2 – Long Term Drift

The effects of long term drift are accounted for by calibrating at the beginning of each test. The idea here, however, is to monitor the pressure transducers from test to test. If the transducer sensitivity or offset is significantly different for a specific test as compared to the average history of that transducer, then the data for that test is discarded. Alternatively, if a transducer's scales fluctuate significantly from test to test, then the data from that transducer is discarded for all of the tests. Table 2.1 lists the sensitivities and offsets of the upstream rake (labelled PT2AR#) and downstream rake (labelled PT5AR#) for the seven turbine tests.

With the exception of PT2AR3, the sensitivities and offsets are very steady from test to test. Table 2.2 quantifies the long term drift for the total pressure rakes. Column 1 contains the mean value of either the sensitivity (atm/volt) or the offset (volts) for the transducers, while column 2 contains the standard deviation of the two quantities. Column 3 gives the standard deviation as a percent of the corresponding mean value which indicates the long term variations in the scales and zeros of the transducers. As indicated in Table 2.2, the variation in sensitivity is about 0.1% for all of the transducers except for PT2AR3 (10.682%). The variation in offset is again quite small (on the order of 0.3% or lower) except for PT2AR3 (3.024%). This indicates that the transducers have excellent long term stability. The integrity of PT2AR3 is questionable, however, so the data from this transducer was not used for the tests due to its irregular behavior.

TABLE 2.1 - SENSITIVITIES & OFFSETS FOR TURBINE RUNS

Transducer		TEST TURB110	TURB111	TURB112	TURB113	TURB114	TURB115	TURB116
PT2AR1	Sensitivity	0.9336	0.9348	0.9360	0.9351	0.9348	0.9349	0.9359
	Offset	-3.4268	-3.4251	-3.4275	-3.4261	-3.4251	-3.4278	-3.4275
PT2AR2	Sensitivity	0.7997	0.7991	0.7981	0.7994	0.8011	0.7996	0.8009
	Offset	-3.2400	-3.2402	-3.2450	-3.2428	-3.2425	-3.2450	-3.2444
PT2AR3	Sensitivity	0.9005	0.8199	0.8437	0.8905	0.8284	1.1000	0.8846
	Offset	-3.2375	-3.3325	-3.3175	-3.2441	-3.3237	-3.0475	-3.2545
PT2AR4	Sensitivity	0.7715	0.7715	0.7706	0.7715	0.7725	0.7716	0.7718
	Offset	-3.1932	-3.1945	-3.1955	-3.1945	-3.1934	-3.1964	-3.1966
PT2AR5	Sensitivity	0.7950	0.7962	0.7946	0.7950	0.7959	0.7944	0.7958
	Offset	-3.2400	-3.2303	-3.2423	-3.2400	-3.2400	-3.2500	-3.2425
PT2AR6	Sensitivity	0.7981	0.7980	0.7970	0.7991	0.7984	0.7976	0.7982
	Offset	-3.2374	-3.2342	-3.2386	-3.2375	-3.2375	-3.2400	-3.2400
PT5AR1	Sensitivity	0.4322	0.4334	0.4322	0.4325	0.4322	0.4316	0.4318
	Offset	-2.1687	-2.1691	-2.1674	-2.1651	-2.1650	-2.1624	-2.1650
PT5AR2	Sensitivity	0.4396	0.4401	0.4397	0.4395	0.4396	0.4384	0.4399
	Offset	-2.2100	-2.2100	-2.2082	-2.2075	-2.2062	-2.2047	-2.2064
PT5AR3	Sensitivity	0.4323	0.4332	0.4328	0.4332	0.4323	0.4320	0.4327
	Offset	-2.1700	-2.1736	-2.1725	-2.1723	-2.1700	-2.1695	-2.1725
PT5AR4	Sensitivity	0.4259	0.4263	0.4257	0.4260	0.4255	0.4255	0.4254
	Offset	-2.1325	-2.1374	-2.1347	-2.1325	-2.1308	-2.1300	-2.1325
PT5AR5	Sensitivity	0.4253	0.4262	0.4253	0.4252	0.4252	0.4249	0.4253
	Offset	-2.1395	-2.1290	-2.1347	-2.1328	-2.1416	-2.1500	-2.1448

TABLE 2.2 - LONG TERM DRIFT FOR TOTAL PRESSURE RAKE TRANSDUCERS

TRANSDUCER		MEAN VALUE, M	STANDARD DEVIATION, S	S/M %
PT2AR1	Sensitivity	0.9350	8.030×10^{-4}	0.086
	Offset	-3.4266	1.143×10^{-3}	0.033
PT2AR2	Sensitivity	0.7997	1.034×10^{-3}	0.129
	Offset	-3.2428	2.118×10^{-3}	0.065
PT2AR3	Sensitivity	0.8954	9.565×10^{-2}	10.682
	Offset	-3.2510	9.832×10^{-2}	3.024
PT2AR4	Sensitivity	0.7716	5.589×10^{-4}	0.072
	Offset	-3.1949	1.351×10^{-3}	0.042
PT2AR5	Sensitivity	0.7953	6.945×10^{-4}	0.087
	Offset	-3.2421	7.314×10^{-3}	0.225
PT2AR6	Sensitivity	0.7980	6.528×10^{-4}	0.082
	Offset	-3.2379	1.982×10^{-3}	0.061
PT5AR1	Sensitivity	0.4323	5.794×10^{-4}	0.134
	Offset	-2.1661	2.400×10^{-4}	0.111
PT5AR2	Sensitivity	0.4395	5.442×10^{-4}	0.124
	Offset	-2.2076	1.987×10^{-3}	0.090
PT5AR3	Sensitivity	0.4326	4.324×10^{-4}	0.100
	Offset	-2.1715	1.610×10^{-3}	0.074
PT5AR4	Sensitivity	0.4258	3.259×10^{-4}	0.080
	Offset	-2.1329	2.476×10^{-3}	0.116
PT5AR5	Sensitivity	0.4253	4.036×10^{-4}	0.095
	Offset	-2.1389	7.286×10^{-3}	0.341

2.6.3 - Effect of Temperature on Transducer Sensitivity

One other source of error which can be significant is the effect of temperature on transducer sensitivity. Although the transducers are compensated for temperature over the 80 ^{o}F to 250 ^{o}F range, there is still a slight effect on transducer sensitivity. An experiment was performed to quantify this effect as follows. The pressure transducers were placed on a plate in an oven which was heated to five different temperatures. The temperature of the oven was measured by three thermocouples placed at different points on the plate. Pressure calibrations were performed as described above once equilibrium conditions in the oven were established (i.e. when all three thermocouples indicated the same temperature to within 1 ^{o}F for fifteen minutes).

Figure 2.7 and Figure 2.8 show the results for five of the six upstream transducers (only five were available for the experiment at the time) and for the downstream transducers, respectively. There are some interesting points worth noting in both figures. First, Figure 2.7 indicates a 1-2% decrease in sensitivity over the compensated temperature range while Figure 2.8 indicates a slightly larger decrease in sensitivity (about 2.5%) for the downstream transducers. Second, the downstream pressure transducers appear to reach the limit of their compensation at about 220 ^{o}F after which the slope drops off sharply. Third, the sensitivities of the transducers are not the same as for the series of actual blowdown experiments. This is because the gains of the external amplifiers were adjusted so that the sensitivities of the transducers were approximately the same and also to take advantage of the 10 volt resolution of the data acquisition system.

This experiment suggests that a large error can result in the total pressure measurement if the pretest calibration is done at a temperature which is

significantly different from the actual temperature of the transducer during the blowdown. This raises an important question: namely, what is the temperature which the transducer "sees" during a test? The answer to this question dictates the importance of temperature level on transducer output.

Consider the problem in more detail. The transducer is mounted outside of the tunnel so that its gross operating temperature is that of the room. The pressure transducer "sees" gas which has traveled along six inches of 0.004" thick stainless steel tubing which is initially at room temperature. Therefore, the tubing cools the gas. In addition, heat must diffuse through the gas present in the tubes once the initial filling of the connecting tubes is complete. The time required to do this is on the order of the diffusive time scale L^2/α. Here L is 6.0" or 0.1524 m and α ($=k/\rho c_p$) is the gas diffusivity which is approximately 6.0×10^{-6} m^2/s. This gives a time scale on the order of 60 minutes; a huge value compared to the actual test time. Alternatively, heat can conduct along the stainless steel tubing length. Here again, however, the diffusive time scale for such a process is much larger than the test time since $\alpha = 3.5\times10^{-6}$ for stainless steel. Essentially, then, the time scales for heat transfer to the transducer are much larger than the test time so that there should be little or no effect of temperature given the current configuration.

TABLE 2.3 - AVERAGE INLET TEMPERATURE LEVEL

Test	T (K)	$\frac{T - T_{min}}{T_{max} - T_{min}}$
115	421.1	0
114	431.1	0.088
112	435.6	0.128
111	456.9	0.316
113	461.1	0.354
110	481.4	0.533
116	534.3	1

In order to illustrate this point, consider Figures 2.9 and 2.10 which show the

scales of the pressure transducers plotted vs. average inlet total temperature. The total temperature is nondimensionalized as $(T-T_{min})/(T_{max}-T_{min})$. T_{min} and T_{max} are the smallest and largest values of the turbine inlet temperature shown in Table 2.3, respectively. Table 2.3 shows both the dimensional and nondimensional values of the average turbine inlet temperature. Since the values of T shown in the table are an indication of the gas temperature "seen" by the transducer during a test, one would expect to see a large variation in the transducer sensitivities (since the temperatures are outside of the compensated temperature range). Figures 2.9 and 2.10 show no correlation with temperature. Even the variations in transducer PT2AR3 do not appear to have any correlation with temperature. For this reason, it is assumed that the effect of temperature on transducer output is neglible in this application. This argument can be validated experimentally by placing a thermocouple in place of a pressure transducer in order to measure the temperature of the gas in the connecting tube. This has not been done.

2.6.4 – Uncertainty Estimate for the Total Pressure Measurement

This section presents the estimates of the net uncertainty in both the upstream and downstream total pressure measurements. The total uncertainty will be considered to consist of three parts: probe error, short term drift, and signal noise. Since these errors are not correlated, the root mean square should be taken. The pretest calibration error vanishes if we consider measurements relative to a local reference standard. In other words, the pressure transducers are calibrated using the same local references for every test. Any errors in the references disappear when any two tests are compared relative to each other. The other errors are now described. The probe error is given by Eqn. 2.2; the

short term drift is, as described above, the maximum deviation between the pressure transducers for a particular rake at 300 sec; and the noise is the equivalent pressure corresponding to 5 mvolts. Table 2.4 provides a summary of these uncertainties. It is of interest to note that most of the uncertainty in the measurement comes from the short term drift component. If this component is overestimated (reasons for this were given above), then the net uncertainty in the pressure measurement will be overestimated. For the sake of being conservative, however, the estimate of the short term drift is taken as accurate.

TABLE 2.4 - UNCERTAINTIES IN THE TOTAL PRESSURE MEASUREMENT

Test/Location		Probe Error %	Short Term Drift %	Noise %	Total %
110	Upstream	0.003	0.75	0.1	0.757
	Downstream	0.184	0.60	0.2	0.659
111	Upstream	0.003	1.00	0.1	1.005
	Downstream	0.184	0.59	0.2	0.650
112	Upstream	0.003	0.99	0.1	1.000
	Downstream	0.184	0.70	0.2	0.751
113	Upstream	0.003	0.66	0.1	0.668
	Downstream	0.184	0.76	0.2	0.807
114	Upstream	0.003	0.65	0.1	0.658
	Downstream	0.184	0.70	0.2	0.751
115	Upstream	0.003	0.88	0.1	0.886
	Downstream	0.184	0.70	0.2	0.751
116	Upstream	0.003	0.83	0.1	0.836
	Downstream	0.184	0.61	0.2	0.668
				Mean Value Upstream	0.830
				Mean Value Downstream	0.720

* PT2AR3 IS NOT USED FOR THESE TESTS

Chapter 3 - Total Temperature Measurement

3.1 - Introduction

In addition to the total pressure measurement, aerodynamic performance estimation requires the measurement of total temperature at the inlet and the exit of the stage. As with the total pressure measurement described in Chapter 2, some combination of single-sensor probes, rakes and traverses in the radial and circumferential directions are used to measure the time-averaged inlet and exit conditions. The technology to do this in conventional steady state testing facilities is well developed. Essentially, impact thermocouples are placed within a vented shroud which serves at least three purposes. First, the shroud (and bleed holes) are sized to yield recovery factors near one. Second, the shroud serves as a radiation shield. Third, the kiel-head shroud minimizes sensitivity to misalignment errors. The frequency response of this type of probe is on the order of seconds, which is much higher than the 0.25 sec frequency response required in a short duration facility such as the BDT. One of the objectives of this work, then, was to design inexpensive rakes for the purpose of routine measurement of gas total temperature with accuracies which are consistent with performance estimation (better than 0.25%) and step input response on the order of 250 msec [12].

The three constraints (high accuracy, fast response, and low cost) significantly reduce the available options. For example, fast response thermocouples have been developed for shock tube applications, but the accuracy requirements are a great deal less than for the BDT application [13]. Another approach, the aspirating hot wire probe, has high frequency response (20 kHz) and workable accuracy

(1 K), but is too expensive and complicated for multi-sensor rakes [4]. The approach taken here is to adapt conventional thermocouple rakes to the BDT application with emphasis on low cost. Given sufficient care, the accuracy requirements can be satisfied just as in conventional facilities. The primary problem, as we shall see, is the frequency response of the probes.

The objectives of this chapter, then, are as follows. First, the requirements of the probes are discussed in more detail and the main distinction between total temperature measurements in a short duration facility as compared to a conventional facility is addressed. Second, the probe designs considered to meet the requirements are described. Four different variations were constructed and experimentally evaluated to establish the probe behavior. The final design was selected from these four variations. Third, an analytical model of the temperature probe is described which is used along with experimental data to characterize the probe performance. In particular, the model is used to determine the relative importance of error sources (such as steady state and transient conduction, recovery effects, and radiation) and the probe frequency response. Fourth, the application of total temperature rakes to the BDT with the RTDF generator installed is discussed. Finally, an estimate of the uncertainties in the total temperature measurement is given for the tunnel configurations with the RTDF generator.

3.2 – Total Temperature Probe Requirements

The purpose of this section is to state briefly why knowledge of the total temperature is required for performance calculations and also to make the distinction between the total temperature measurement in the BDT and in a conventional steady state facility. First, why measure total temperature? As

mentioned above, the total temperature probes are used to determine the inlet and exit conditions of the turbine stage. In particular, the probe measurements are used to determine the ΔT of the stage (i.e. power) and the temperature ratio of the stage (i.e. stage efficiency). Like the upstream total pressure probe, the upstream total temperature probe measures the inlet radial temperature profile. As discussed in Chapter 5, the effects of inlet radial temperature profiles on turbine aerodynamic performance is a topic of interest to the turbine designer since turbine inlet temperature distributions can have large radial variations.

Second, what is the main distinction between the total temperature measurement in the BDT and the same measurement in conventional steady state facilities? A discussion of the different time scales of the two facilities helps to make that distinction. In this context, "time scales" refer to those characteristic times which are peculiar to a particular facility and not to the physical time scales which are important for fluid mechanics, heat transfer, etc. In a continuous running facility, for example, the inlet temperature is constant with time, and the test time is long compared to the frequency response of the probes. Therefore, time response is not a major concern in steady state measurements. In a short duration test facility, however, this is not the case since the test time is short. In this case, then, time response is a concern even for steady state measurements.

Consider, for now, the BDT configuration without the RTDF generator. Figure 3.1 shows a typical time history of the total or stagnation temperature in the supply tank (labelled "inlet") and at the entrance to the stage which is calculated using the supply tank pressure history and the initial gas temperature. There are four different time scales present in the figure which are of interest. The first time scale is the valve opening time. As shown in the figure, a typical valve opening time is 30 msec. The second time scale is that of the flow startup which stretches from about 30 msec to 100 msec. This is the time during which

steady flow is established in the tunnel. Prior to about 100 msec, then, transient processes are important. The third time scale of interest is that of the actual steady state time, 250 msec to 550 msec. It is during this time period when the turbine is choked and the corrected speed and corrected flow are constant. The fourth time scale of interest is the characteristic decay rate of the supply tank. As seen in the figure, the total temperature drops about 5% over the first 500 msec of flow time. This translates to a blowdown time constant on the order of 25 sec.

Figure 3.1 also shows the response of a temperature rake element to the inlet gas total temperature (labelled "sensor"). Initially, the probe is at room temperature in a vacuum. The valve opens in about 30 msec admitting flow to the test section. As seen in the figure, the probe "sees" a step input in temperature which is dropping off exponentially according to the blowdown time constant. Given the distinctions between the BDT and a continuous running facility, the requirements of the total temperature probes can be succinctly stated as follows: the probes must respond to step inputs in gas total temperature in less than 300 msec with accuracies of 0.25% or better. If the probes cannot respond fully in that time span, then some time accurate means of correcting the data must be employed. This is discussed in detail below.

3.3 – Total Temperature Probe Design

3.3.1 – Probe Geometry Considerations

The probe geometry must be designed to maximize frequency response and minimize error. Of primary concern is the first order time response of the thermocouple junction itself. The time constant of the junction itself is τ =

$\rho V c_p/hA$ where h is the heat transfer coefficient, A is the surface area, ρ is the density, V is the volume, and c_p is the specific heat (all of the junction). This expression is obtained from an energy balance for the thermocouple (shown later). Aside from size considerations (the smaller the better), the response is governed by the heat transfer coefficient h. The heat transfer coefficient, in turn, is related to the Nusselt number (Nu), the nondimensional heat transfer coefficient by the relation:

$$Nu = \frac{h\ D}{k} \qquad (3.1)$$

where D is the characteristic dimension of the junction and k is thermal conductivity of the gas. The Nusselt number Nu is a function of Reynolds number based on D, Re_D, Prandtl number, Pr, and junction geometry. It turns out that for thermocouple junctions of 25 μm diameter or less and a flow geometry over the junction of 5 m/s, τ is about 3 msec. Provided that the actual thermocouple mounting is adequate, this should be sufficient for the BDT application. It is important to note that the presence of conduction (steady and transient), recovery effects, and radiation will decrease the overall time constant of the temperature measuring system. The relative magnitudes of these errors are considered later.

For the purposes of the design, however, these error sources must be considered qualitatively. Steady state conduction, recovery effects, and radiation are common to any thermocouple type probe, discussions of which can be found in [14] – [20]. Figure 3.2 illustrates a typical shielded, vented probe head. The junction is at the end of a long L/D insulated support to minimize conduction error. The L/D should be as long as possible to minimize the error, consistent with mechanical integrity, fabrication, and mounting constraints. The size of the bleed hole diameter d sets the velocity over the junction. Since Nu is proportional to velocity, a high velocity is desirable to reduce the time constant

of the junction, but this results in larger recovery losses. Therefore, some tradeoff between these two effects is necessary. The shroud minimizes flow misalignment errors and also serves as a radiation shield. Because the temperatures are relatively low in the BDT, however, radiation errors are small.

One error source which is peculiar to this application is transient conduction along the junction support. The driving force for this effect is the temperature difference between the junction and the probe body. Since the probe body is massive compared to the junction support, it remains nearly isothermal during the test time (the diffusive time scale $t=L^2/\alpha$ is on the order of 4 sec). Hence, there can be a 180 K temperature difference along the support assuming that its initial temperature is about 300 K. As the test progresses, the support heats up and the conduction error reduces towards its steady state value. The magnitude of this error is calculated later.

3.3.2 – Probe Design Implementation

3.3.2.1 – Sensor Description

As stated above, the first order response of the junction necessitates a thermocouple which is 25 μm or less. Thermocouples which are this small, however, are extremely difficult to work with. Fortunately, fabricated thermocouple subassemblies are commercially available from Paul Beckman Inc. [21] at reasonable cost. Figure 3.3 shows a schematic of the sensor. The sensor consists of a type K (chromel–alumel) thermocouple disc junction 20 μm in diameter by 2.5 μm thick, with 20 μm diameter thermocouple lead wires. The junction is placed at the end of a specified length cylindrical support constructed of 76 μm diameter quartz. The quartz may be sheathed in a 200 μm O.D.

stainless steel tube for mechanical support. As one might imagine, the steel sheath increases the effective thermal conductivity of the support, the area for heat to conduct, and the mass of the support. The conduction error for the stainless steel case will be greater than the cases without it for transient processes. Therefore, in the BDT application, the stainless steel tubing should only be used if the mechanical integrity of the support is questionable. As we shall see, use of the stainless steel tubing is not necessary.

3.3.2.2 – Four Probe Head Designs

Since the performance of the sensor is difficult to assess a priori, a prototype rake with four different head designs was constructed and tested to experimentally establish the probe behavior. In this way, the effects of support length, diameter, and material as well as bleed hole size could be determined. Figure 3.4 shows the different head designs. Two different length standoffs were used, 7.6 mm and 3.8 mm. The shorter standoff would be desirable so that the entire probe would fit through the 12.7 mm (0.5") instrumentation ports. For each standoff, two different supports were used, one with quartz only and one with both quartz and stainless steel tubing. The four probe heads are mounted on an aerodynamically contoured stainless steel probe body 49.022 mm long. The body is cantilevered from a 12.5 mm diameter stainless steel shaft. Figure 3.5 illustrates the prototype probe with the four head designs. The thermocouple wires feed through the probe body along the stainless shaft to the electronics package which is attached to the shaft outside the tunnel. The electronics are discussed further below.

The probe head design variables shown in Figure 3.2 are listed in Table 3.1 for each of the four head designs. As seen in the table, the bleed hole diameter

was different only for case 1. The support diameter is determined by the insulation type, quartz or stainless steel and quartz. Variable dimensions not shown in the figure were identical for all four cases and are given here. The stainless steel shroud O.D. was 2.34 mm; the inlet bevel half angle was 15 °; the inlet I.D. was 1.7 mm (after contraction); and the distance from the junction to the bleed whole was 2.5 mm.

Table 3.1 - Probe Head Design Geometries (mm)

Case #	Descriptor	l	d	D	L
1	short w S.S.	1.5	0.86	0.20	3.81
2	long w S.S.	5.6	0.61	0.20	7.62
3	short w/o S.S.	1.5	0.61	0.076	3.81
4	long w/o S.S.	5.6	0.61	0.076	7.62

3.3.2.3 - Signal Conditioning

Since the time constant of the junction itself is on the order of 3 msec, the electrical cutoff frequency for this probe is above 60 Hz. Thus, one must be concerned with electrical pickup. In an attempt to minimize thermocouple lead lengths and ground loop problems, the integrated circuit signal conditioners are placed in a small box which is cantilevered from the probe shaft just outside the tunnel walls. The signal conditioner, Analog Devices AD597AH, provides electronic ice point compensation, linearization, and amplification at a very low cost ($15). The output of the signal conditioner is amplified and low pass filtered by an amplifier which is external to the probe. The output of this amplifier is then recorded by the 12 bit A/D system. Since the resolution of the A/D system is 2.5 mvolts, the net temperature resolution after amplification is 0.06 K. The noise level, however, was 5-10 mvolts peak-to-peak which amounts to approximately 0.15 K. The uncertainties due to short term drift and long term drift are discussed in the section on temperature measurement uncertainties.

3.3.2.4 – Mechanical Performance of the Temperature Probes

The mechanical performance of the probes (both the prototype and the final upstream and downstream designs) was completely satisfactory. There were no mechanical failures over some 20 tests. The probes survived a 50 gallon leak of 500 ^{o}F heat transfer oil into the flow and a dirty heat exchanger which introduced enough particles into the flow to sandblast the tunnel walls and, with it, a fellow graduate student's experiment [5]. This suggests that the stainless steel tubing for the thermocouple support is not necessary.

3.4 – Total Temperature Probe Model and Probe Evaluation

3.4.1 – Overview

The purpose of this section is threefold. First, the results of the tests used to evaluate the four head probe designs are briefly presented, and the motivation for a model is given. Second, the temperature probe model is described in detail. Third, the probe model is applied with the aid of the experimental results to determine the temperature measurement error.

3.4.2 – Experimental Probe Performance

The prototype probe was tested by placing it upstream of the nozzle guide vanes in the BDT. This is illustrated in Figure 3.6 which shows the upstream rake location relative to the NGV's and the rotor (9.5 cm upstream of the NGV leading edge). There is a clear flow path from the supply tank to the upstream station

(without the RTDF generator) with the boundary layer bled off just upstream of the probe. Because the flow is nearly adiabatic, the stagnation temperature at this location should be the same as in the supply tank. This provides a means to evaluate the response and accuracy of the four head designs if the supply tank temperature is known with sufficient accuracy.

Unfortunately, this was not the case for the tests which were performed. The reason why the supply tank temperature was not known to a sufficient level of accuracy is because the BDT was originally intended for heat transfer studies. For this application, three thermocouples (which were not individually calibrated) were placed in the supply tank to measure the gas temperature (tank top, middle, and bottom), and the thermocouple readout on the control panel has only 1 ^{o}F resolution. Although this is sufficient for heat transfer studies, it is not for aerodynamic studies. Furthermore, there was no mechanical stirring of the supply tank gas so that temperature uniformity depended on tank metal uniformity (which is a function of the heating history of the supply tank for a given test) and free convection. As a result, temperature nonuniformities of 1–3 ^{o}F were not uncommon. This complication can obviously be avoided in the future by placing a string of calibrated thermocouples diagonally across the supply tank to assess temperature nonuniformities and by introducing forced mixing in the supply tank. In order to derive information from the current tests, however, some assumptions are necessary. These are discussed further below.

Figures 3.7 and 3.8 show the raw data traces of all four sensors for the prototype rake for TEST73 and TEST74, respectively. The inlet temperature for TEST74 was about 60 K hotter than that of TEST73. The raw traces show that the differences between the four designs is small, on the order of a few degrees K. When the accuracy requirements of the measurements are on the order of tenths of degree K, however, these small differences are exceedingly important.

Since we are considering small differences in temperature, it becomes clear that a model which can accurately describe the measurement process is highly desirable. This is the motivation for the probe model.

3.4.3 - Temperature Probe Model Description

3.4.3.1 - Thermocouple Energy Balance

This section gives the details of the temperature probe model. Since the two main concerns here are time response and accuracy, the probe model should be unsteady and take into account the three modes of error: conduction, recovery effects, and radiation. In addition, the model should be able to be driven by experimental data (i.e. the best estimate of the inlet gas total temperature). That is the approach taken here.

Figure 3.9 shows the energy balance for the thermocouple junction. The time rate of change of energy contained in the junction (which is considered to be at a uniform temperature) is balanced by the rate of change of energy entering the junction in the form of forced convection, and the rate of change of energy leaving the junction in the form of conduction along the support, recovery effects, and radiation losses. This statement of the energy balance may be written as:

$$E_{st} = E_{in} - E_{out} \tag{3.2}$$

or, more specifically, as:

$$\rho V c_p \frac{dT}{dt} = hA\,(T_t - T) - Q_{cond} - Q_{rec} - Q_{rad} \tag{3.3}$$

where ρ is the density, V is the volume, c_p is the specific heat, h is the heat

transfer coefficient, A is the surface area, and T is the temperature. T_t is the true gas total temperature, Q_{cond} is heat conduction loss, Q_{rec} is the equivalent heat loss due to the fact that the gas is not actually stagnated, and Q_{rad} is the radiation heat loss from the junction. If one neglects the heat loss terms in Eqn. 3.3, the solution to the above is the classic exponential response to T_t where the time constant is that given above. The recovery heat loss can be written as [16]:

$$Q_{rec} = \frac{(1-r)\ \frac{\gamma-1}{2}\ M^2\ hAT_t}{1 + \frac{\gamma-1}{2} M^2} \qquad (3.4)$$

where r is the recovery factor of the junction and M is the Mach number of the gas flowing past the junction (not the free stream Mach number). Due to the fact that the Reynolds number based on the junction disc diameter is very small, the flow over the junction is assumed to be laminar and the recovery factor r is taken as $Pr^{1/2}$. The radiation heat loss can be written as [16]:

$$Q_{rad} = \sigma \epsilon A(T^4 - T_{surr}^4) \qquad (3.5)$$

where $\sigma = 5.67 \times 10^{-8}$ W/(m^2 K^4) is the Stefan–Boltzmann constant and ϵ is the emissivity of the junction. A value of 0.4 is used for the emissivity of the chromel–alumel junction [22].

One other piece of information which is required to calculate the time response of the probe is the conduction error along the junction support. Haig suggests that the conduction along the support can be accurately determined by treating the support as an extended fin [16]. The solution given in [16], however, is for the case of steady state heat transfer along a solid cylindrical tube of one material. Details of this solution can be found in [22]. Although Haig's solution does not apply here, the approach is still valid if generalized to include multiple materials and transient effects. This generalized approach is now described.

3.4.3.2 – Transient Conduction Model for the Junction Support

Since the conduction along the junction support is required as a function of time, the approach is to perform an energy balance for the junction support to obtain the equations which govern its temperature distribution. The governing equation, with appropriate boundary conditions and initial condition, can then be solved at discrete times using standard finite–difference techniques to obtain the support temperature distribution. At each time step, then, the conduction along the support can be calculated given the temperature distribution.

Figure 3.10 is a schematic of the transient conduction model for the support. The temperature distribution along the support is a function of axial distance and time. The boundary condition at x=0 is $T(x=0,t)=T_{body}$, and boundary condition at x=L is the convective boundary condition. The initial condition T(x,t=0) is a linear temperature distribution between T_{body} and the initial sensor temperature. This is because the probe is initially in vacuum prior to the test so that the heat transfer coefficients are nearly zero. Assuming that the temperature condition is steady with time and that radiation losses are negligible, the solution to the heat equation is a linear temperature distribution. During the test, the support is assigned an average heat transfer coefficient h_{stem} based on the stem length. The correlations for the support and junction Nusselt numbers are given below and are functions of time as well. Only material properties are considered constant. Values of the material properties can be found in [23]. The gas total temperature is a function of time and has either a functional form input by the user, or it can be the supply tank total temperature estimate.

Following the same procedure as for the thermocouple junction, an energy balance is performed on the support (Figure 3.11). If we look at a length Δx of

the support, the energy balance gives that the time rate of change of energy contained in the volume is balanced by conduction in, conduction out, and convective heat transfer from the support. In general, the support consists of the two thermocouple leads, chromel and alumel, the quartz insulation, and the stainless steel protective sheath. The energy balance can be written as:

$$E_{st} = Q_x - (Q_x + \frac{\partial Q_x}{\partial x} \Delta x) - Q_{conv} \tag{3.6}$$

where

$$E_{st} = \Delta x\{(\rho Ac_p)_{al}+(\rho Ac_p)_{ch}+(\rho Ac_p)_q+(\rho Ac_p)_{ss}\} \frac{\partial T}{\partial t} \tag{3.7}$$

and

$$-\frac{\partial}{\partial x}(Q_x)\Delta x = -\frac{\partial^2 T}{\partial x^2}\{(kA)_{al}+(kA)_{ch}+(kA)_q+(kA)_{ss}\}\Delta x \tag{3.8}$$

and

$$Q_{conv} = \bar{h}_{stem} AP\Delta x(T - T_t) \tag{3.9}$$

After substituting into Eqn. 3.6 and simplifying gives the governing partial differential equation:

$$\{(\rho Ac_p)_{al}+(\rho Ac_p)_{ch}+(\rho Ac_p)_q+(\rho Ac_p)_{ss}\} \frac{\partial T}{\partial t} =$$

$$\{(kA)_{al}+(KA)_{ch}+(KA)_q+(KA)_{ss}\} \frac{\partial^2 T}{\partial x^2} - \bar{h}_{stem} P (T - T_t) \tag{3.10}$$

The boundary conditions and initial condition are:

$$x = 0 : \quad T = T_{body}$$
$$x = L : \quad -\{(KA)_q + (KA)_{ss}\} \frac{\partial T}{\partial x} = \bar{h}_{stem} A \, (T - T_t) \qquad (3.11)$$

$$t = 0 : \quad T(x,0) = T_{body} + \{T_{sensor}(0) - T_{body}\} \cdot \frac{x}{L} \qquad (3.12)$$

As stated above, Eqn. 3.10 can be solved at discrete time points for the support temperature distribution. The conduction along the support at x=L can then be calculated using the equation:

$$Q_{cond} = \{(KA)_{al} + (KA)_{ch}\} \frac{\partial T}{\partial x}_{x=L} \qquad (3.13)$$

Once Q_{cond} is known as a function of time, it can be substituted into Eqn 3.3 which can then be solved for the temperature of the sensor.

3.4.3.3 – Determination of Heat Transfer Coefficients

At this point, it is appropiate to describe how the support and junction heat transfer coefficients are calculated. In each case, h is determined by Eqn. 3.1 where k is the thermal conductivity of the fluid in the shroud. It is assumed that k has the same value for both. What about the length scale D? For the case of the support, the heat transfer process is characterized as an internal flow between concentric cylinders so that the length scale of interest here is the hydraulic diameter D_h (i.e. the difference between the shroud I.D. and the support diameter). For the case of the thermocouple junction, however, the flow is consider to be an external flow over a flat plate since the junction is shaped like a disc (Figure 3.3) and is located in the inviscid core region of the flow. The appropriate length scale here is the 20 μm diameter of the disc.

What form should the Nusselt number take for each case? Since the support is located in the entry region (for both the viscous and thermal boundary layers), the Nusselt number is larger than for fully developed flow in concentric cylinders [22]. Incropera and DeWitt give the following relation for the case of an internal flow where both a viscous and a thermal boundary layer are developing:

$$\overline{Nu} = 1.86 \{ Re_D Pr / (L/D) \}^{\frac{1}{3}} (\mu/\mu_s)^{0.14} \qquad (3.14)$$

The expression is valid as long as : $Nu_D/1.86$ is greater than approximately 2; $0.48 < Pr < 16{,}700$; $0.0044 < (\mu/\mu_s) < 9.75$; and T_s = constant. Here the subscript s denotes the support surface conditions. All of the requirements are satisfied except for the constant surface temperature condition since the actual conditions in the shroud more closely resemble a constant surface heat flux condition. For this reason, the factor 1.86 was multiplied by the ratio of 4.36/3.66 (i.e. the ratio of the Nusselt number for the constant surface heat flux condition to the Nusselt number for the constant surface temperature condition in fully developed pipe flow). The term raised to the 0.14 power (i.e. a correction term to account for large property variations) is neglected since its value will be nearly one for the cases considered. One other change is that the hydraulic diameter is used in place of D. Typical values for the average support Nusselt number exceed 4.36 (since the support lies in the entry region of the flow).

As mentioned above, the flow over the thermocouple junction is laminar since the Reynolds number is very small. Because of this, an average Nusselt number for laminar flow over a flat plate is used to calculate the junction heat transfer coefficient (giving typical values of about 3.0):

$$Nu_D = 0.664 \, Re_D^{\frac{1}{2}} \, Pr^{\frac{1}{3}} \qquad (3.15)$$

3.4.4 – Application of Probe Model

Now that the model has been described in detail, it can be applied to the two prototype probe tests, TEST73 and TEST74, with two goals in mind. First, the experimental data is used to validate the probe model. Second, given sufficient confidence in the model, it can then be used to determine the magnitudes of the conduction, recovery, and radiation errors. If the errors predicted by the model exceed the maximum allowable error for the performance calculations, then the model can be used to correct the data.

For tests TEST73 and TEST74, the probe was placed upstream of the turbine inlet where the total temperature should be the same as in the supply tank. As discussed above, however, the supply tank temperature is not known with sufficient precision. Thus, in order to derive information from these tests on the validity of the model, and to account for the lack of precision to which the inlet temperature was known, some assumptions must be made. These assumptions are now discussed.

There are two problems associated with determining the inlet temperature, the initial gas temperature and nonuniformities in gas temperature. Consider the problem of the initial gas temperature first. The lack of knowledge of the precise initial temperature results in a "shift" in the calculation of the supply tank total temperature history. For example, the calculated total temperature will exceed the true value by 1% if the the initial temperature measurement is high by 1%. This uncertainty is accounted for by shifting the level of the supply tank temperature in a systematic fashion. This is done as follows. It was assumed that the thermocouples reach their respective steady state condition after 1 second, and the freestream total temperature at each sensor location was

assumed to be at the sensor temperature corrected for steady state errors. This, in effect, adjusts the level of the d.c. offset of the supply tank thermocouples.

The second problem, temperature nonuniformities, result in total temperature variations at the measuring plane. The variations appear in the form of low frequency waves of 1–2 K amplitude in the data traces. The wavelength of these disturbances match the supply tank's transverse dimension (2.1 m). The effects of these waves are to increase the uncertainty to which the total temperature can be estimated at the rake location.

3.4.4.1 – Model Validation

This section shows how the results of the prototype probe tests can be used to validate the model. Given the correction for the d.c. offset of the supply tank thermocouples and the waves present in the data traces, any remaining discrepancies between the model prediction and the sensor data is due to model deficiencies. Figures 3.12 and 3.13 show the results of applying the model to TEST73 and TEST74, respectively. The ratio of the temperature predicted by the model to the actual sensor raw data is plotted over the 250 to 1000 msec test time for all four head designs listed in Table 3.1. The figure of merit here is how close to one the ratio is over the test time. Note that the ratio is identically one at one second due to the assumptions made. The results show that the model is able to predict the sensor temperature to a fraction of a percent for all of the cases. The model is better for the two cases without stainless steel (0 to 0.5%) than for those with stainless steel (0 to 0.9%). The figures both show the wavelike disturbances just mentioned (they occur for all four sensors at the same time). The amplitudes of these waves are about 0.3% (1–2 K). The conclusion is that the model does a very good job of predicting the temperature indicated by

the sensors.

3.4.4.2 – Model Error Prediction

Given that the model is capable of predicting the temperatures measured by the sensors, it can now be used to estimate the magnitude of the error sources versus time (which characterizes the frequency response of the four head designs). The model can also be used to correct the raw data. Figure 3.14 shows the magnitude of the nondimensional errors predicted by the model for TEST73. Here, nondimensional error is defined as the difference between the gas total temperature and the sensor temperature divided by the gas total temperature. As one can see, the presence of the stainless steel adds considerable error to the measurement. Fortunately, the satisfactory mechanical performance of the quartz insulated supports suggests that the stainless steel support is not needed and, consequently, the measurement error can be significantly reduced by using quartz insulated supports only. It is interesting to note that the error changes sign from positive to negative for the quartz only probes around 550–650 msec and remains below 0.25 K for 100 msec. This occurs because of the negative slope of the supply tank total temperature history. The probe "lags" the flow so that, once the flow startup–induced thermal transient damps, the initially smaller overshoot error dominates. This effect is identical to the classical response of a first–order system to a downward–sloping ramp function.

Since the model calculates the temperature error as a function of time, the data can be corrected by adding the error to the sensor data. This was done for TEST73 and TEST74, and Figures 3.15 and 3.16 show the results. The ratio of the corrected sensor temperature to the best estimate of the gas total temperature is shown versus time. Note that since it was assumed that the

sensors reach their respective steady state condition at one second, the ratio is identically one at this time. In other words, the sensor output at one second (corrected for conduction, recovery, and radiation errors) is assumed equal to the gas total temperature. Again, the figure of merit is that the ratio should be one prior to one second. Any residual error is due to temperature nonuniformities and model defiencies. If one ignores the "bumps" as temperature nonuniformities, then the model residual error is about 0.2% for the cases without stainless steel.

The proper procedure to validate the model was mentioned above and is emphasized again here. A string of supply tank temperature thermocouples should be calibrated, and a fan should be introduced to mix out the temperature nonuniformities. A bypass duct with a fast acting valve could be used with the probe placed as close as possible to the tank (to reduce non-adiabatic effects). In this way, the supply tank temperature is well characterized. This was not done due to time constraints.

3.4.4.3 – Steady State Model Error Prediction

It is instructive at this point to give the nondimensional form of the conduction, recovery, and radiation error. This is done by taking the governing equation for the thermocouple heat balance, Eqn. 3.3, and solving this equation at steady state conditions. Obviously, there are three error terms, E_{cond}, E_{rec}, and E_{rad}. The steady state error is just the sum of the steady state heat losses divided by hA of the sensor. The equation for heat losses due to recovery effects was given as Eqn. 3.4 so that the steady state recovery error nondimensionalized by T_t can be written as:

$$\frac{E_{vel}}{T_t} = \frac{(1-r)\,\frac{\gamma-1}{2}\,M^2}{1+\frac{\gamma-1}{2}\,M^2} \tag{3.16}$$

The equation for radiation heat losses was given as Eqn. 3.5 so that the steady state radiation error nondimensionalized by T_t can be expressed as:

$$\frac{E_{rad}}{T_t} = \frac{\sigma\epsilon(T_{sensor}^4 - T_{surr}^4)}{h_{sensor}\,T_t} \tag{3.17}$$

To obtain the steady state conduction error requires the steady state solution of Eqn. 3.10 for the support temperature distribution. The temperature gradient at x=L is obtained by differentiating the solution at x=L. Substituting this into the equation for conduction heat losses, Eqn 3.13, dividing through by hA of the sensor, and simplifying gives the steady state conduction error as:

$$\frac{E_{cond}}{T_t} = \frac{\{(kA)_{al}+(kA)_{ch}\}\,h_{stem}(A_{ss}+A_q)(T_t - T_{body})}{[(kA)_{ss}+(kA)_q]\,(hA)_{sensor}\,T_t \left\{\cosh(mL) + \frac{h_{stem}(A_{ss}+A_q)}{m[(kA)_{ss}+(kA)_q]}\sinh(mL)\right\}} \tag{3.18}$$

where:

$$m^2 = \frac{h_{stem}\,P}{(kA)_{al}+(kA)_{ch}+(kA)_q+(kA)_{ss}} \tag{3.19}$$

The expression for the steady state conduction error is obviously very complicated and, unfortunately, not very insightful at first glance. The expression is useful, however, to check the finite-difference solution to the model since the answer is exact. The solution, however, is only valid for the case where both the thermocouple junction and the gas temperature is not changing with time.

Table 3.2 shows representative steady state errors for both the nominal upstream and downstream test conditions using Eqns. 3.16 – 3.19. As seen in the table, radiation error is negligible for all cases considered. The recovery error is negligible upstream (Mach number = 0.07) but is of the same order of magnitude as the conduction error downstream (Mach number = 0.6). For the short quartz only design, the conduction error equals the recovery error downstream and sums to 0.3 K, while the error upstream is due to conduction only and equals 0.8 K. There is one other interesting point to make here. The long standoff with stainless steel has a smaller conduction error than the short standoff with just quartz. This is only true for the case of constant inlet temperature (i.e. a step input which does not drop off with time). For the case where the inlet temperature is changing with time (as in the tests described above) the larger thermal mass of the designs with the stainless steel sheath causes those designs to have a longer response time. Therefore, the model is less accurate for the cases with stainless steel than for the cases with quartz only. This is because the assumption that the designs reach their respective steady state conditions at one second is better for the quartz only designs (because of their smaller mass).

Table 3.2 - Representative Steady State Errors (K)

Upstream ($M=0.07, T_t=478$ K)	Conduction	Recovery	Radiation
Sensor Type			
Short w S.S.++	2.67	0.010	0.06
Long w S.S.	0.36	0.003	0.08
Short w/o S.S.	0.82	0.003	0.08
Long w/o S.S.	0.009	0.003	0.08
Downstream ($M=0.6, T_t=343$ K)			
Sensor Type			
Short w S.S.++	0.53	0.62	0.02
Long w S.S.	0.07	0.15	0.03
Short w/o S.S.	0.15	0.15	0.03
Long w/o S.S.	0.002	0.15	0.03

++ enlarged bleed hole case

3.5 - Total Temperature Measurement With the RTDF Generator Installed

In this section we discuss the measurement of total temperature with the RTDF generator installed in the tunnel. First, the final upstream and downstream probe designs are described. Second, a method which was used to reduce the magnitude of the conduction error is described. Third, the probe model is used to estimate the temperature measurement uncertainty with the RTDF present.

3.5.1 - Final Probe Designs

Based on the results of the previous section, a final design was selected. The head design was that of case 3, the short standoff quartz insulated support.

The probe designs are shown in Figures 3.17 and 3.18 for the upstream and downstream probes, respectively. The probes use the same thermocouple junction and signal conditioning package as described above. One other feature of the design which is new is now described.

3.5.2 – Probe Heating

The results of the previous section indicate that the dominant error source is conduction along the junction support. In addition, the "residual" error in the model was seen to be about 0.2% (0.8 K) which is higher than that required for highly accurate performance calculations. There are two ways of reducing these errors (besides improving the experimental data). One way is to introduce micro–thermocouples at the base of the support to measure the temperature there. This improves the information into the model since the support constant temperature boundary condition at x=0 is no longer necessary. However, this would be very expensive since this technique precludes the use of commercially available thermocouple assemblies (remember that one of the objectives was to make the probes inexpensive). The other approach [24] is to preheat the probe body to the approximate temperature that the probe would see during the test time. The motivation for this is to decrease the ΔT across the support, thereby reducing the conduction error. This can be seen by examining Eqn. 3.18 which shows that the conduction error is directly proportional to the ΔT across the support, $T_t - T_{body}$.

The second approach was adapted due to its simplicity and the potential for error reduction. The upstream and downstream probes were constructed with electric heating wire imbedded along the probe body using high temperature epoxy. The heater wire resistance was 16 Ω for the upstream probe and 9 Ω

for the downstream probe. The heaters were controlled in servo loop using the AD597AH (which includes set point and control circuitry) and thermocouples imbedded in the probe body. One amp fuses were included in the heating circuit to prevent heater wire burnout (which is a concern since the probes are in a vacuum prior to test and the only mechanisms to cool the probe are conduction along the probe body to the tunnel walls and radiation from the probe). Heating experiments in a small vacuum tank indicated that only a few watts of power are required to heat the probe to the temperature levels seen in the BDT. The time required for the probe to reach its steady state heating condition is on the order of five minutes. During the course of the tests, the probe body thermocouples failed and so the AD597 could not be used in its control mode. Fortunately, however, the rake sensors could be used to monitor the heating process. The steady state temperature of the sensors during heating proved to be very repeatable (to within 1–2 K for a given power setting).

Note that the initial temperature of the probe cannot be set exactly to match the gas temperature for three reasons. First, the RTDF generator provides an inlet radial temperature profile. Second, the turbine has a radial work distribution associated with it. Third, the heating creates a temperature profile in the probe body. An analogy for this third point is that a solid wall with uniform heat generation has a parabolic steady state temperature distribution provided that the two boundary conditions are not identical temperatures. How close the probe can be heated to the steady state gas temperature depends on the magnitude of the three effects just mentioned. As we shall see shortly, however, the probe heating can reduce the ΔT across the support by a factor 3 or 4. For the six heated RTDF tests which were performed with both rakes in operation, the maximum ΔT across the support was 65 K. The performance of the heated probes can be verified experimentally once the supply tank is properly equipped with calibrated

thermocouples and a fan.

3.5.3 – Determination of Error for RTDF Tests

The next step is to actually determine the magnitude of the errors for the case with the RTDF generator installed. Figure 3.19 shows the probe responses for four cases of interest; an upstream sensor heated above its steady state temperature, an upstream sensor heated below its steady state temperature, a downstream sensor heated above its steady state temperature, and a downstream sensor heated below its steady state temperature. The four cases shown are the worst cases in terms of heating (i.e. the initial sensor temperature was furthest away from its respective steady state value). As a result, the error calculated for these four cases should be larger than the error for any other case. The figure has some interesting aspects associated with it besides the initial condition of the sensor due to the heating. The most striking feature is the "bump" in the data around 75 msec. These bumps suggest that the probes have been exposed to an impulse in temperature at the start of the test. The origin of the bump and its effect on probe response is one concern which is addressed further below. The second feature of interest is that the probes respond (after the spike) as if the gas temperature were constant. This should be the case in the presence of the heat exchanger. This aspect is also addressed below.

3.5.3.1 – Origin and Effect of Temperature Impulse

The first question concerning the spike is, assuming it to be a real effect, where it comes from. The second question is, regardless of where it comes from, whether it affects the response of the probe out around 450–500 msec.

As we shall see shortly, it has a very small effect so that the answer to the first question becomes less important (not necessarily less interesting though).

Let us consider explanations to the first question briefly. First, we must determine when the spike occurs and see if its presence correlates with other factors. The spike occurs when the RTDF generator is present in the tunnel. Does it occur when the generator is not present? Inspection of the prototype probe data shows a slight "bump" early in the test (the first 100 msec) for the sensor with the larger bleed holes (i.e. the short standoff with stainless steel). This is shown in Figure 3.7. The larger bleed hole increases the velocity over the junction and therefore improves the first order response of the junction. The larger velocity results in higher recovery losses, but since the upstream Mach number is about 0.07, this error is small. This suggests, possibly, that the temperature impulse may be present in the tunnel even without the RTDF generator. If so, where does it come from and why don't we see it in the response of all four head designs?

The source of the bump might be compressional heating. In other words, the high pressure in the supply tank coupled with the initial vacuum in the test section has the effect of compressing the gas and, therefore, heating it. This effect lasts only a short time until the pressure equalizes in the tunnel. Another possible source might be the high heat transfer rate in the heat exchanger at the start of the test. The RTDF generator is a large electrically heated honeycomb structure designed to have an effectiveness (i.e. outlet gas temperature/metal temperature) near 0.95 [5]. At the start of the test, the heat transfer is more efficient due to the near vacuum conditions. The effectiveness may reach values as high as one (i.e. the gas may reach the metal temperature). These two effects together may combine to give an impulse in temperature.

For one test, TEST115, the probes were not heated prior to the test. The

data traces are shown for the upstream probe in Figure 3.20. Note that the probes indicate a slight "bump" near 75 msec. The upstream probe has exactly the same head design as case 3 (i.e. smaller bleed holes). The RTDF generator is present in the tunnel as well. The only difference between this test and and the other tests shown in Figure 3.19 is the probe heating. Since the probe heating decreases the conduction error and, hence, improves the probe response, the temperature impulse may be present in all tests (with or without the generator). The suggestion is that the probe heating improves the response and allows one to "see" the temperature impulse. Of course, an obvious way to check this is to use the high frequency response aspirating probe mentioned earlier to determine the details of the temperature impulse. This has not been done.

The question of the impulse is of concern only if it significantly affects the probe reading around 500 msec. To what extent the impulse affects the probe response is important for two reasons. First, as just discussed, the origin of the temperature impulse is largely unexplored. Hence, the magnitude of the impulse is unknown. Second, if the magnitude of the impulse proved to affect the probe response, we would have no way of "driving" the model (i.e. supplying the model with a good estimate of the gas total temperature) and, therefore, determining the magnitude of the error sources. The approach taken here is to examine the four cases shown in Figure 3.19. The idea is to drive the model with four different levels of temperature impulse: 125%, 100%, 50%, and 0% of the maximum temperature indicated by the sensor for a short period of time (i.e. from the time when the valve opens until the time when the sensor reaches its maximum temperature). This is followed by a constant temperature equal to the average temperature read by the sensor at 500 msec. The constant temperature portion of the input is a direct result of the observation made above: after the initial impulse, the probe appears to respond to a constant temperature input. This

should be the case since the heat exchanger thermal mass is huge compared to the gas flowing through it so that the exit total temperature of the gas should remain constant over the test time. For the downstream probe, where the turbine power extraction is dropping off with time, the temperature should increase slightly with time. From Figure 3.19, however, this amount appears to be very small and is neglected.

The results of the model tell us to what extent the impulse is important and also determine the temperature uncertainty. Figures 3.21 to 3.24 show the results of the model for the four cases. Figures 3.21a, 3.22a, 3.23a, and 3.24a show the four different driving temperatures which were input to the model for each of the four cases shown in Figure 3.19, and Figures 3.21b, 3.22b, 3.23b, and 3.24b show the response predicted by the model. For example, Figure 3.21a shows the four different magnitudes of temperature impulse (125%, 100%, 50%, and 25%) followed by a constant gas temperature of approximately 487 K for TEST116 upstream sensor #1. Figure 3.21b show the nondimensional error (i.e. error/gas temperature) predicted by the model for the different inputs of Figure 3.21a. Figures 3.22, 3.23, and 3.24 show similar results for tests TEST112 upstream sensor #3, TEST116 downstream sensor #1, and TEST112 downstream sensor #4, respectively. Two observations can be made based on the results presented in these figures. First, the average error predicted from 450–500 msec for the four cases was 0.12%. Second, the average of the maximum difference between the 125% case and 0% case for each test is 0.0375% (i.e. 30% of the magnitude of the average error). In other words, the difference in error predicted for cases with an impulse and cases without an impulse is small compared to the magnitude of the error predicted.

Therefore, the magnitude of the impulse is deemed unimportant relative to the magnitude of the error. Now let us consider the magnitude of the error

itself, 0.12%. This error predicted by the model amounts to less than 0.6 K upstream and about 0.4 K downstream. These magnitudes are also worst case estimates of the error since, for all other heated tests, the probes' initial temperatures were closer to the steady state test temperatures. Therefore, we can say with confidence that these measurement error estimates are conservative.

3.6 – Total Temperature Uncertainty Estimation

In this section we will estimate the contributions to the uncertainty in the total temperature measurement. These will consist of four parts: calibration error, short term drift, long term drift, and measurement error.

3.6.1 – Calibration Procedure

At this point, a brief description of the calibration procedure is in order. The probes are calibrated in a stirred and heated bath (the fluid is electrically inert) relative to a local reference standard. The procedure is as follows. Initially the fluid is heated to its upper temperature, usually around 420 K, with the probes placed in the bath center along with a reference thermometer and a reference RTD. The bath is covered to reduce heat losses to the surroundings. The stirred bath is then cooled to room temperature at the rate of about 1 K every two minutes. This slow process is necessary to account for the large time constants of the thermometer and the RTD. The output of the rakes and the RTD are recorded by the A/D system just as for a test. The thermometer output is input to the A/D at an amplification of 10 mvolts/K. A least squares method is used to determine the calibration curve (assumed a straight line) of the rakes versus the two standards. The best fit line approximation is accurate to better than 0.1 K

over the entire range of the calibration.

For one sensor, the calibration procedure was repeated three consecutive times to determine the repeatability of the calibrations. In other words, since the voltage output from three calibrations varied from -4.0 volts to 0.0 volts, the calibration curves obtained from these three calibrations are compared over that range to see how much they varied. The maximum variation between the three calibrations amounted to 0.13 K. In addition, an estimate of the nonlinearity of the sensors is of interest. To estimate this, the same three calibrations were used to determine the temperature which the sensor would indicate at the limit of the A/D resolution (5.0 volts). The maximum indicated difference at 5.0 volts for the three calibrations was 0.27 K. Note that the proper way to estimate the nonlinearity error is to calibrate the sensor over a larger temperature range and compare the results of that calibration to a calibration over a limited temperature range. This has not been done.

3.6.2 - Short Term Drift and Long Term Drift

In addition to the above experiment, another experiment was performed to determine the short term drift of the sensor. This was done by placing the prototype probe in the same bath described above for a period of 100 hours. The bath was maintained at the same temperature and the difference between the reference RTD and the sensors was recorded periodically. The results of the experiment are shown in Figure 3.25. Note that the sensors remained stable to within 0.25 K. The environment temperature was intentionally varied from 12-25 ^{o}C over the course of the test (by opening the large sliding door in the BDT area in the dead of a Boston winter). This was done to determine the effects of the environment temperature on the electronics since the environment temperature is

not controlled in the BDT test area. The spikes in the measurements correspond to a 24-hour cycle. This implies that temperature control (or at least insulation) of the electronic package may improve stability.

The long term drift was evaluated by performing a bath calibration just prior to the beginning of the test runs and then again just after the completion of the test runs 3 months later. Just as for above, the calibration curves were compared for the two calibrations over the range of temperatures experienced by the sensors. On average, the calibrations repeated to within 0.36 K.

3.6.3 - Uncertainty Estimate for the RTDF Generator Tests

The estimate of the uncertainties in the total temperature measurement for the RTDF tests is given here. The total error for the measurement becomes a function of the calibration error , the short and long term drift, and the measurement error. As for the total pressure measurement, these errors are uncorrelated so that the root mean square should be taken. This error is termed the absolute error. On a test to test basis, the calibration error vanishes and leaves the short and long term drift error and measurement error. This is termed the relative error.

The calibration error is taken as the 0.27 K maximum variation found between repeated calibrations. The short term drift is the 0.25 K day to day variation shown in Figure 3.25. The long term drift is taken as the 0.36 K change between calibrations. The measurement error is taken as the 0.12% found by the model. Table 3.3 shows the tabulated values of the errors in absolute and relative terms. Note that the conditions are expressed on a percent basis ($\Delta T/T$) using the nominal upstream and downstream conditions.

Table 3.3 - Uncertainties in Total Temperature Measurement %

Location/ Conditions	Cal	Short Term Drift	Long Term Drift	Model	Total
Upstream* ($M=0.07, T_t=478$ K)	0.0565	0.0523	0.0753	0.12	0.161
Upstream++ ($M=0.07, T_t=478$ K)	-	0.0523	0.0753	0.12	0.151
Downstream* ($M=0.6, T_t=343$ K)	0.0787	0.0729	0.1050	0.12	0.192
Downstream++ ($M=0.6, T_t=343$ K)	-	0.0729	0.1050	0.12	0.175

* absolute
++ relative

Chapter 4 - Uncertainty Analysis for Efficiency

4.1 – Introduction

The previous two chapters have considered the details of the total pressure and temperature measurements in the BDT for the RTDF generator tests. Each chapter concluded with a net uncertainty estimate for the quantity of interest: upstream total pressure, downstream total pressure, upstream total temperature, and downstream total temperature. This was done in order to determine how the uncertainties in the measurements can affect a calculation which uses the results. Since the ultimate goal is to determine the effect of inlet temperature profiles on turbine efficiency, the purpose of this chapter is to perform an uncertainty analysis for the adiabatic efficiency η. Essentially, the uncertainty estimates of the two previous sections are used to determine the net uncertainty in η. See references [25]–[31] for a set of detailed discussions on uncertainty analysis (i.e. its definition and importance in experiments, proper procedures, and examples of its applications).

This chapter has three goals. First, the definition of η in an uncooled turbine stage is stated, and a correction for the η calculation which is peculiar to a short duration facility is discussed. Second, the uncertainty of η is determined as a function of uncertainties in temperature ratio τ, pressure ratio π, and ratio of specific heats γ. This calculation gives the influence coefficients for τ, π, and γ. Third, the uncertainty estimates of Chapters 2 and 3 are used to determine the uncertainties in τ, π, and γ. These are then used to determine the total uncertainty in η.

4.2 – Definition of Adiabatic Efficiency

The definition of adiabatic efficiency is given in [32] as:

$$\eta = \frac{1 - \tau}{1 - \pi^{\frac{\gamma-1}{\gamma}}} \qquad (4.1a)$$

where

$$\tau = \frac{T_{t\ avg_{downstream}}}{T_{t\ avg_{upstream}}} \qquad (4.1b)$$

and

$$\pi = \frac{P_{t\ avg_{downstream}}}{P_{t\ avg_{upstream}}} \qquad (4.1c)$$

One assumption which is implicit in Eqn 4.1 is that the turbine is adiabatic. In the blowdown turbine, however, this is not the case (remember that the facility was built for the purpose of measuring heat transfer). Because of the heat transfer to the blades, endwalls, rotor, etc., the net effect is that a lower total temperature is measured at the stage exit than would be the case if the stage were adiabatic. This results in a lower τ and, consequently, a higher η. This non-adiabatic effect can be calculated and corrected for. According to [1], the correction is on the order of 1%. However, this correction is not accounted for in the analysis and results which are presented in this chapter and Chapter 5.

4.3 – Uncertainty Analysis

Since η is a function of temperature ratio, pressure ratio, and ratio of specific heats, we may use a Taylor series expansion (truncated after one term) to write a small change in η as a function of small changes in the independent variables: $\Delta\tau$, $\Delta\pi$, and $\Delta\gamma$:

$$\Delta\eta = \frac{\partial\eta}{\partial\tau}\Delta\tau + \frac{\partial\eta}{\partial\pi}\Delta\pi + \frac{\partial\eta}{\partial\gamma}\Delta\gamma \qquad (4.2)$$

Or, in terms of percentage changes, as:

$$\frac{\Delta\eta}{\eta} = \frac{\partial\eta}{\partial\tau}\frac{\tau}{\eta}\frac{\Delta\tau}{\tau} + \frac{\partial\eta}{\partial\pi}\frac{\pi}{\eta}\frac{\Delta\pi}{\pi} + \frac{\partial\eta}{\partial\gamma}\frac{\gamma}{\eta}\frac{\Delta\gamma}{\gamma} \qquad (4.3)$$

Since the uncertainties in τ, π, and γ are not correlated, the root mean square of these quantities are used. Calculating the partial derivatives, substituting for each of the terms on the right hand side of Eqn. 4.3, and simplifying gives:

$$\left\{\frac{\partial\eta}{\partial\tau}\frac{\tau}{\eta}\frac{\Delta\tau}{\tau}\right\}^2 = \left\{\frac{\tau}{(1-\tau)}\right\}^2\left\{\frac{\Delta\tau}{\tau}\right\}^2 \qquad (4.4)$$

and

$$\left\{\frac{\partial\eta}{\partial\pi}\frac{\pi}{\eta}\frac{\Delta\pi}{\pi}\right\}^2 = \frac{\pi^{2\left(\frac{\gamma-1}{\gamma}\right)}}{\left(1-\pi^{\frac{\gamma-1}{\gamma}}\right)^2}\left\{\frac{(\gamma-1)}{\gamma}\right\}^2\left\{\frac{\Delta\pi}{\pi}\right\}^2 \qquad (4.5)$$

and

$$\left\{\frac{\partial\eta}{\partial\gamma}\frac{\gamma}{\eta}\frac{\Delta\gamma}{\gamma}\right\}^2 = \frac{\pi^{2\left(\frac{\gamma-1}{\gamma}\right)}(\ln\pi)^2}{\left(1-\pi^{\frac{\gamma-1}{\gamma}}\right)^2\gamma^2}\left\{\frac{\Delta\gamma}{\gamma}\right\}^2 \qquad (4.6)$$

where the first terms on the right hand side of Eqns. 4.4, 4.5, and 4.6 are defined as the influence coefficients. Using the definitions of the influence coefficients, the final uncertainty (on a percent basis) can be written as:

$$\frac{\Delta\eta}{\eta} = \{ c_\tau \left(\frac{\Delta\tau}{\tau}\right)^2 + c_\pi \left(\frac{\Delta\pi}{\pi}\right)^2 + c_\gamma \left(\frac{\Delta\gamma}{\gamma}\right) \}^{1/2} \qquad (4.7)$$

There are some interesting points to make concerning the influence coefficients. From Eqn. 4.7 one can see that the size of the influence coefficients dictates the importance of the percent uncertainty in temperature ratio, pressure ratio, and γ. Consider the coefficient of $\Delta\tau/\tau$ first. According to Eqn 4.4, the influence coefficient can be written as

$$c_\tau = \{ \frac{\tau}{(1-\tau)^2} \}^2 = \{ \frac{T_{down}}{\Delta T} \}^2 \qquad (4.8)$$

Note that the coefficient is inversely proportional to the square of ΔT. In other words, for low work turbines, it becomes increasingly difficult to measure efficiency accurately regardless of the accuracy of the temperature measuring probe. Table 4.1 shows typical values of the coefficients for nominal values of τ, π, and γ in the BDT.

Table 4.1 - Influence Coefficients for Efficiency Calculation

quantity	typical value
τ	0.741
π	0.243
γ	1.313
c_τ	8.185
c_π	0.353
c_γ	7.217

From the table, it becomes obvious that the critical link in the accurate estimation of η (for the current turbine configuration) is the measurement of total temperature. Table 4.1 also shows that uncertainties in γ are almost as critical as those for temperature. This fact can be easily overlooked, but percent uncertainties in γ are usually smaller than that of τ and π. These ideas are

clearer in graphical form. A three–dimensional plot of percent uncertainty in efficiency versus the percent uncertainties in τ, π, and γ would show surfaces of constant uncertainty moving away from the origin (where zero uncertainty in all quantities gives zero uncertainty in η). If the influence coefficients were equal for τ, π, and γ, then the surfaces would be spherical with radii equal to the influence coefficients. For cases with different influence coefficients for τ, π, and γ, the surfaces become skewed. Because the three–dimensional picture becomes crowded, two–dimensional slices are shown in Figures 4.1 through 4.3. Lines of constant percent uncertainty in η are drawn versus percent uncertainty in τ and π for particular values of percent uncertainty in γ (0.0%, 0.1%, and 0.2% respectively).

There are three interesting points about the figures. First, as expected, Figure 4.1 shows zero uncertainty in η when there is no uncertainty in any of the three quantities. Second, the lines of constant percent uncertainty in η are nearly vertical for values of percent uncertainty in τ greater than 0.15. This reiterates the importance of accurate temperature measurements for the current BDT configuration. Third, each 0.1% increment in γ uncertainty results in a 0.25% increment in η uncertainty. This shows that precise knowledge of γ is required for accurate absolute estimates of η. For gases γ is essentially a function of temperature only. In the BDT, where the gas is a mixture of argon and freon, precise knowledge of the gas mixture is also required to determine γ accurately.

What is an estimate in the uncertainty of γ ? Since the exact value of γ is a function of the gas mixture used in the tests, an estimate of the uncertainty in γ can be obtained by determining how a small change in freon mass fraction XF affects its value. This can be expressed as:

$$\frac{\Delta\gamma}{\gamma} = \frac{1}{\gamma}\frac{\partial\gamma}{\partial XF}\Delta XF \qquad (4.9)$$

Using typical values and a 1% change in XF gives a value of $\Delta\gamma/\gamma = 0.20\%$. Since the filling of the supply tank has a systematic procedure associated with it, only random fluctuations affect the gas mixture. Thus, the relative percent uncertainty in γ should be smaller than this value and is taken as 0.10%.

4.4 - Uncertainty Estimate for η

This section calculates the estimates of uncertainty for τ and π using the uncertainty estimates of total pressure and temperature given in Chapters 2 and 3. Using the definition of τ given in Eqn. 4.1b, the percent uncertainty in τ can be written (repeating the above analysis) as:

$$\frac{\Delta\tau}{\tau} = \left\{ \left(\frac{\Delta T_{t\ avg_{downstream}}}{T_{t\ avg_{downstream}}}\right)^2 + \left(\frac{\Delta T_{t\ avg_{upstream}}}{T_{t\ avg_{upstream}}}\right)^2 \right\}^{1/2} \qquad (4.10)$$

and, similarly, the percent uncertainty in π can be expressed as:

$$\frac{\Delta\pi}{\pi} = \left\{ \left(\frac{\Delta P_{t\ avg_{downstream}}}{P_{t\ avg_{downstream}}}\right)^2 + \left(\frac{\Delta P_{t\ avg_{upstream}}}{P_{t\ avg_{upstream}}}\right)^2 \right\}^{1/2} \qquad (4.11)$$

Finally, the percent uncertainties in the total pressure and total temperature are inserted into Eqns. 4.10 and 4.11 to give the percent uncertainty in τ and π. The resulting values can then be substituted into Eqn. 4.7 to determine the net uncertainty in efficiency. Table 4.2 presents these results on a relative basis. As one can see from the table, the net uncertainty in efficiency is just below 1.0% which is higher than the 0.25% typically required for performance estimation.

Table 4.2 - Uncertainty Calculation for Efficiency

Quantity	Source	% uncertainty
$P_{t\ upstream}$	Table 2.4	0.830
$P_{t\ downstream}$	Table 2.4	0.720
$T_{t\ upstream}$	Table 3.3	0.151
$T_{t\ downstream}$	Table 3.3	0.175
γ	Eqn. 4.9	0.100
τ	Eqn. 4.10	0.231
π	Eqn. 4.11	1.099
η	Eqn. 4.7	0.967

Chapter 5 - Effects of Inlet Temperature Profiles on the Stage Performance

5.1 - Introduction

The previous chapters have considered in detail the measurements of total pressure and temperature for the purpose of assessing the effects of inlet radial temperature profiles on the stage performance. This chapter explains how this problem was addressed. Essentially, the RTDF generator was used to generate axisymmetric radial total temperature profiles at the inlet to the turbine, and the probes described in the previous chapters were used to measure the inlet and exit conditions of the stage at a fixed radial location. Thus, an uncertainty may be introduced due to the fact that the probes were not traversed circumferentially. The magnitude of this uncertainty has not been estimated. The resulting data was then used to characterize the stage performance (i.e. determine the corrected flow, corrected speed, and the average stage efficiency).

This chapter consists of five parts. First, the motivation for the experiment is given along with a discussion of some previous work on this problem. Second, the RTDF generator is described. Third, the data analysis technique is presented. Fourth, the results of the experiments are presented. Finally, the chapter is concluded with a discussion of the results in light of the the error analysis presented in the previous chapter.

5.2 - Background

Most experimental turbine aerodynamic studies use uniform inlet radial temperature profiles for the sake of simplicity. As one might expect, however, the uniform profiles do not represent the true inlet conditions to a turbine during engine operation. In general, the inlet conditions are spatially nonuniform and can also vary with time. Although the nonuniformities are strongly dependent on the type of combustor design chosen, typical inlet profiles exhibit large radial variations. These radial temperature profiles are a direct result of the trend toward higher turbine inlet temperatures (in order to improve cycle performance). The resulting higher combustor exit temperatures require large amounts of cooling air near metal surfaces to maintain the temperatures within acceptable levels. For this reason, the core flow is maintained at high temperature while the flow adajacent to the surfaces bounding the flowpath is at a lower temperature resulting in radial variations in inlet total temperature.

What are the effects of these radial variations? Previous studies, [33] and [34], have found that the inflow temperature nonuniformities result in the migration of hot gas toward the pressure side and cold gas toward the suction side of the rotor blade. This effect can be explained by the difference in the rotor relative frame inlet flow angles as discussed by Kerrebrock and Mikolajczak [35]. In addition, both studies observed large radial migrations in the rotor near the hub and tip endwall regions due to strong secondary flows induced by the inlet temperature profiles. These effects, combined with observations that rotor airfoil pressure sides are subjected to higher heat loads than suction sides, raise concerns about high, localized heat transfer rates on the the pressure side of airfoils and the endwall regions.

The studies mentioned above concentrated on the details of the flowfield but did not give any mention of the effects of the profiles on the performance of the turbine. It is this topic which this chapter addresses.

5.3 - Description of the RTDF Generator

We start by discussing briefly the design of the RTDF ("Radial Temperature Distribution Factor") generator. See [5] for a detailed discussion of its design. The goal of the RTDF generator is to develop different levels of inlet temperature nonuniformities. This nonuniformity is characterized by a nondimensional number which will be called the RTDF and is defined as:

$$RTDF = \frac{(T_{max} - T_{mean})}{T_{ref}} \cdot 100 \qquad (5.1)$$

where T_{max} = the maximum total temperature, T_{mean} = the mass averaged inlet total temperature, and T_{ref} is a typical combustor temperature rise (1010 K) scaled by the BDT temperature scaling (310 K / 1118 K). The temperature scaling comes from the requirement that the ratio of the mean metal temperature to the mean gas temperature must be the same in both the scaled facility and the full scale facility for dynamic similarity of the flowfields. The RTDF, then, nondimensionalizes the temperature nonuniformity by the scaled ΔT_t of a typical combustor (1010*310/1118=280.1). In addition, the inlet total pressure profile should be uniform so that total pressure gradient driven secondary flows can be distinguished from total temperature gradient driven secondary flows (although both may be present in a real engine environment). Another goal of the generator was to provide the turbine with a temperature profile which is constant over the steady test time. This determines the physical size of the machine once a material is selected.

Given these requirements, the final configuration of the generator was as follows. It is a 20" long honeycomb stainless steel structure which is electrically

heated in vacuum prior to test. The generator was also plumbed so that the supply tank heating oil could be used to set the boundary conditions of the heat exchanger (i.e. there is an inner and outer jacket for the oil which surrounds the flow area). It is placed between the valve and the front flange (approximately 14" from the upstream measuring station). The generator consists of three 120° heater sections which nominally require 3 kilowatts of power each. Thus, the generator can be used to generate non-axisymmetric temperature profiles (although this was not done for the tests discussed below). The three sectors of the generator are monitiored during heating by thermocouples which are imbedded throughout the honeycomb matrix. The output of the thermocouples is stored in a Digital Equipment Corp μVAX and displayed on a terminal for online monitoring.

5.4 - The RTDF Experiments

5.4.1 - Goal of the Experiments

This sections describes the goal of the RTDF experiments performed in the BDT and the problems encountered. Seven tests were performed in the BDT with the idea of operating the turbine at its design corrected mass flow condition and two different corrected speed conditions (100% and 120%). For each corrected speed condition, a different RTDF level as defined above would be used as the inlet condition to the turbine. Given the measured inlet and exit radial total pressure and temperature profiles, the average turbine stage efficiency could be determined and correlated with the RTDF.

Unfortunately, however, this proved to be a difficult task. The main reason for this is the "learning curve" associated with the simultaneous shakedown and

use of the RTDF generator. As with any mechanical equipment, the performance of the generator needed to be characterized experimentally. The outlet gas temperature of the generator, for example, affects the corrected speed of the test. In turn, the mechanical speed and brake power must be set accordingly to provide the desired corrected speed. This proved to be difficult since the "firing" temperature profile of the generator is a function of the heating history and the boundary conditions of the generator. Thus, the "average" temperature which will be seen at the turbine inlet (and, therefore, the corrected speed) was difficult to assess until just prior to the the test time. Meeting the corrected speed goal requires some last minute calculations to set the turbine mechanical speed and the eddy current brake power. The end result is that the corrected speed varied slightly from the desired value .

5.4.2 – Method of Data Analysis

This section describes the procedure followed to calculate the %design corrected flow, %design corrected speed, and the stage efficiency. First, consider %design corrected mass flow, $m_{corr\ \%design}$. This is defined as:

$$\frac{\overset{o}{m}_{corr}}{\overset{o}{m}_{corr\ design}} = \frac{\left\{ \dfrac{\overset{o}{m}\ (\gamma R T_t)^{1/2}}{P_t\ A} \right\}}{\left\{ \dfrac{\overset{o}{m}\ (\gamma R T_t)^{1/2}}{P_t\ A} \right\}_{design}} \qquad (5.2)$$

where T_t and P_t in the numerator are averaged quantities for the inlet; γ and R are determined from the gas mixture and static temperature T; m is the mass flow calculated from the 1D choked flow assumption; and the denominator is the design value of the quantity. Note that the area A cancels in this calculation.

The %design corrected speed $N_{corr\ design}$ is defined as:

$$\frac{N_{corr}}{N_{corr\ design}} = \frac{\dfrac{N\ D}{(\gamma R T_t)^{1/2}}}{\left\{ \dfrac{N\ D}{(\gamma R T_t)^{1/2}} \right\}_{design}} \qquad (5.3)$$

where N is the rotor mechanical speed and the denominator is the design value for the turbine. Again, as for the area in Eqn. 5.2, the turbine diameter cancels in the calculation.

The turbine stage efficiency is calculated as defined in Eqn. 4.1. The temperature ratio τ and pressure ratio π are calculated from time-averaged total temperature and total pressure measurements (450 to 500 msec), and γ is the arithmetic mean of the upstream and downstream γ. The total temperature and total pressure measurements may be arithmetically averaged which corresponds to an area average or mass weighted to obtain the traditional mass average.

In order to calculate mass averaged quantities, some assumptions must be made. This is because a mass weighted average requires knowledge of the mass flow distribution at a given axial location. In other words, a mass average requires knowledge of the velocity distribution along the span. Unfortunately, the facility was not instrumented to provide this information. As a result, in order to estimate the mass averaged quantities, the following assumptions were made for the upstream and downstream stations.

For the upstream case, the gas passes through the generator whose 20" long honeycomb tubes serve as flow straighteners. In addition, the upstream measuring station should be far enough downstream that any nonuniformities should mix out. As we will see, the upstream total pressure profile is uniform to within 1-2% across the span. The boundary layer bleeds are just upstream of the measuring plane so that the viscous and thermal boundary layers are bled off

prior to entering the inlet. As a result, the upstream static pressure is assumed to be uniform across the duct (the streamlines have no curvature) and is calculated from the following relation:

$$\frac{P_t}{P} = \left(1 + \frac{\gamma-1}{2} M^2 \right)^{\frac{\gamma}{\gamma-1}} \qquad (5.4)$$

where P_t is the average upstream total pressure and M is determined by the relation between the duct area and the NGV throat area:

$$\frac{A}{A^*} = \frac{1}{M} \left\{ \frac{1 + \frac{\gamma-1}{2} M^2}{\frac{\gamma+1}{2}} \right\}^{\frac{\gamma+1}{2(\gamma-1)}} \qquad (5.5)$$

The variation in static temperature across the duct is then found from the relation:

$$\frac{T_t}{T} = 1 + \frac{\gamma-1}{2} M^2 \qquad (5.6)$$

In essence the upstream weighting amounts to accounting for density variations across the annulus. Once the Mach number distribution is known, the mass flow across the annulus can be calculated and used to obtain the mass average of a generic quantity Q:

$$Q_{\text{mass avg}} = \frac{\sum_i (\rho V A)_i \, Q_i}{\sum_i (\rho V A)_i} \qquad (5.7)$$

For the downstream position, the flow is, in general, three dimensional. For lack of any better information, the results of streamline curvature simulations were used to give the static pressure distributions for the experiments at the downstream measuring station. The distributions were scaled by a measurement of static pressure at the tip endwall. Using Eqn. 5.4 and the static pressure at the point

of the total pressure measurements, a Mach number distribution was determined. The exit flow angles from the streamline curvature calculation are then used to determine the axial velocity components along the span. Eqn. 5.6 gives the static temperature distribution using the total temperature measurements. At this point, the mass flow distribution is calculated and compared to the upstream value. Assuming no losses of gas in the rotor, the axial velocity is scaled up or down so that continuity is satisfied. Finally, the mass weighted quantities are calculated using Eqn. 5.7. It must be emphasized that true mass weighting should incorporate an angle probe traverse across the span to determine the velocity distribution.

5.5 - The Results

Figures 5.1 through 5.7 present the time-averaged (450-500 msec) upstream and downstream total pressure data for the seven experiments (labelled "TEST11#"). The inlet total pressure variation ΔP_t is between 1.0% and 1.5% of the inlet total pressure. This is true for cases both with and without the inlet temperature profiles (TEST112 and TEST115). The key point here is that the inlet total pressure profiles are the same for the cases with and without inlet temperature profiles. As for the level of inlet distortion, the Mach number is about 0.0695 so that $\frac{1}{2}\rho V^2$ is small. In particular, the variation of total pressure nondimensionalized by the dynamic head is given by the relation :

$$\frac{\Delta P_t}{\frac{1}{2}\rho V^2} = \frac{\Delta P_t}{P_t} \cdot \frac{\left(1 + \frac{\gamma-1}{2} M^2\right)^{\frac{\gamma}{\gamma-1}}}{\frac{\gamma}{2} M^2} \qquad (5.8)$$

For the nominal upstream values of the seven experiments (M=0.0695, γ=1.28, and

P_t=3.5 atm), this amounts to about 4.4.

Figures 5.8 through 5.14 present the total temperature profiles at the turbine inlet and exit of the stage. Using the definition of the RTDF, one finds that the inlet temperature distortion varied from about 2% to 20%. The figures show that the exit profiles are nearly mixed out (four axial chord lengths from the rotor trailing edge).

It is of interest to note that the inlet temperature profiles are nearly parabolic in shape (as designed). A least squares calculation of the best fit parabola to the inlet temperature profiles was performed for each of the tests with an inlet profile. Figures 5.15 through 5.19 show both the fitted profiles and the measured profiles vs. radial location. The fit was based on the five temperature measurements (K) and the radial locations of the five sensors (inches). The equations of the profiles are also included.

Table 5.1 shows a summary of the inlet and exit conditions of the stage for the seven tests. The notation is as follows : M is the Mach number, T_t is the total temperature (K), P_t is the total pressure (atm), γ is the ratio of specific heats, subscript 2 designates the upstream station, and subscript 5 designates the downstream condition. Note that the inlet Mach number was the same for all of the tests which is a consequence of the choked condition. In addition, the inlet total pressure was nearly the same for the tests as well. The inlet total temperature varied for the tests in order to change the corrected speed of the turbine.

Table 5.1 - Average Conditions for the RTDF tests++

TEST	M_2	T_{t_2}	P_{t_2}	γ_2	M_5	T_{t_5}	P_{t_5}	γ_5
110	0.070	480.6	3.4064	1.278	0.658	371.2	0.9059	1.345
111	0.070	455.8	3.4028	1.282	0.557	337.6	0.8240	1.344
112	0.070	435.3	3.4029	1.286	0.546	322.1	0.8201	1.349
113	0.070	459.0	3.5175	1.281	0.557	336.9	0.8472	1.345
114	0.070	429.5	3.5174	1.287	0.553	322.1	0.8671	1.350
115	0.070	420.6	3.3422	1.289	0.544	315.3	0.8194	1.352
116	0.070	532.1	3.5253	1.272	0.580	396.6	0.8509	1.327

++ data averaged from 450-500 msec

Given these conditions and the data analysis technique described above, we can calculate the corrected conditions for the tests. Table 5.2 presents a summary of these. The last column in the table gives the net uncertainty in the efficiency (the value is obtained by multiplying the %uncertainty in efficiency given in Table 4.2, $\Delta\eta/\eta$, by the corresponding value for η). The net uncertainty in efficiency is seen to be about 0.85%.

In addition, the table shows that the turbine operated at its design corrected flow condition for all of the tests. For three tests, TEST111, TEST112, & TEST113, the goal of 120% of the design corrected speed was achieved to within +/- 1.8%. Also, tests TEST114 and TEST115 were within a percent of the 100% design corrected speed goal. Only two tests, TEST110 and TEST116, missed their mark. TEST110 missed due to inexperience with the generator, while TEST116 fell below the 120% goal due to the high inlet temperature level for that test.

Table 5.2 - Summary of Blowdown Turbine RTDF Tests

TEST	RTDF	% design corr flow	$\frac{1}{\pi_t}$	% design corr speed	η_{mass}	η_{area}	$\Delta\eta$
110	5.2	99.0	3.76	85.5	84.3	84.2	0.82
111	9.8	99.0	4.13	119.1	90.4	90.4	0.87
112	2.2	99.0	4.15	121.8	89.5	89.7	0.87
113	15.1	99.0	4.15	119.4	92.4	92.8	0.89
114	17.2	99.0	4.06	99.3	87.1	87.4	0.84
115	1.5	99.0	4.08	100.9	86.6	86.7	0.84
116	20.8	98.0	4.14	112.3	91.2	91.4	0.88

5.6 - Discussion of the Results

5.6.1 - Significance of the Results

In this section we will discuss the significance of the results. In particular, three items are addressed: (1) the effect of corrected speed on efficiency; (2) the effect of RTDF inlet temperature profiles on efficiency; and (3) the difference between the mass averaged efficiency and the area averaged efficiency.

First, the results agree with previous test data which show that the test turbine operates more efficiently at higher corrected speeds. For example, TEST112 and TEST115 have nearly the same corrected flow, pressure ratio, and RTDF, but the corrected speed is 20% higher for TEST111. This results in a 2.9% increase in efficiency.

Second, the effects of the inlet temperature can be seen. Figure 5.20 shows a plot of the mass averaged stage efficiency (with the corresponding error bars) vs. RTDF. For TEST111, TEST112, and TEST113 the corrected speed is 120% to within a few percent. As the RTDF is increased from 2.2% to 15.1%, an increase in efficiency is seen. For one comparison (120% speed line where the RTDF is

increased from 9.8% to 15.1%) the change in efficiency is 2.0%. This change is greater than the uncertainty estimate. Thus, higher inlet temperature distortions at the same corrected conditions result in a higher efficiency. For two other comparisons (the 120% speed line where the RTDF is increased from 2.2% to 9.8% and the 100% speed line where the RTDF is increased from 1.5% to 17.2%), the slight increase in efficiency is less than the uncertainty estimate so that no conclusions can be drawn concerning the effect of the inlet temperature distortion for these cases. It is worthwhile to note that great care has been taken to insure conservative estimates of the uncertainty in the efficiency calculation. As seen in previous chapters, the best way to reduce the magnitude of this uncertainty is to reduce the uncertainty in the temperature measurement. Table 3.3 showed that the dominant error term for the temperature measurement is the error predicted by the model. Given sufficient confidence in the model, then, this error can be corrected for. Thus, the remaining uncertainty in the temperature measurement would be due soley to other factors such as short term drift, long term drift, and calibration errors so that the net uncertainty in efficiency would be reduced.

It should be mentioned here that the mixed out exit temperature profiles shown in Figures 5.8 through 5.14 agree with the results of the NASA study [34] mentioned earlier. Their results showed that an inlet temperature profile (with an equivalent RTDF of approximately 16%) was mixed out about 2.3 axial chord lengths downstream of the rotor trailing edge.

Third, in spite of the assumptions which were made to calculate mass averaged quantities, the agreement between the straightforward area averaged efficiency and the mass averaged efficiency is between 0.0 and 0.4% for all the tests. This difference is smaller than the estimated uncertainty in the efficiency calculation.

5.6.2 – Qualitative Explanations of the Results

In this section, a qualitative explanation for the effects of the inlet temperature profiles on turbine efficiency is presented. The results of [33] and [34] indicated that the secondary flows which are induced by inlet total temperature profiles can be significant. In particular, they found that inlet total temperature profiles cause large radial migration of hot fluid toward the hub and tip endwall regions in the rotor passage. Is it possible, then, that this effect was present for the RTDF tests? If the contribution to the secondary flows from total pressure variations at the inlet are the same for the cases with and without inlet temperature profiles, then any additional secondary flows which are present are due to the inlet total temperature gradient. In an effort to determine if radial redistribution of fluid in the stage could have occured, the efficiency was calculated on a percent span basis (e.g. a streamline which is at the 50% span location at the turbine inlet is assumed to leave the stage at the 50% span location) for TEST112 and TEST113. As shown in Table 5.2, the only difference between these two tests is that TEST113 has a substantially higher RTDF (15.1% compared to 2.2%). The inlet and exit total pressure and total temperature measurements are linearly interpolated to obtain values at the same percent span locations and are then used to calculate the efficiency for that percent span location as a function of time. Figure 5.21 shows the results for the two tests. The efficiency is plotted versus the percent span location. The figure shows that the case without the inlet temperature profile has a variation in efficiency of about 6% along the span while the case with a 15.2% RTDF indicates a variation of about 35% along the span. This case also shows efficiencies in excess of 100% which is highly unlikely. This result suggests that the inlet temperature

profile has significantly altered the flowfield through the stage (since the inlet total pressure profiles are nearly identical for the two tests). If radial redistribution of fluid is the culprit, then measurements of the heat flux to the tip shroud should verify this [5]. Note also that if large radial flows are present, then the flow angles calculated in the streamline curvature analysis may be in error.

Chapter 6 - Conclusions

This thesis has addressed four subjects which are now reviewed. First, the design of a total pressure probe was presented which would allow accurate time-average measurements of the total pressure downstream of the turbine rotor. The probe uses Kulite strain gauge differential pressure transducers which are mounted external to the flowfield. The frequency response was satisfactory (with an estimated cutoff frequency of 280 Hz and a 1 atm step input response on the order of 25 msec). The net uncertainty of the probe was found to be about 0.72%, most of which is due to the disagreement between the sensors at the end of the 300 sec test time. The maximum difference between any two sensors was taken as the short term drift which amounted to an average value of 0.66%. The magnitude of this uncertainty is substantially reduced if a pressure variation does actually exist.

Second, the design of total temperature probes is discussed which use 20 μm diameter disc thermocouple junctions on 50 L/D quartz insulated supports. The probes use AD597AH preamps for electronic ice point compensation and amplification, and the probe body is heated as close as possible to the approximate gas temperature to reduce the magnitude of the probe conduction error and improve the probe response. An analytical model of the temperature probe was described which can predict the temperature indicated by the probe to $\sim$ 0.2%. The model uncertainty can be reduced by improving the information to the model. Applying the probe model to the RTDF configuration showed that the probe error was 0.12% at 450 msec. The net uncertainty of the probes were estimated to be 0.151% for the upstream probe and 0.175% for the downstream probe so that the total uncertainty in the calculation of the total temperature

ratio τ is 0.23%. Some ways to reduce the magnitude of this uncertainty were already discussed and are summarized again here. First, the electronics package can be improved by using automatic ice point compensators or alternatively, by isolating it from its surroundings in order to reduce the short term stability fluctuations. A second way to reduce the uncertainty magnitude is by improving the the accuracy of the experimental data which is input to the model (i.e. the inlet gas temperature). A third, more painful, but effective, way to reduce the error is by calibrating the thermocouple rakes more often in order to reduce the long term drift errors. For example, if these errors are reduced in half, then the overall uncertainty in the temperature measurement is reduced in half from 0.23% to 0.115% which has, as we will see shortly, quite a substantial effect on the uncertainty in efficiency.

Third, an error analysis of the efficiency calculation was performed to determine the relative importance of temperature ratio τ, pressure ratio π, and ratio of specific heats γ for the current test turbine. The error analysis showed that the influence coefficients for τ, π, and γ are 8.2, 0.35, and 7.2, respectively. This shows that the penalty for errors in τ is approximately 25 times greater than that for π. In addition, the estimation of γ is almost as important as the estimation of τ. The uncertainty in γ was estimated to be about 0.1% from test to test. Thus, the relative contributions of uncertainties in τ, π, and γ to the uncertainty in η are 0.66, 0.65, and 0.27, respectively. This shows that the contributions from the temperature measurement are essentially the same as for the pressure measurement while contributions from γ are less than half of the other two. The net uncertainty in efficiency was 0.85%. Although this value is higher than the 0.5% or better value typically required for engine performance calculations, improvements in the temperature and pressure measurements should reduce the uncertainty to values approaching 0.5%. Should the efforts be

concentrated on the total pressure, total temperature, or both ? A brief inspection of Figure 4.2 provides the answer to this question. The figure shows that efforts to reduce the uncertainty in π (i.e. pressure) are largely fruitless. For example, current uncertainty estimates place the "region of interest" in an area where the percent uncertainty contours of efficiency are nearly vertical so that reducing the uncertainty in the pressure measurement to zero would reduce the magnitude of the error bars by only 0.15% to $\sim$ 0.7%. Reductions in the uncertainty of τ, however, is much more beneficial. The figure shows that cutting the magnitude of the uncertainties in τ in half to 0.115% reduces the magnitude of the uncertainty in η to $\sim$ 0.4%. Therefore, efforts to reduce the overall uncertainty in η are best spent by reducing the errors in the total temperature measurement.

Finally, experiments to determine the effects of inlet radial temperature profiles on stage performance were successfully carried out using the above probe designs and the RTDF generator. In particular, a comparison between two test which had identical corrected conditions but different inlet temperature profiles revealed that an increase in the RTDF from 9.8% to 15.1% resulted in a 2.0% increase in efficiency (which is higher than the estimated uncertainty in the calculation). In addition, the inlet profiles are nearly mixed out by the exit measuring plane (approximately 4 chord lengths downstream of the rotor trailing edge), suggesting that large secondary flows may be present due to the inlet temperature distortion which tends to redistribute the fluid in the stage. A calculation of efficiency vs. percent span location showed a 6% variation in efficiency along the span for the non RTDF case and 35% variation for the RTDF case with efficiencies above 100% (at otherwise the same corrected conditions). The suggestion is not that the numbers just quoted are accurate but that the inlet temperature distortion significantly alters the flowfield in the stage. Ongoing heat transfer measurements for the rotor blades and tip shroud will investigate this.

Future work should investigate the flowfield in more detail in order to separate the contributions to the secondary flows from total pressure gradients and total temperature gradients. In addition, a set of measurements of inlet and exit velocity distribution is necessary to calculate true mass averaged quantities which would allow more realistic comparisons between averaging techniques. Certainly, with the experienced gained from the first set of RTDF tests, the corrected conditions of the turbine can be controlled to a greater extent so that the effects of inlet temperature profiles (axisymmetric or skewed) can be investigated further.

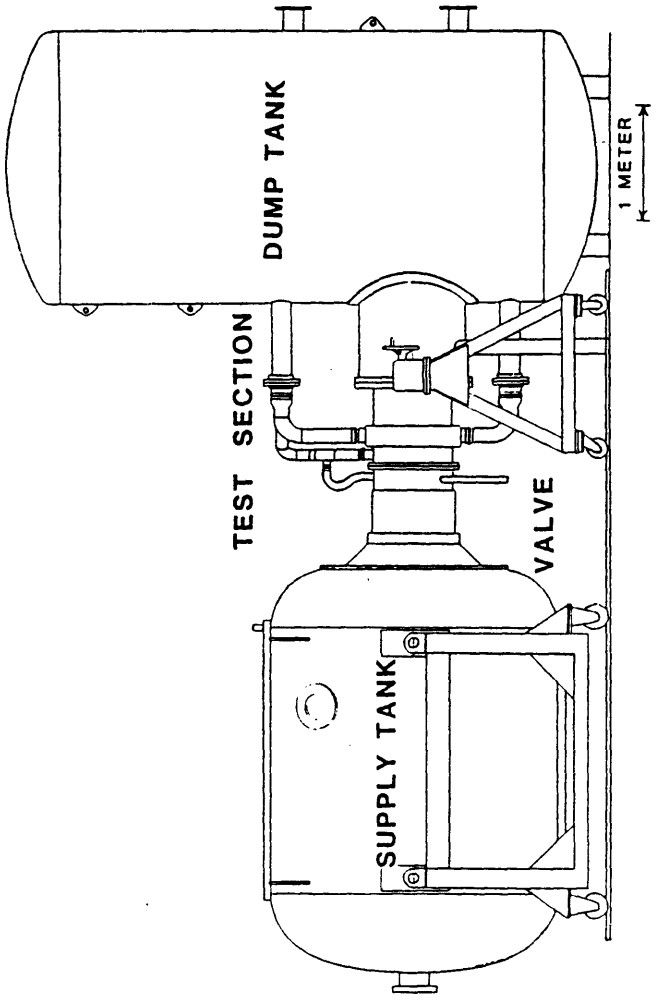

Figure 1.1 – External view of the MIT Blowdown Turbine Facility.

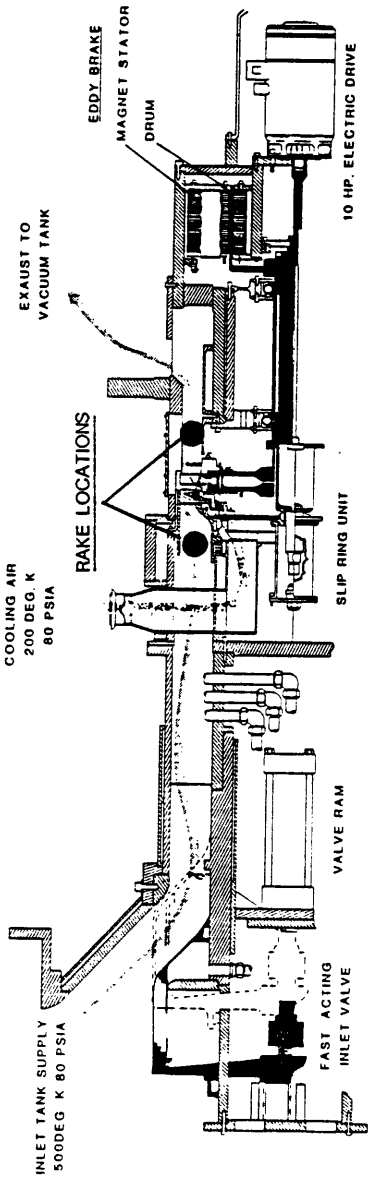

Figure 1.2 - MIT Blowdown Turbine Facility flowpath.

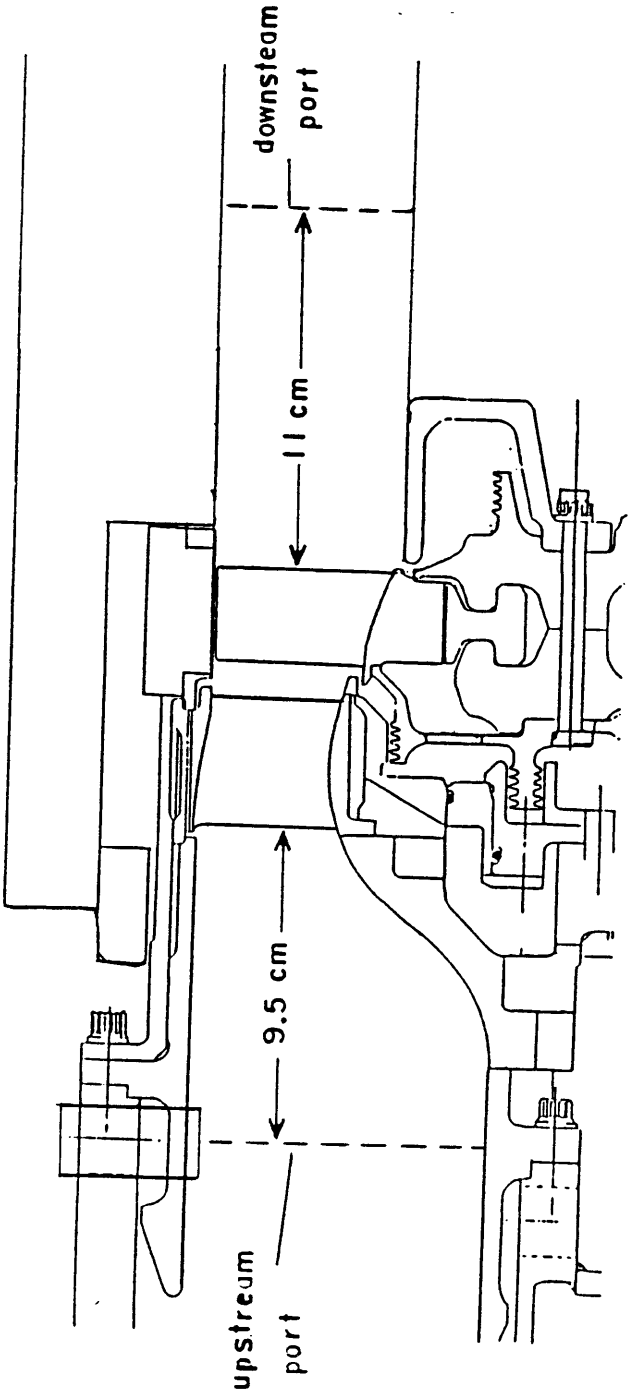

Figure 1.3 – Upstream and downstream measuring stations.

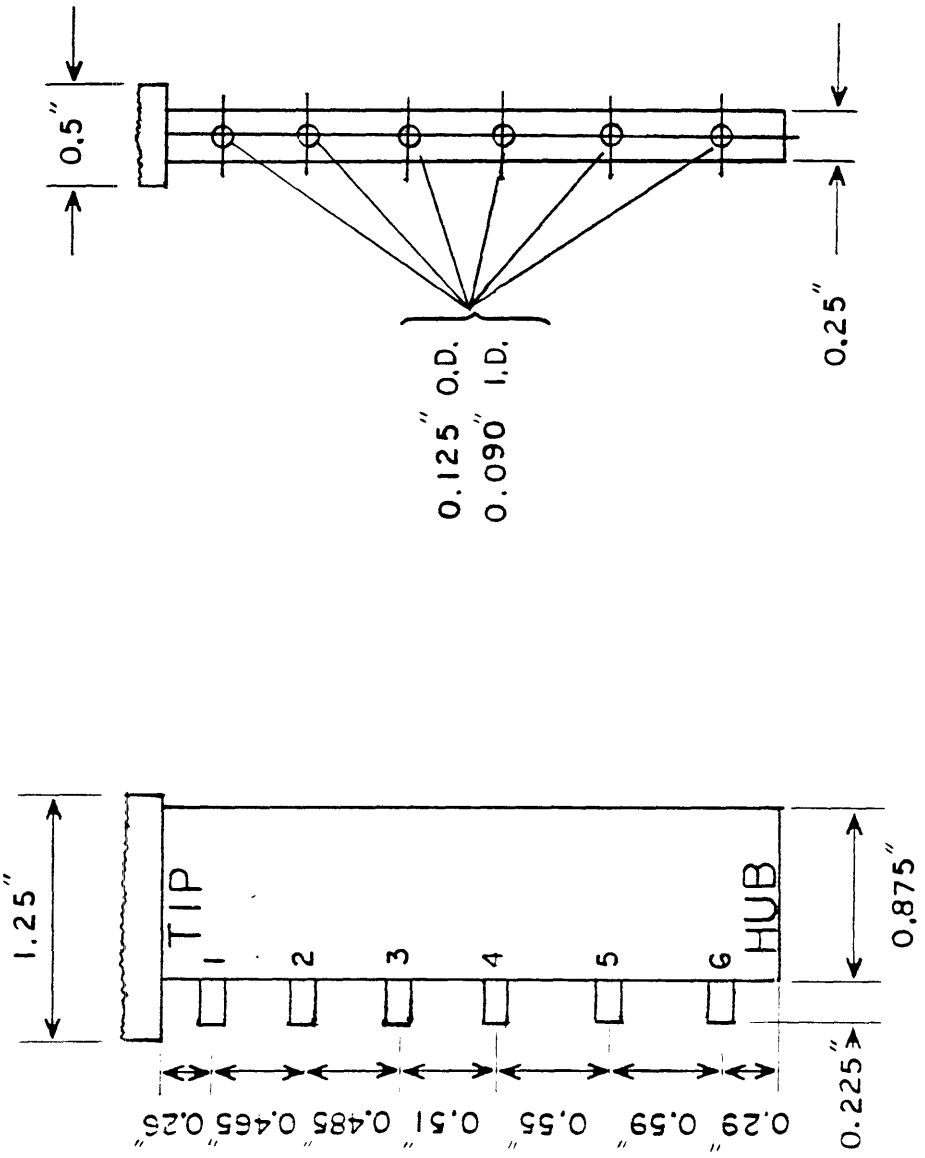

Figure 2.1 - Dimensions of the upstream total pressure probe.

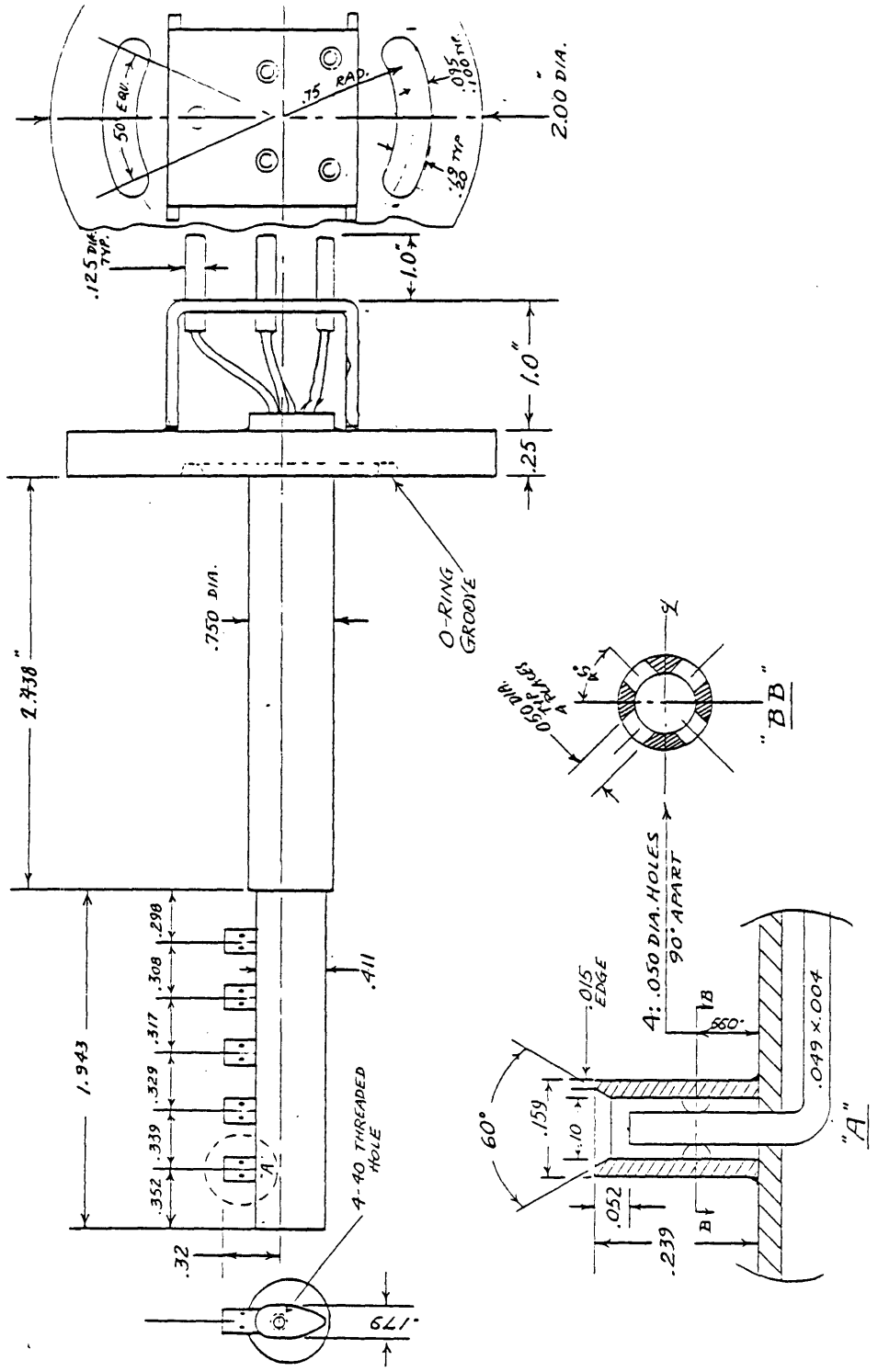

Figure 2.2 - Dimensions of the downstream total pressure probe.

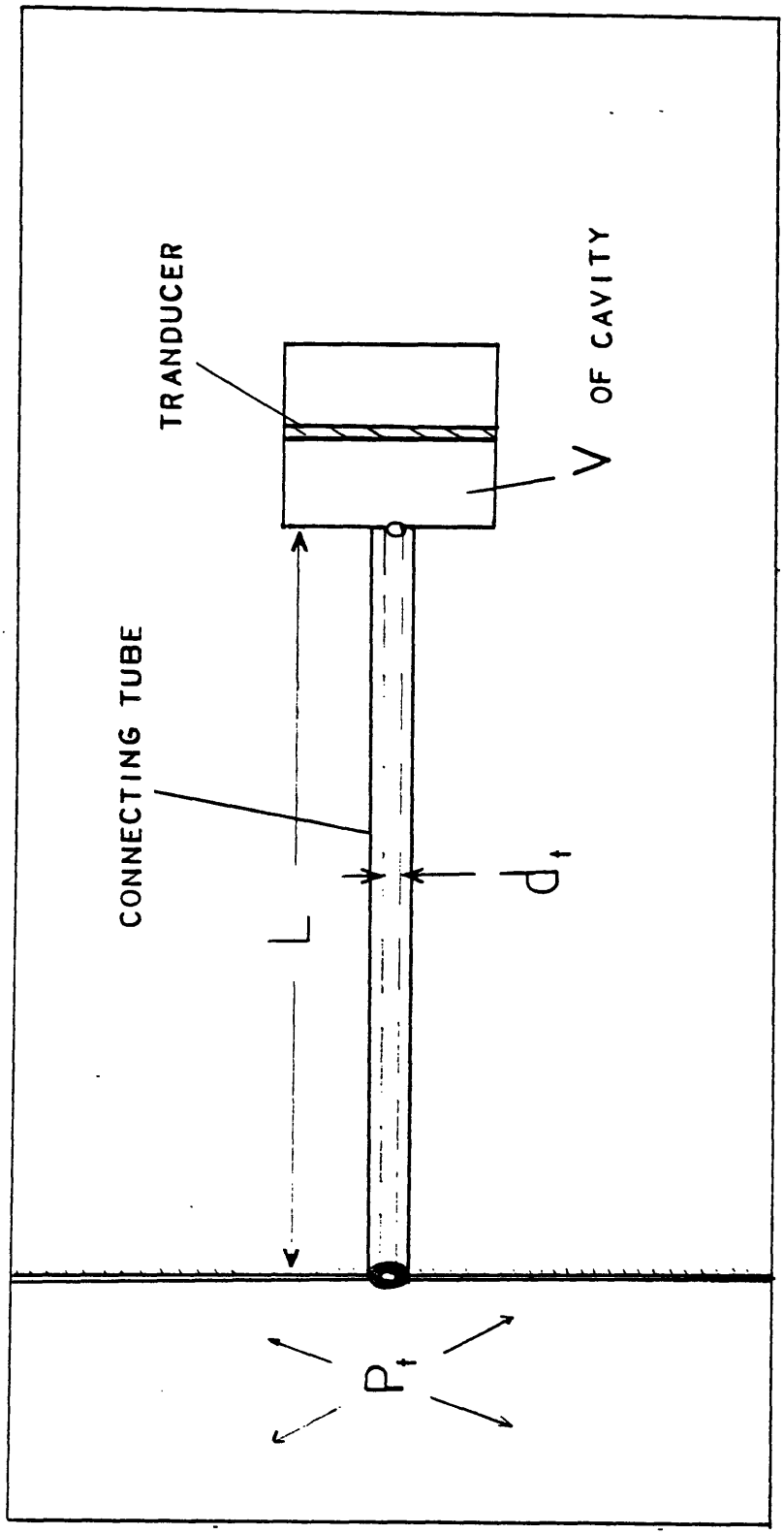

Figure 2.3 - Connecting tube pressure measuring system schematic.

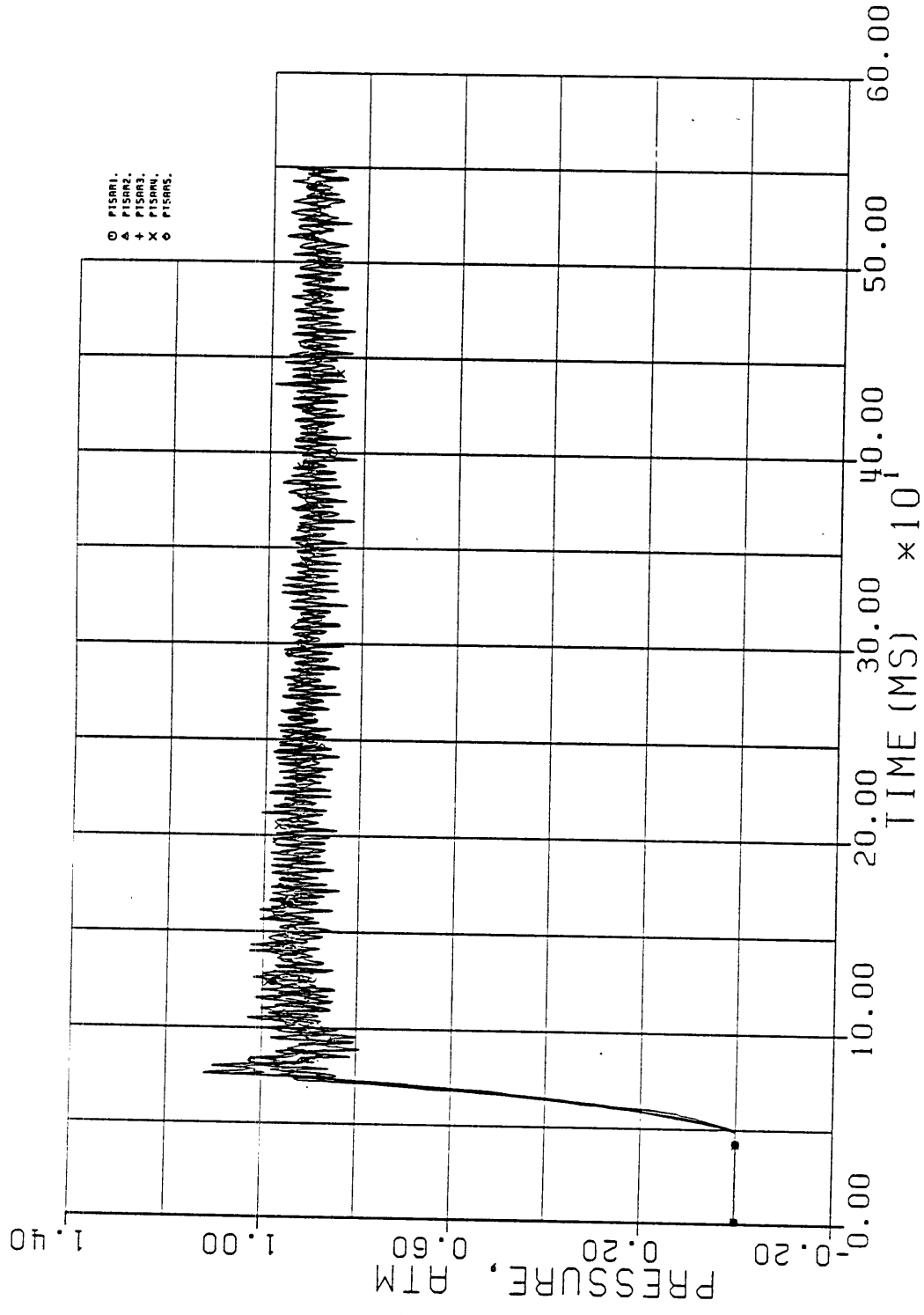

Figure 2.4 - Typical response of the downstream total pressure probe.

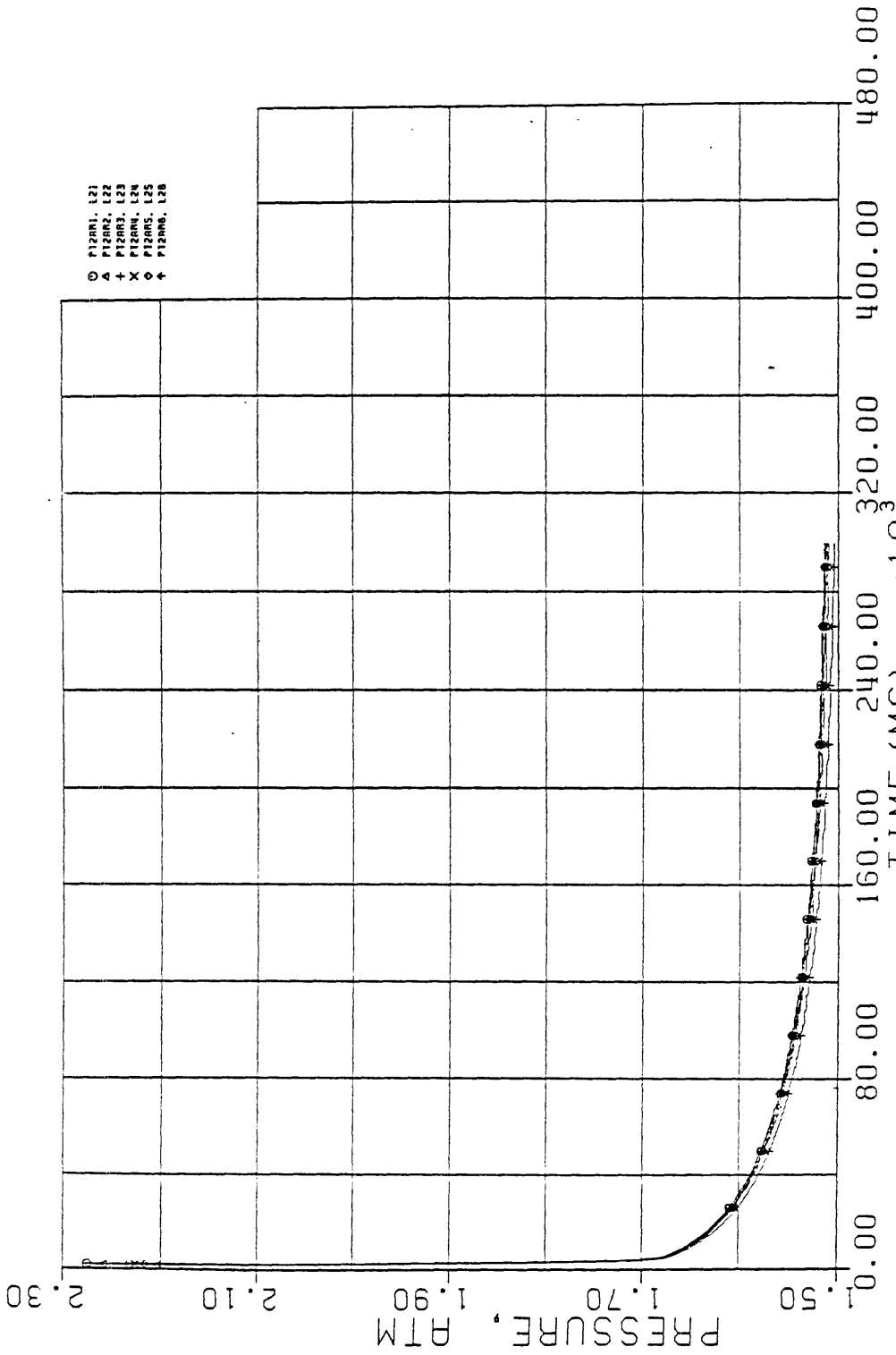

Figure 2.5 - Variations among the upstream rake pressure transducers at the end of the test time (300 sec).

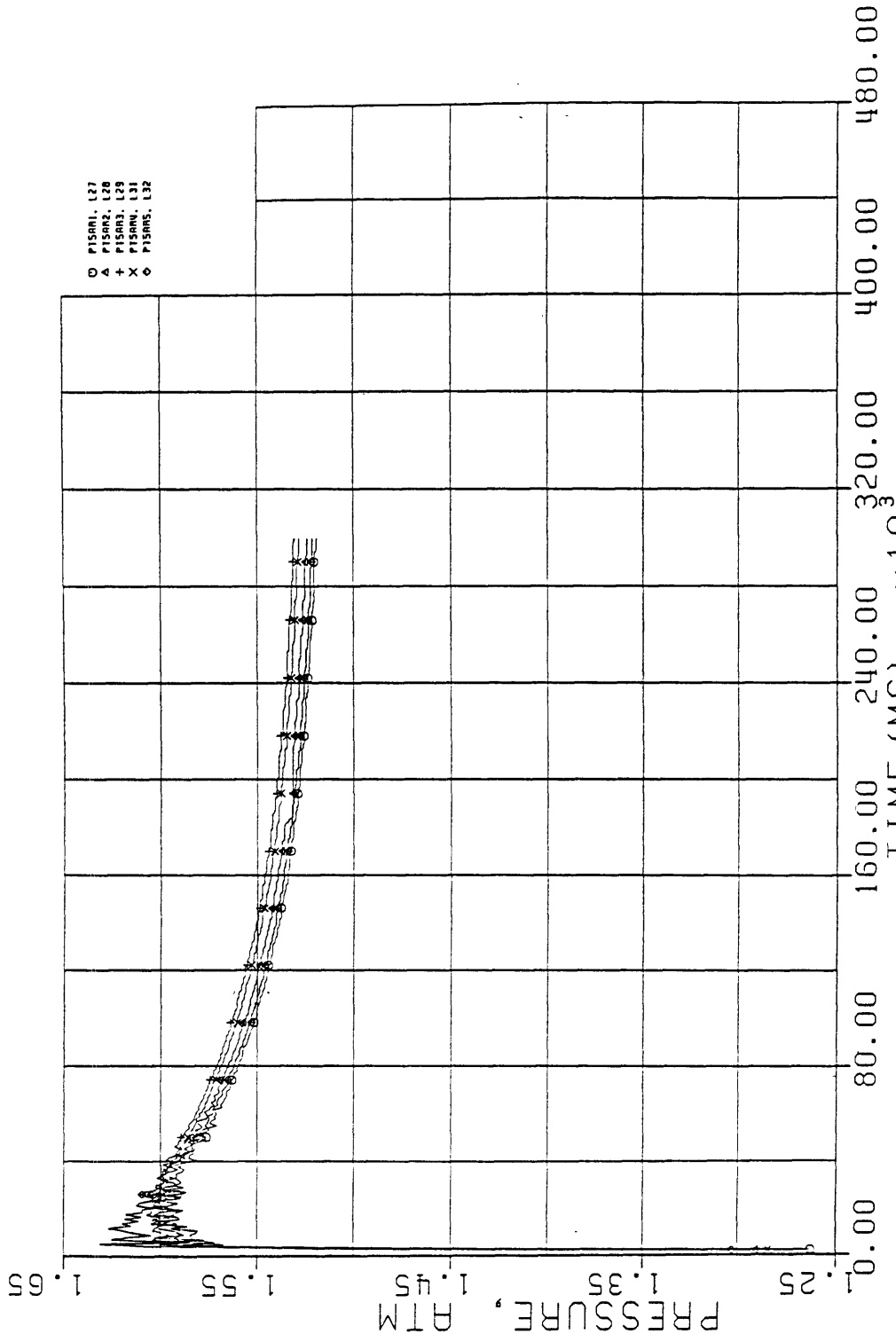

Figure 2.6 - Variations among the downstream rake pressure transducers at the end of the test time (300 sec).

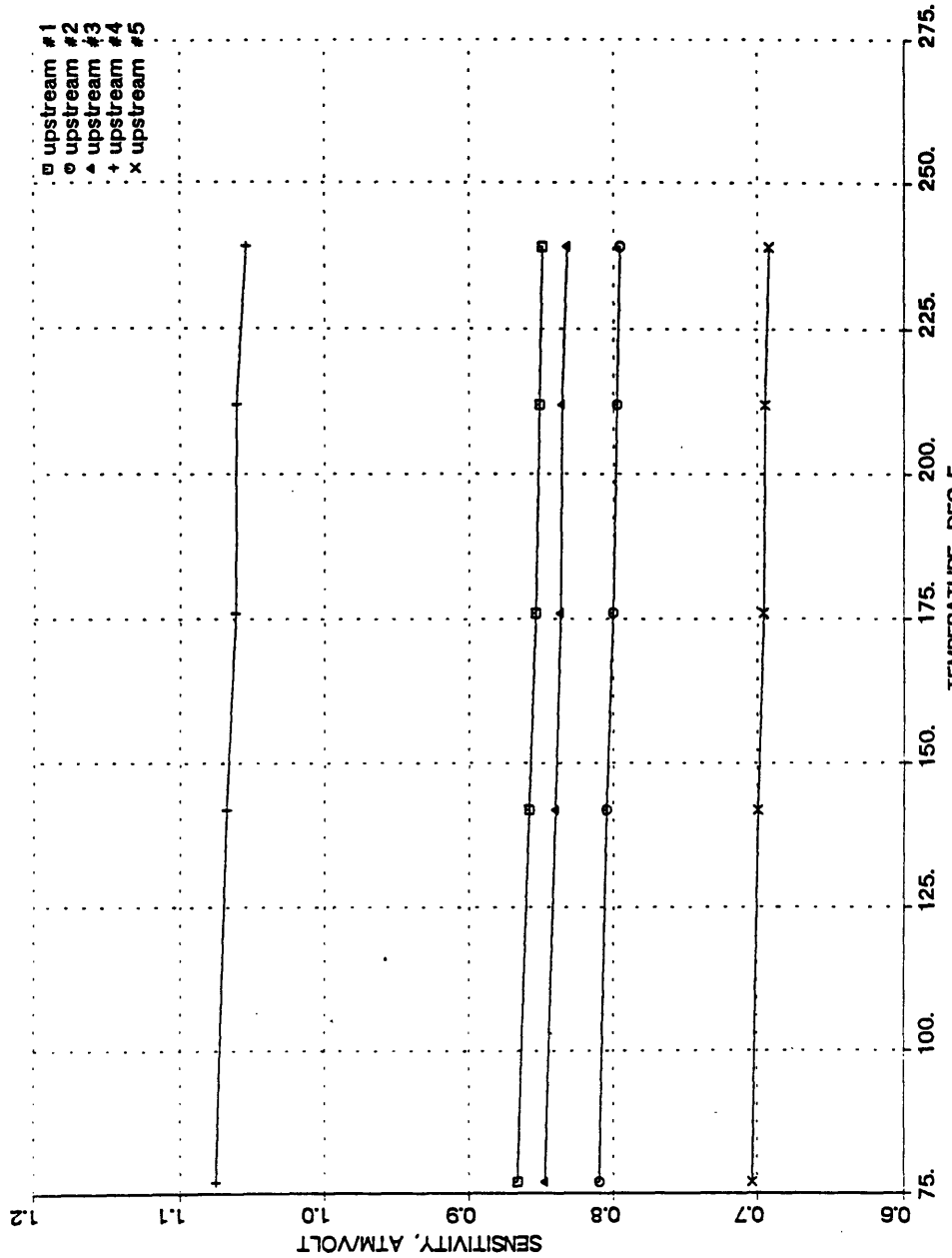

Figure 2.7 - Effect of temperature on the sensitivity of the upstream rake pressure transducers.

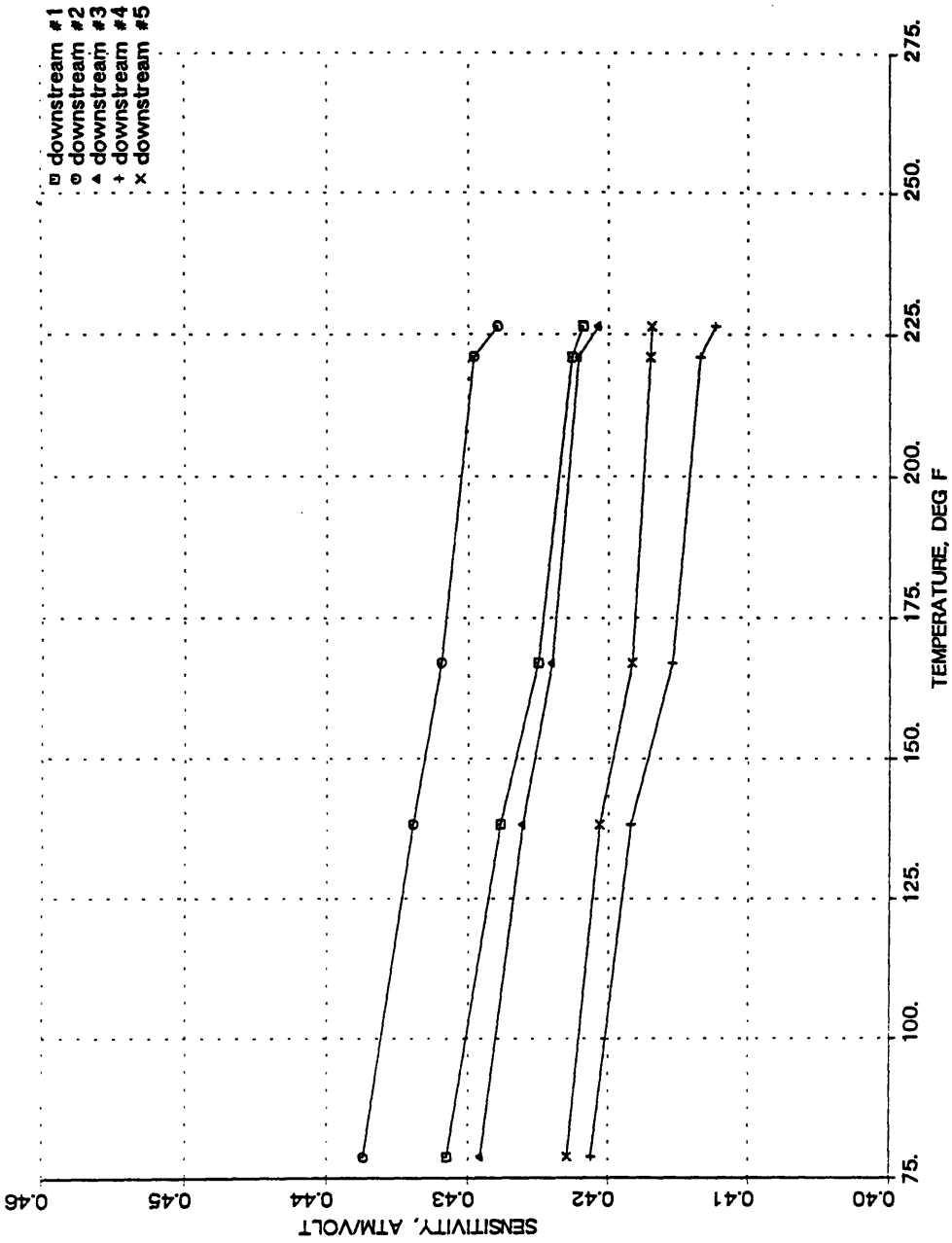

Figure 2.8 - Effect of temperature on the sensitivity of the downstream rake pressure transducers.

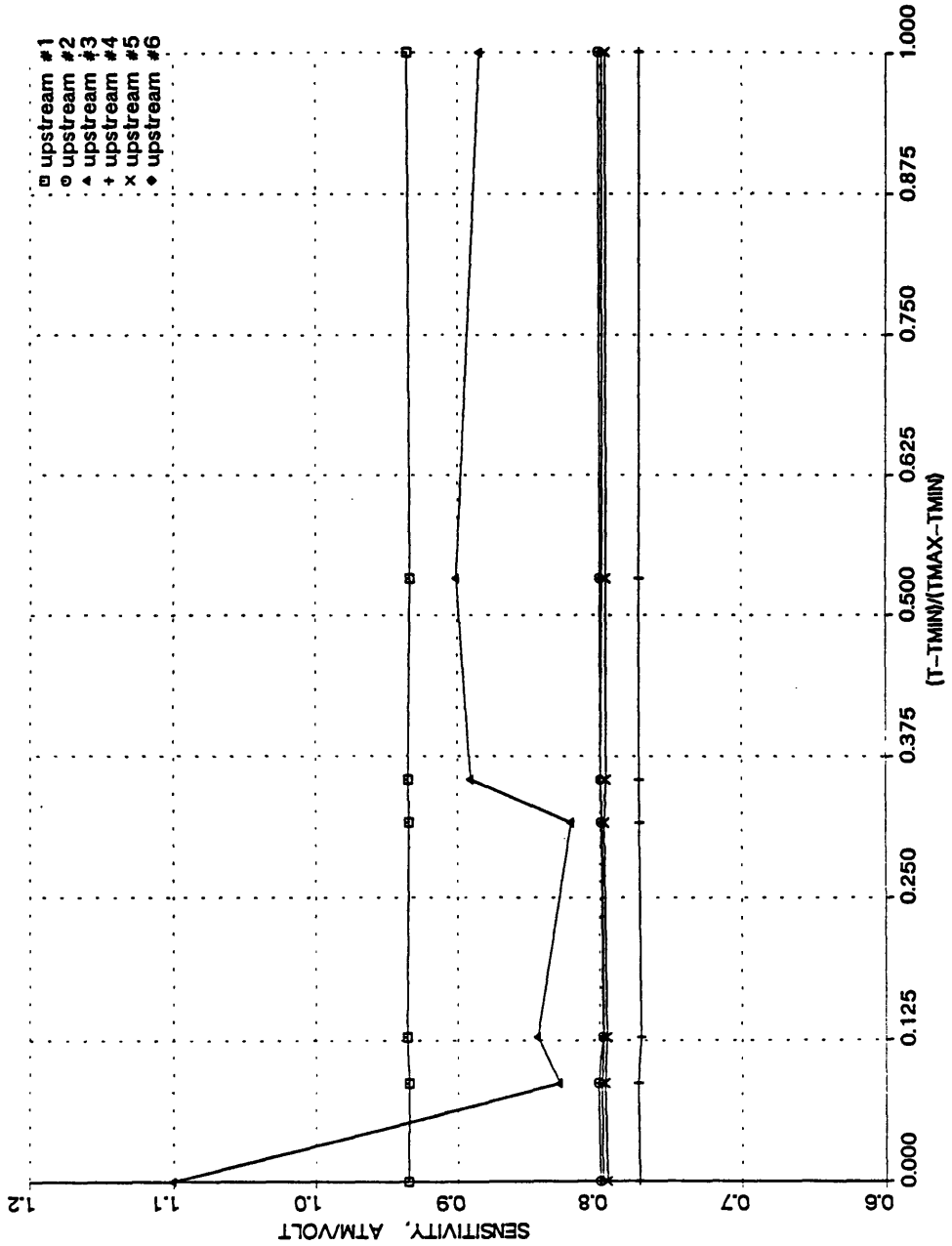

Figure 2.9 - Upstream rake pressure transducer Sensitivities vs. nondimesnional inlet temperatures.

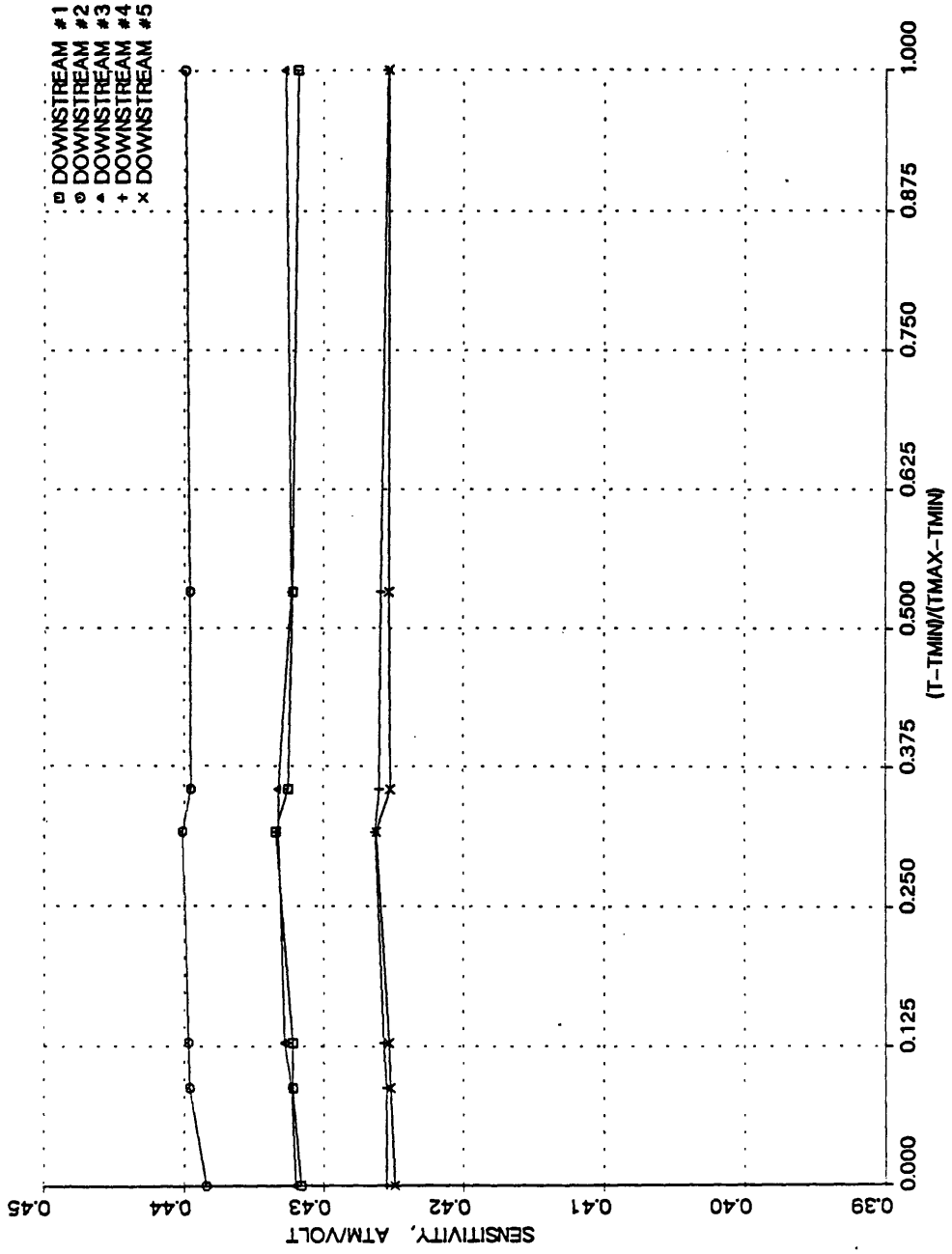

Figure 2.10 - Downstream rake pressure transducer Sensitivities vs. nondimesnional inlet temperatures.

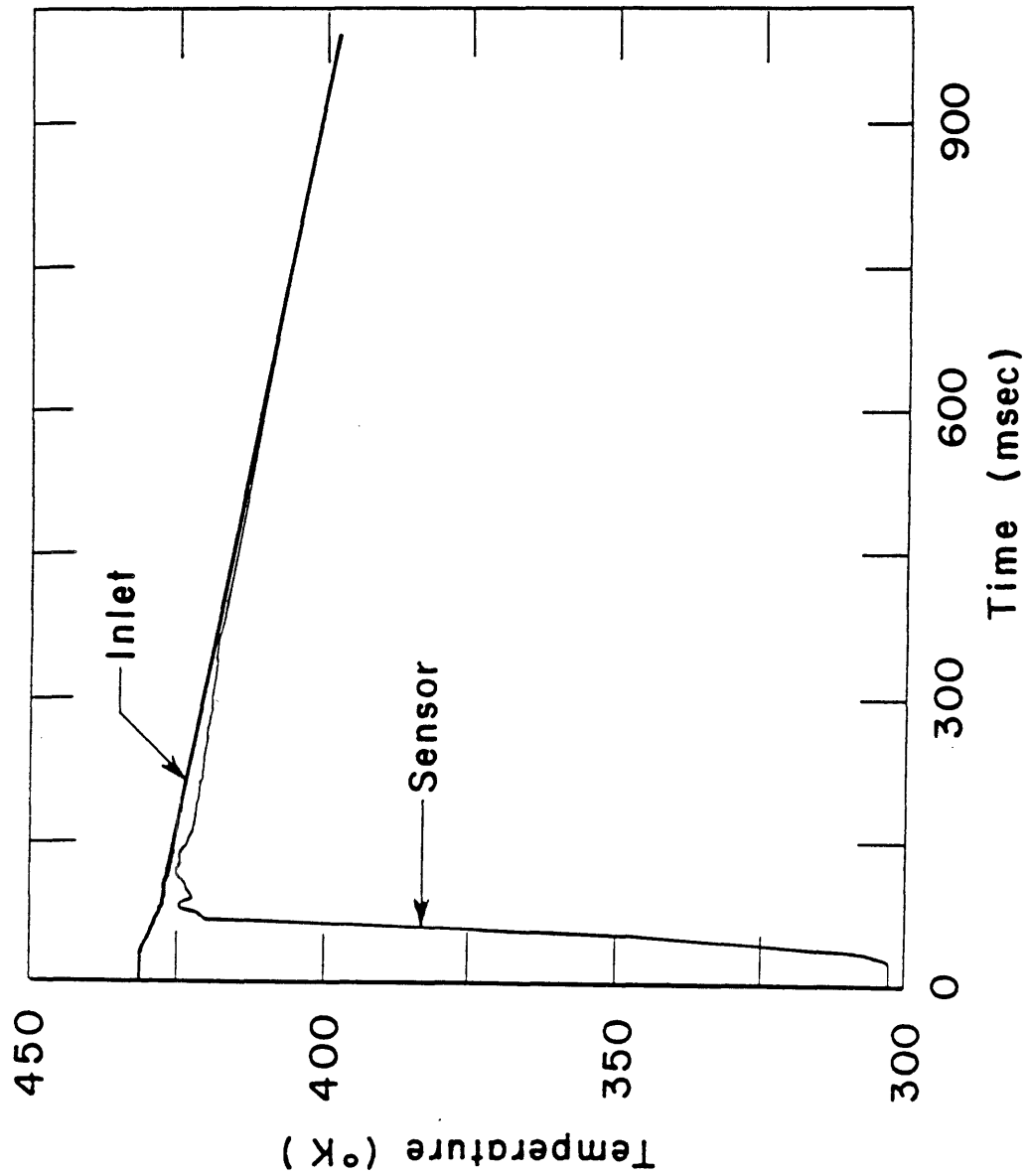

Figure 3.1 – Typical time history of the supply tank temperature ("inlet") and sensor response ("sensor") for a blowdown test.

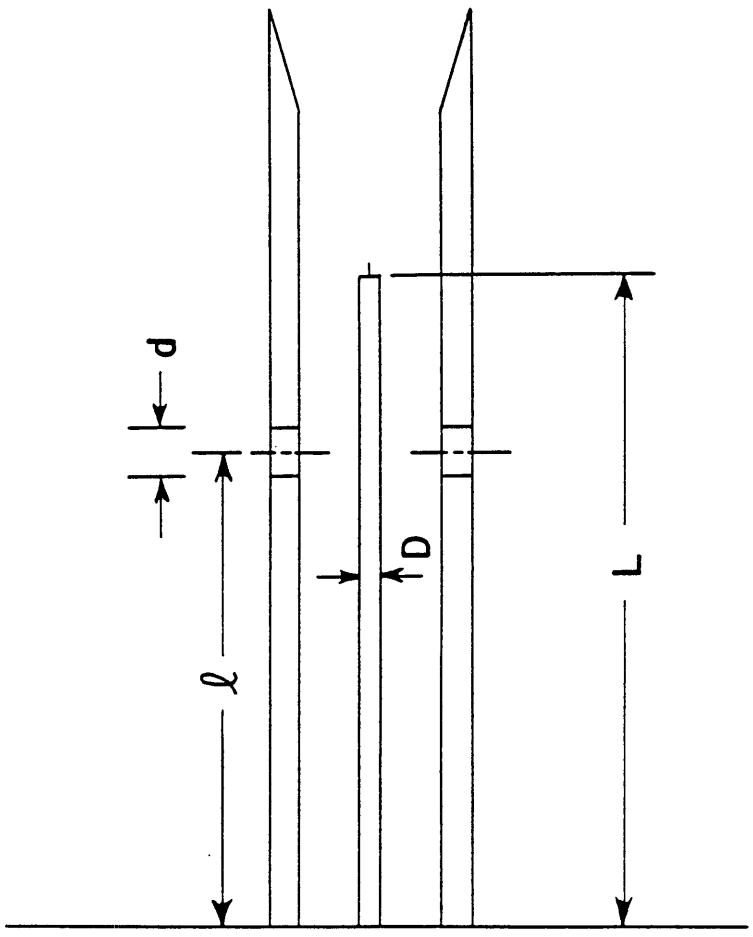

Figure 3.2 - Generic probe head design variables. The vaiables are support length L, support diameter D, bleed hole diameter d, and the axial distance l from the probe body to the bleed hole.

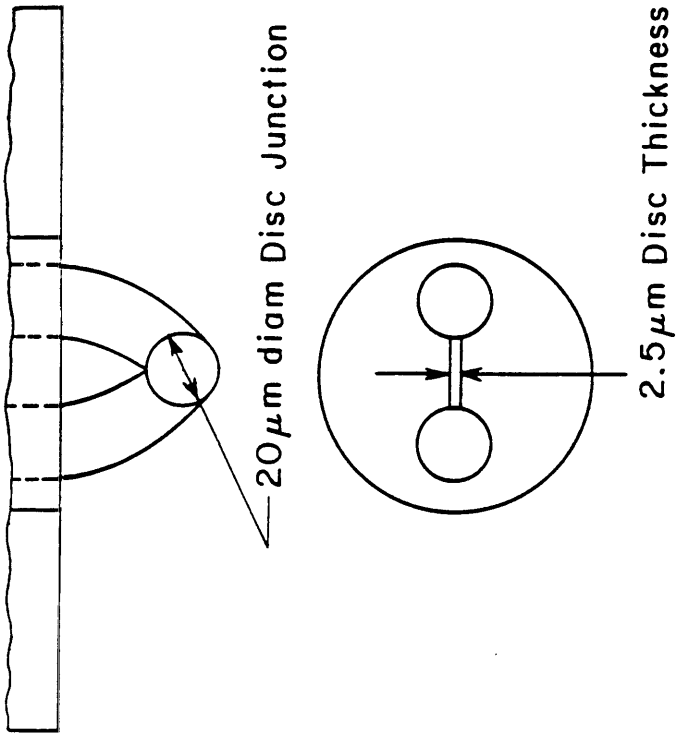

Figure 3.3 - Thermocouple (type K) dimensions.

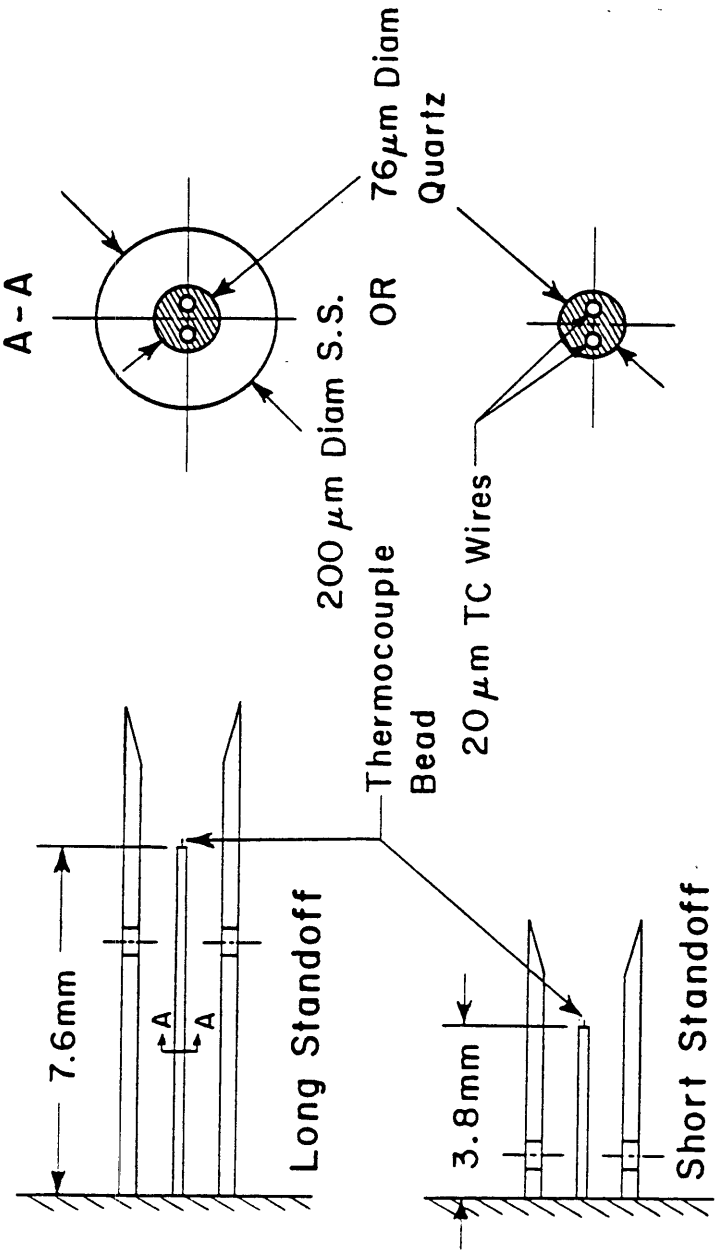

Figure 3.4 - Four different probe head designs. The short and long standoffs were combined with both kinds of support (quartz and quartz with stainless steel sheath).

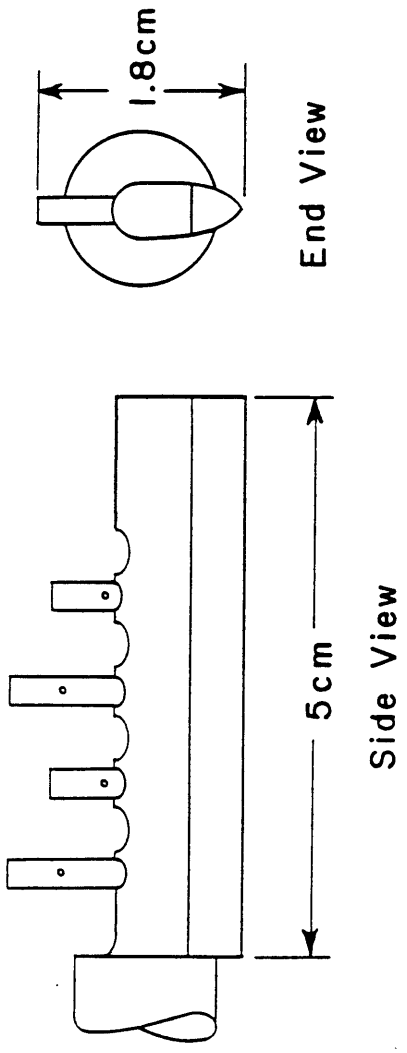

Figure 3.5 - Prototype probe with the four different head designs.

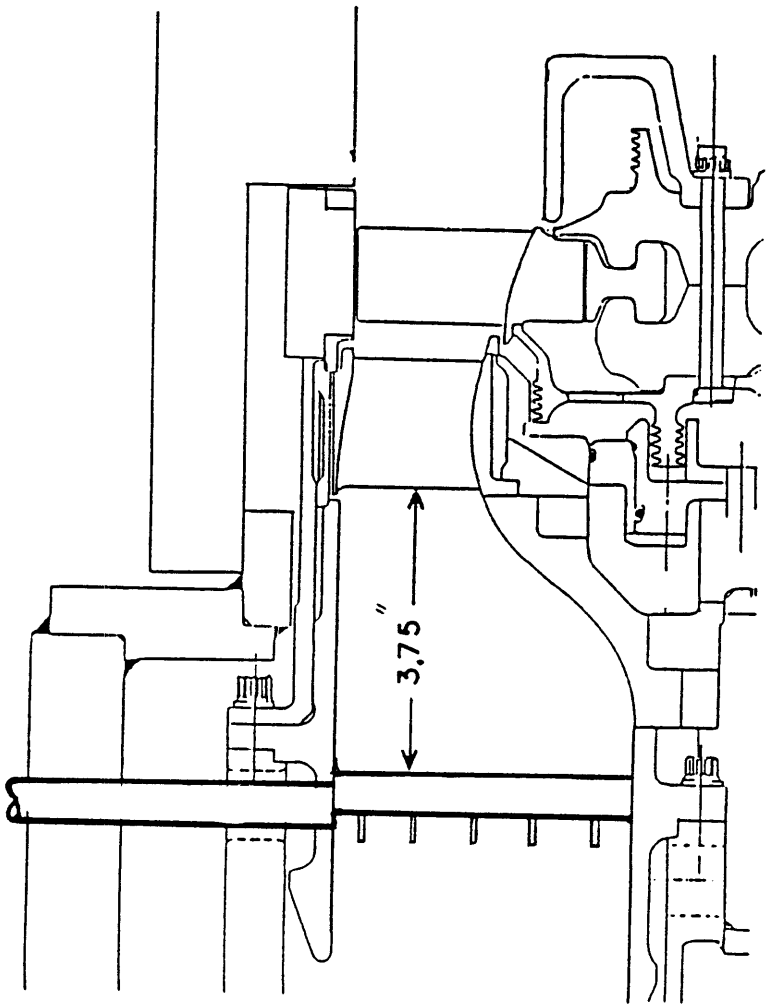

Figure 3.6 - The upstream rake is placed 3.75" (9.5 cm) from the NGV leading edge.

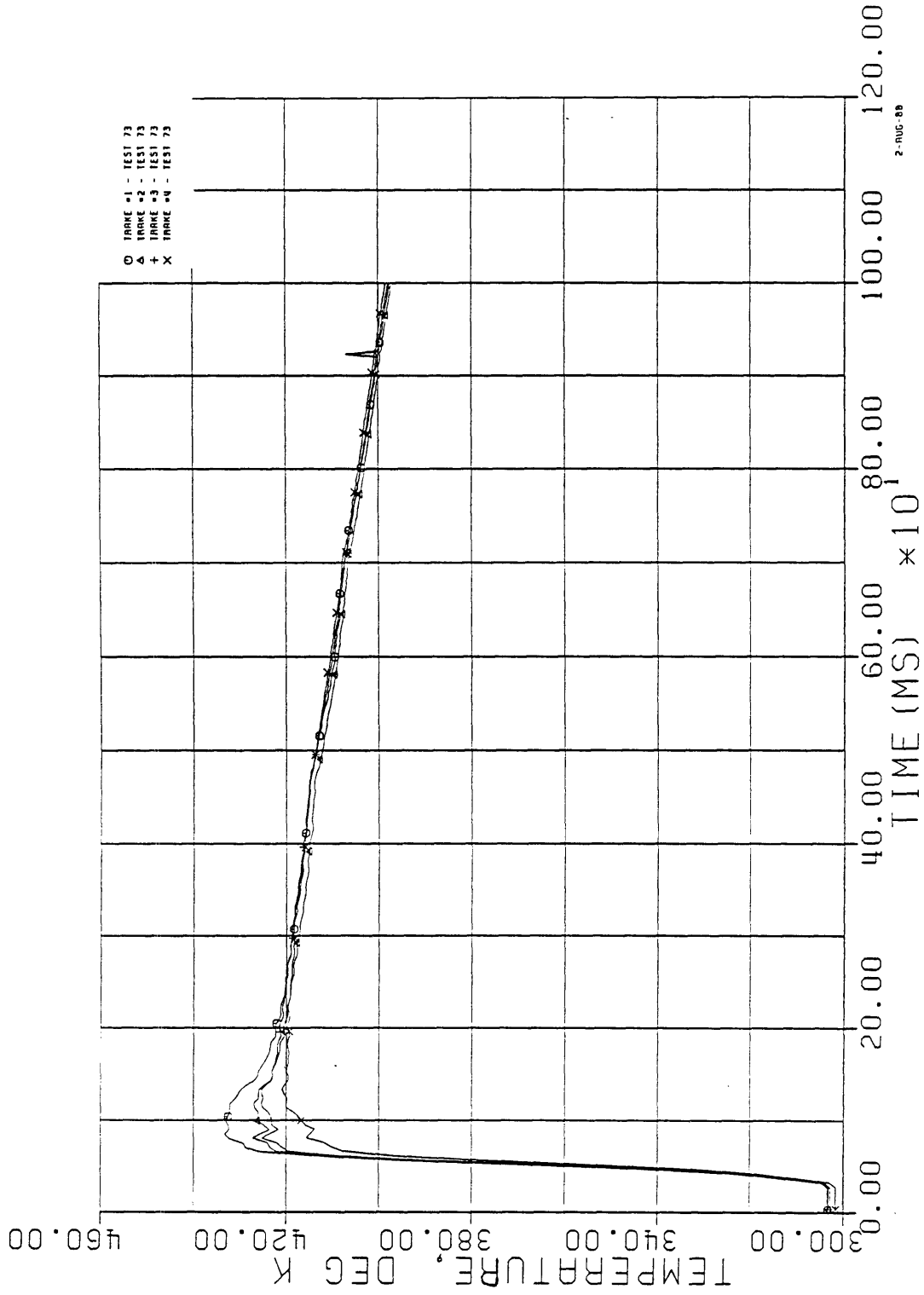

Figure 3.7 - Response of the prototype probe for TEST73.

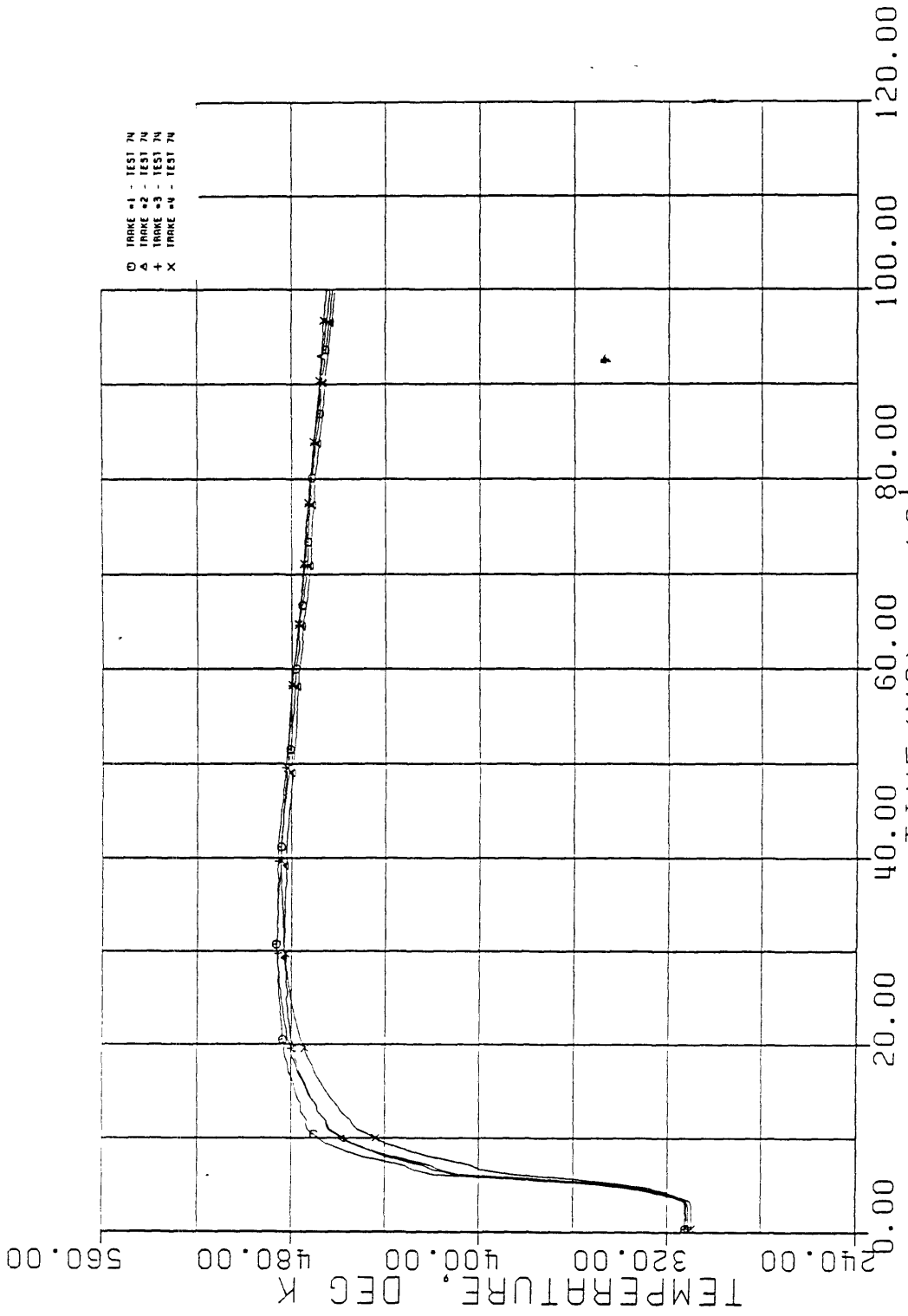

Figure 3.8 - Response of the prototype probe for TEST74.

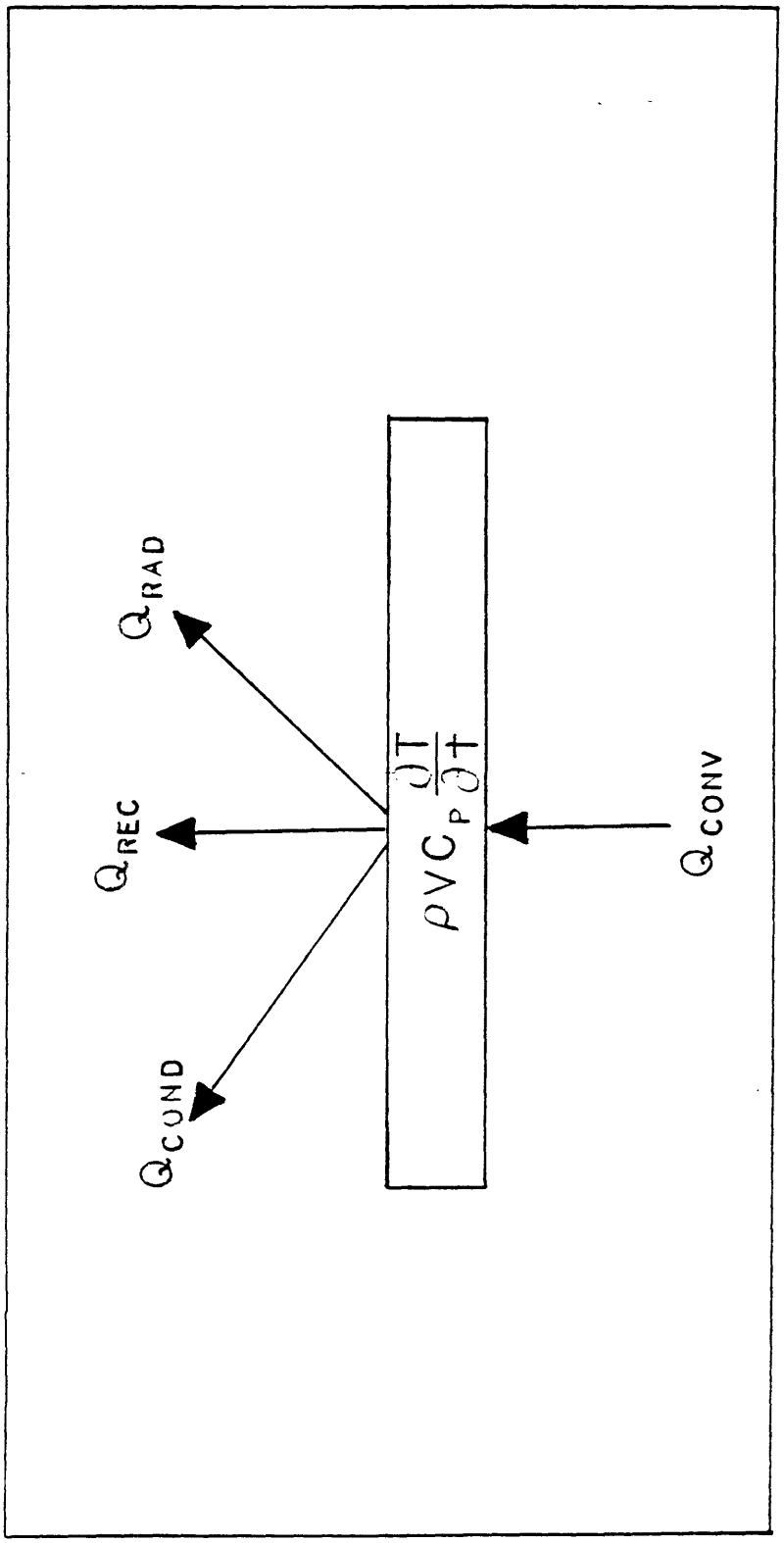

Figure 3.9 - Thermocouple junction energy balance.

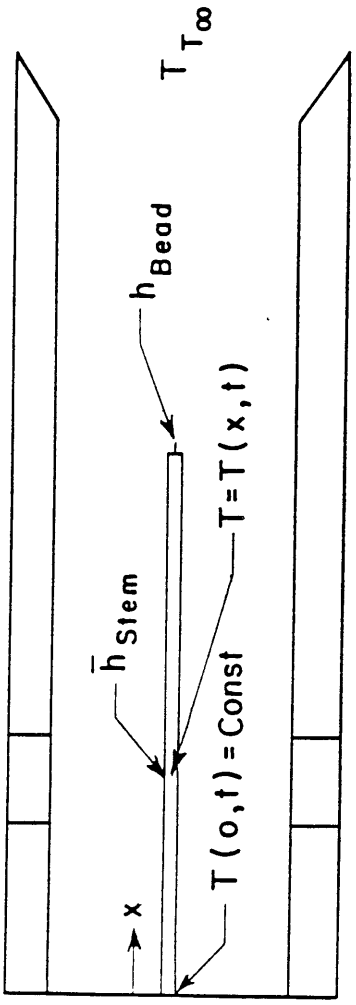

Figure 3.10 - Transient conduction model for the junction support.

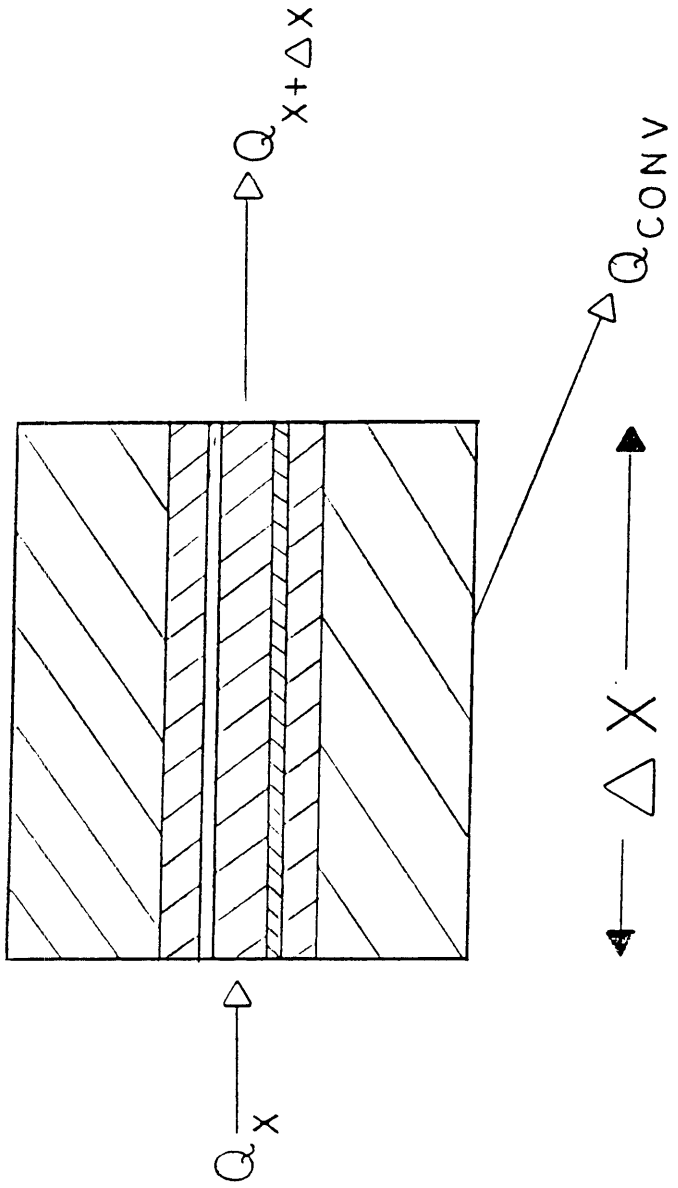

Figure 3.11 - Thermocouple junction support energy balance.

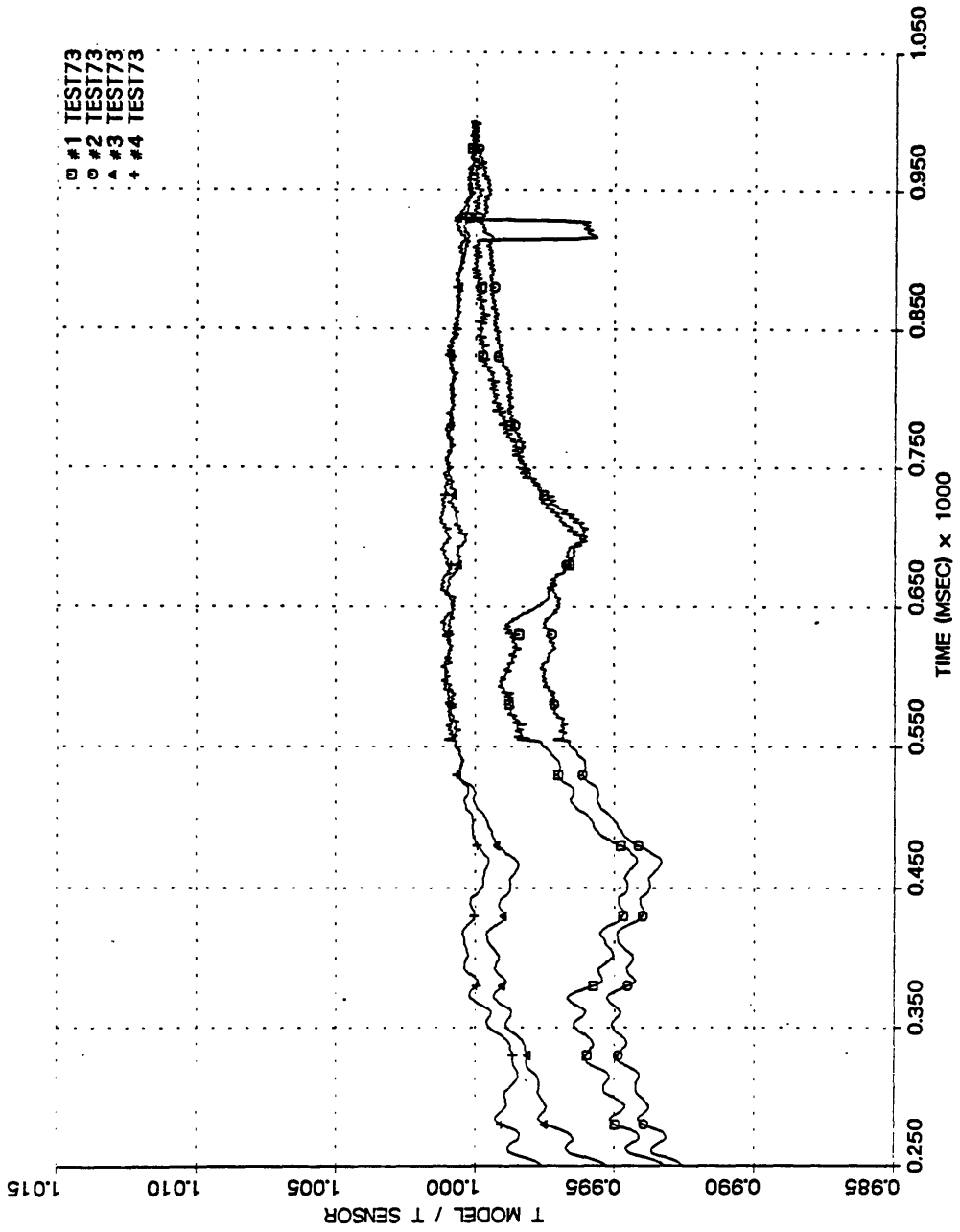

Figure 3.12 - Ratio of the temperature predicted by the model to the temperature indicated by the sensor for TEST73.

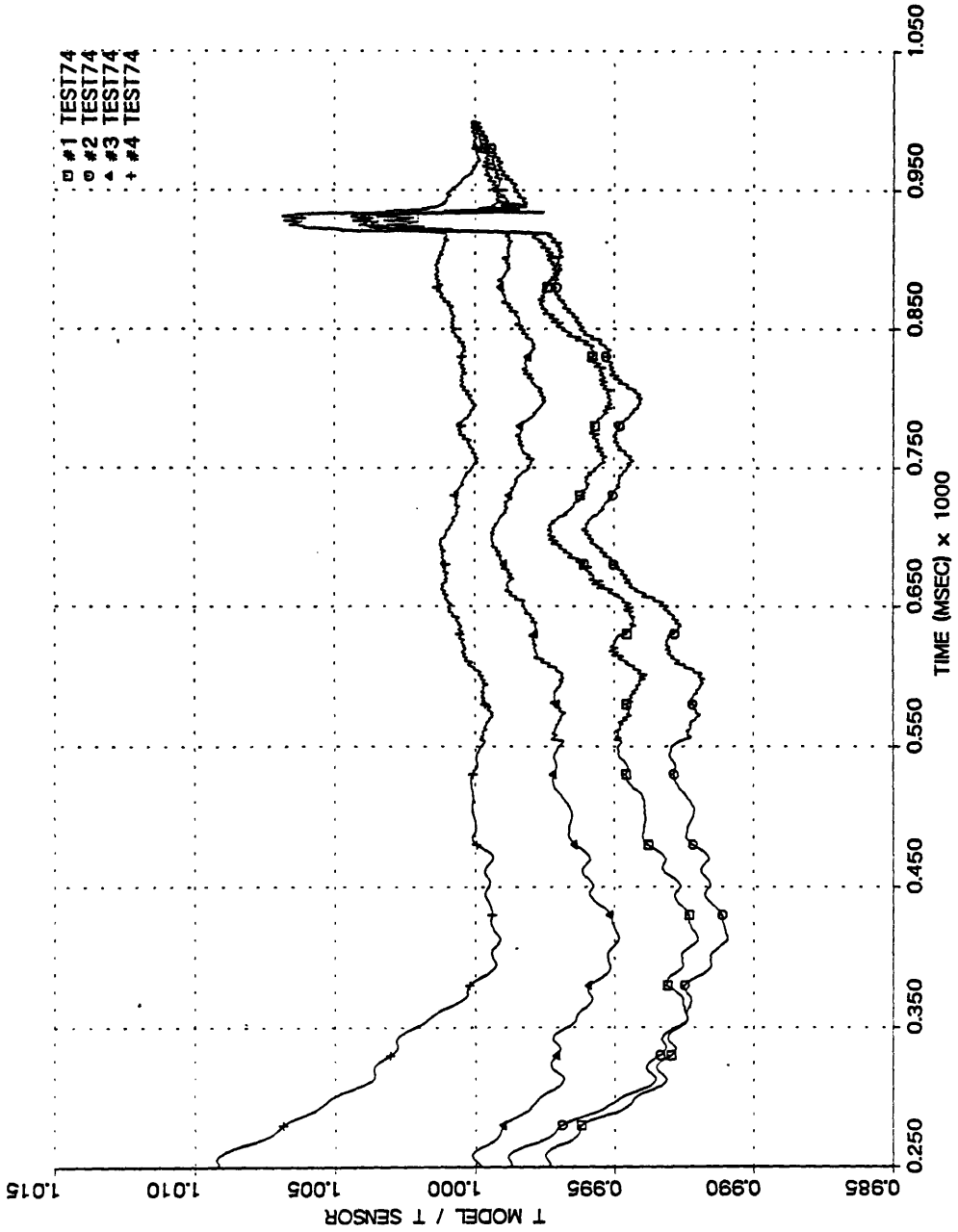

Figure 3.13 - Ratio of the temperature predicted by the model to the temperature indicated by the sensor for TEST74.

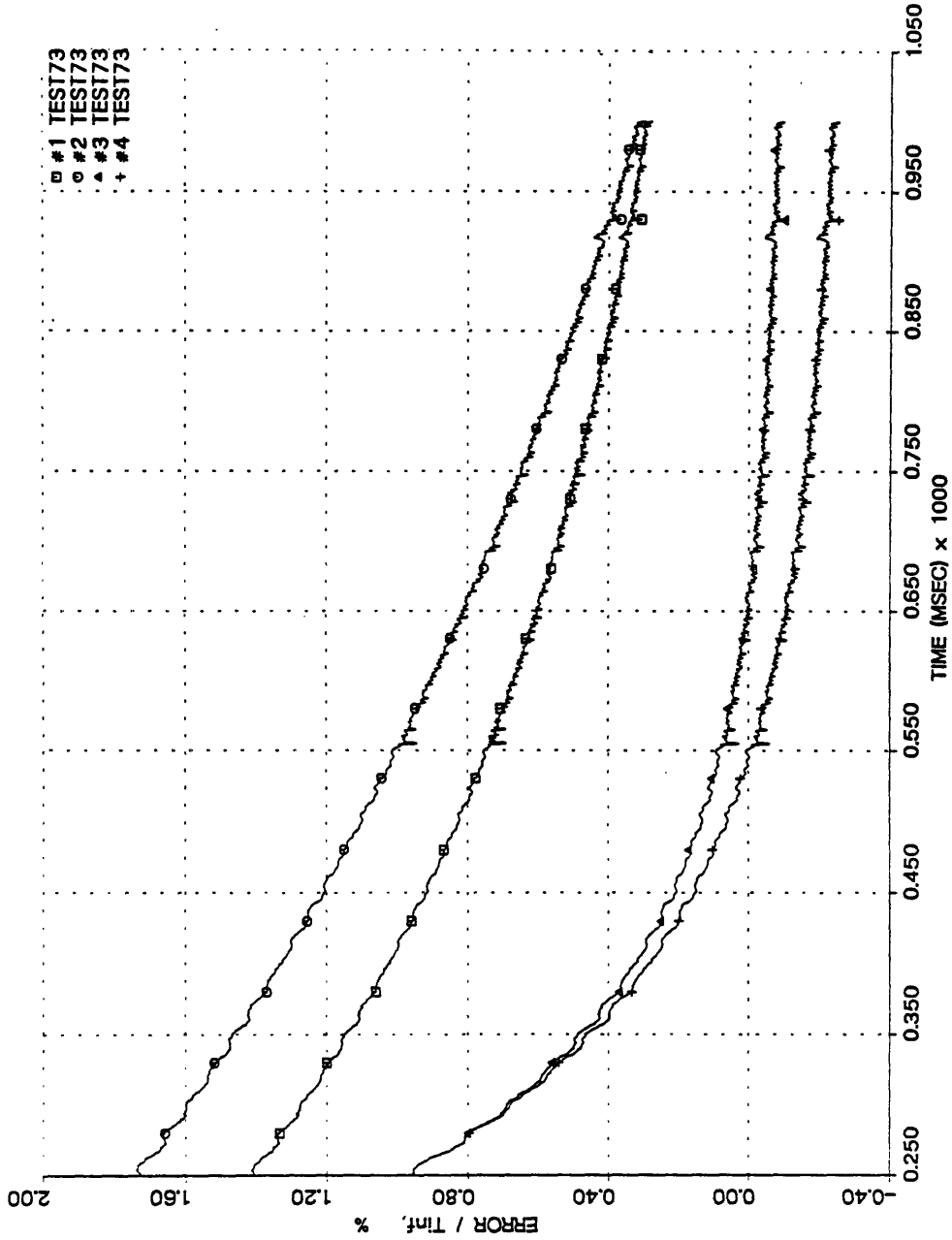

Figure 3.14 - Nondimensional error for TEST73. Error/Tinf is less than 0.2% beyond 450 msec for the quartz only designs.

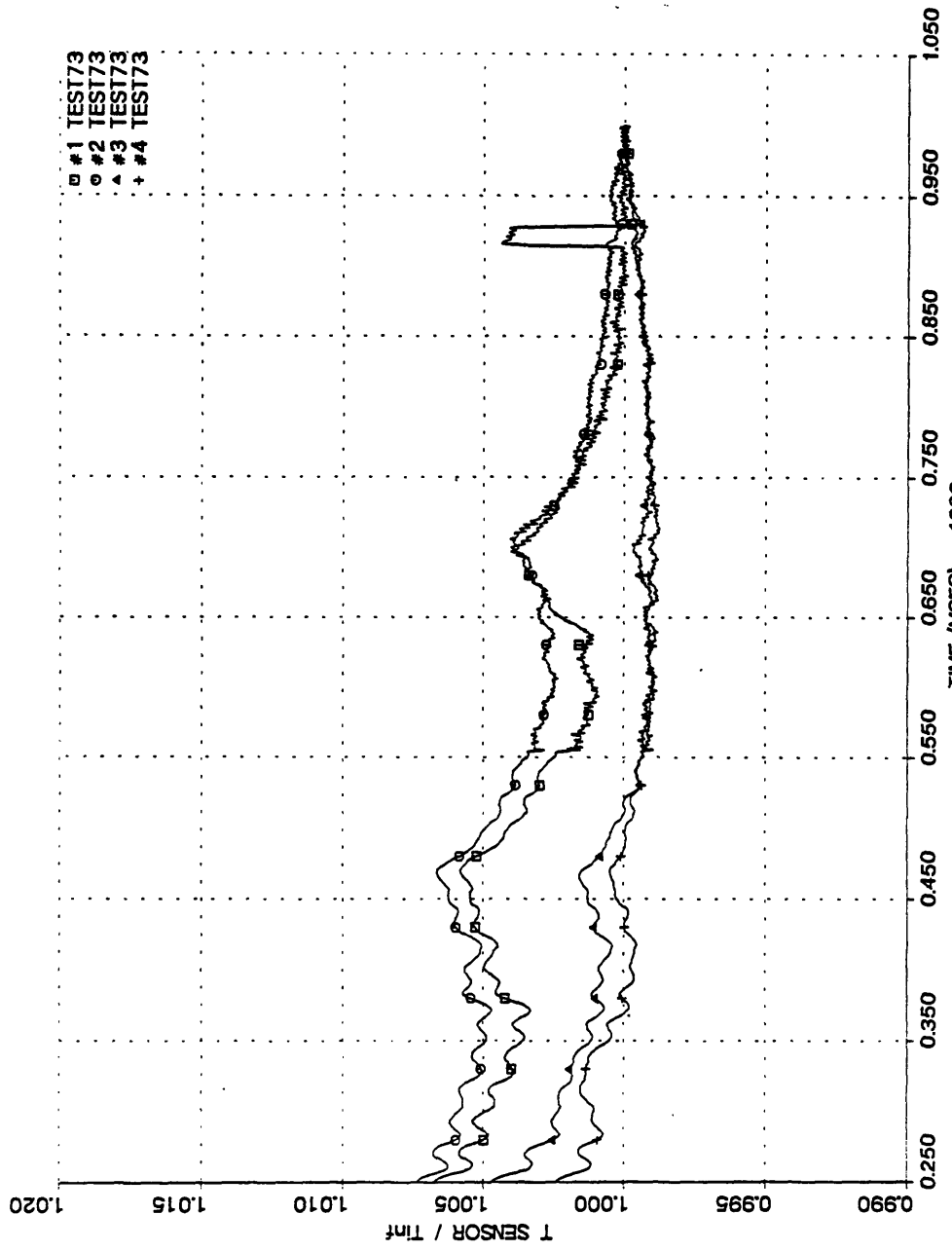

Figure 3.15 – Corrected sensor temperature / T_{inf} for TEST73. The corrected temperatures are the same as T_{inf} to within 0.1% beyond 450 msec for the quartz only designs.

The Libraries
Massachusetts Institute of Technology
Cambridge, Massachusetts 02139

Institute Archives and Special Collections
Room 14N-118
(617) 253-5688

There is no text material missing here.
Pages have been incorrectly numbered.

PAGE 119

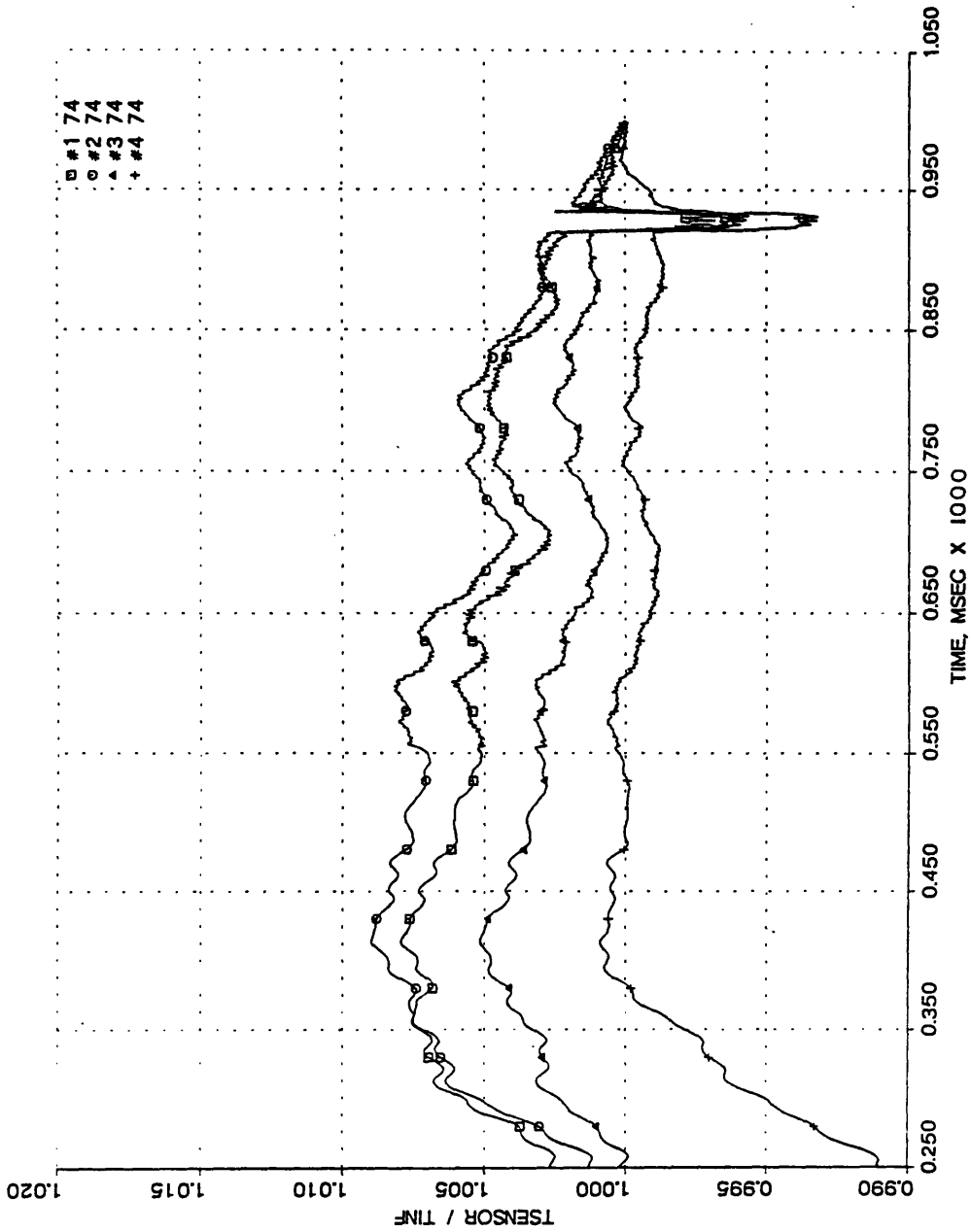

Figure 3.16 - Corrected sensor temperature / T_{inf} for TURB74. The corrected temperatures deviate more from T_{inf} due to the higher nonuniformities in the initial gas temperature.

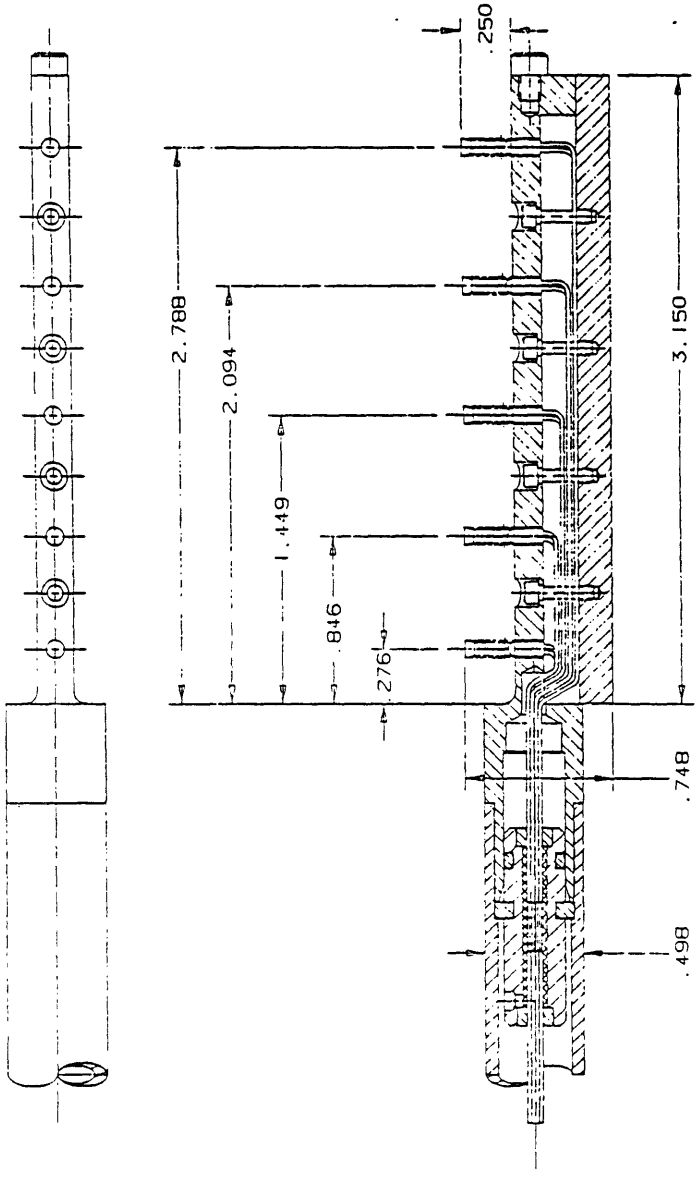

Figure 3.17 - Final upstream total temperature probe dimensions.

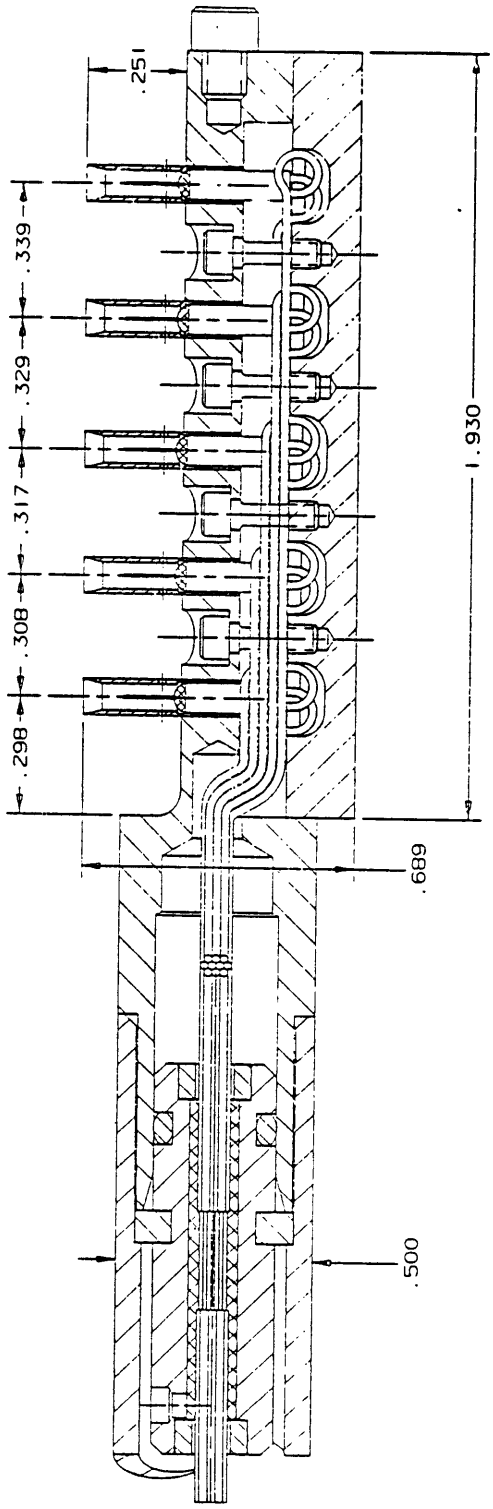

Figure 3.18 - Final downstream total temperature probe dimensions.

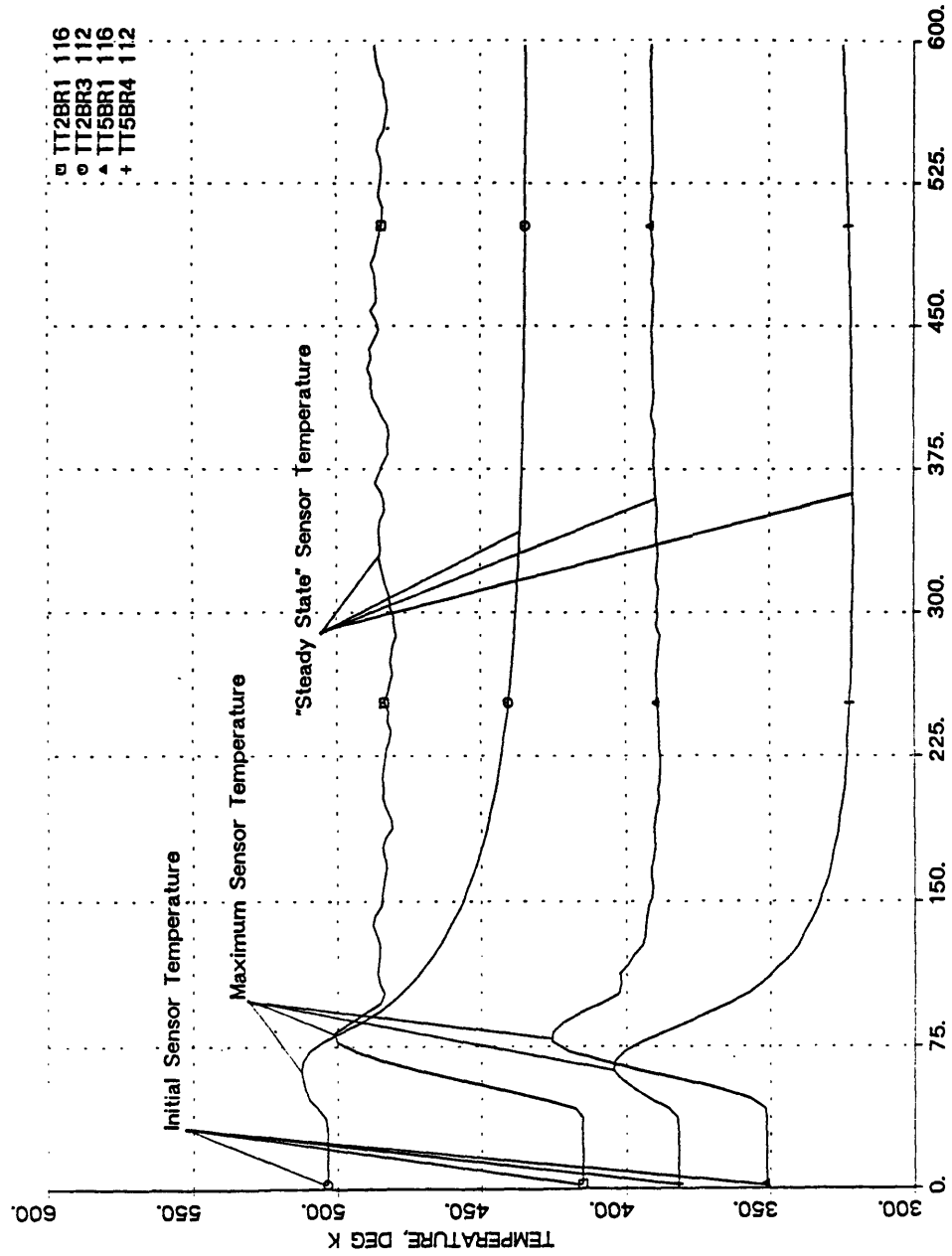

Figure 3.19 - Four maximum error cases for the RTDF tests. The time traces of the four cases where the initial temperature deviated most from the steady state temperatures are shown. Note the temperature "impulse".

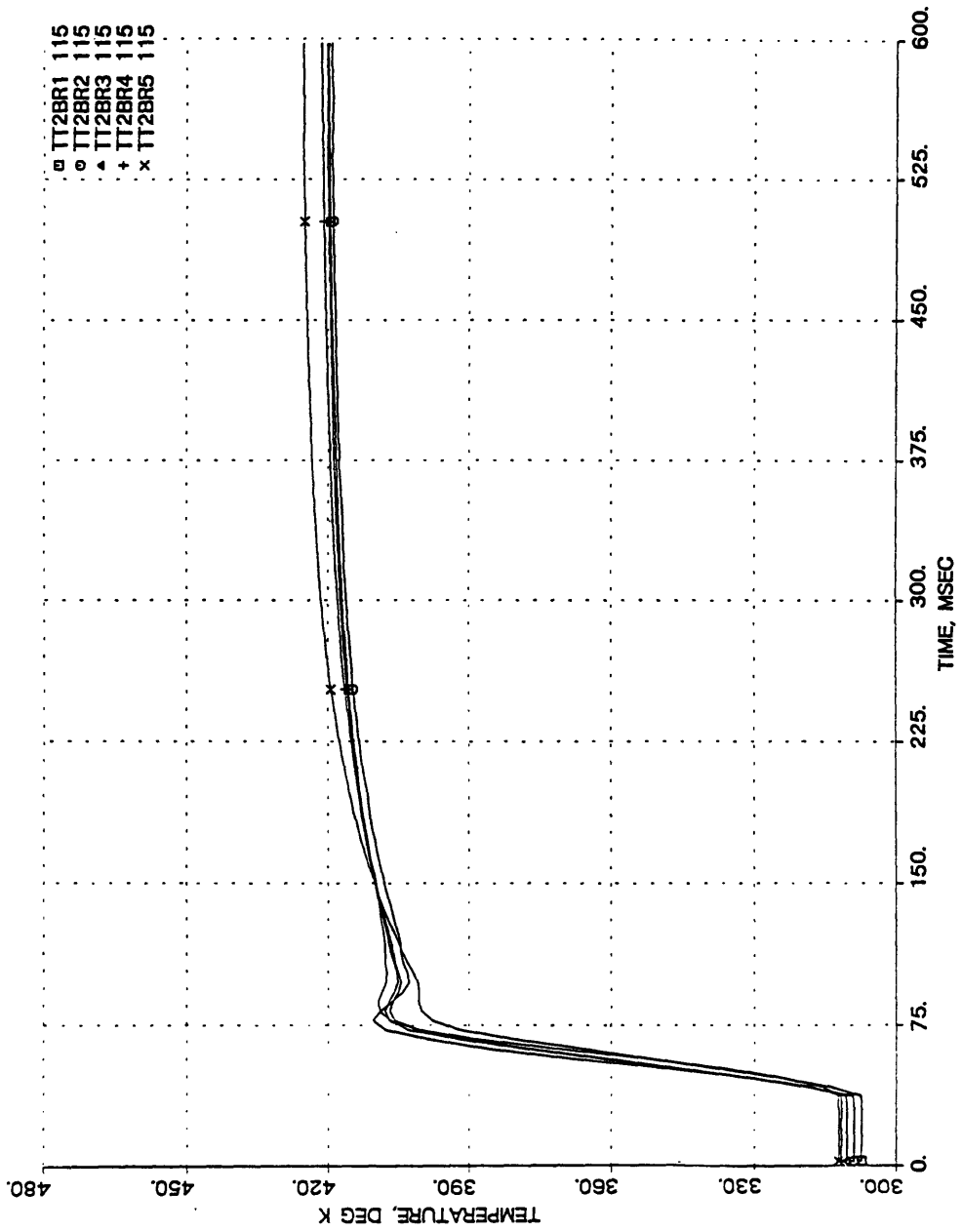

Figure 3.20 - Unheated Probe response for TEST115. The temperature impulse is barely seen for the unheated rake.

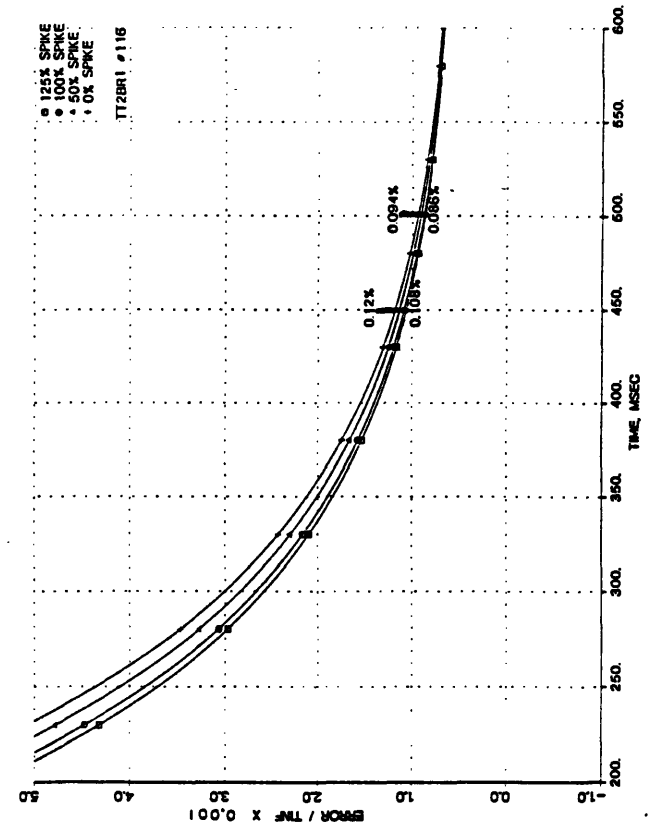

B

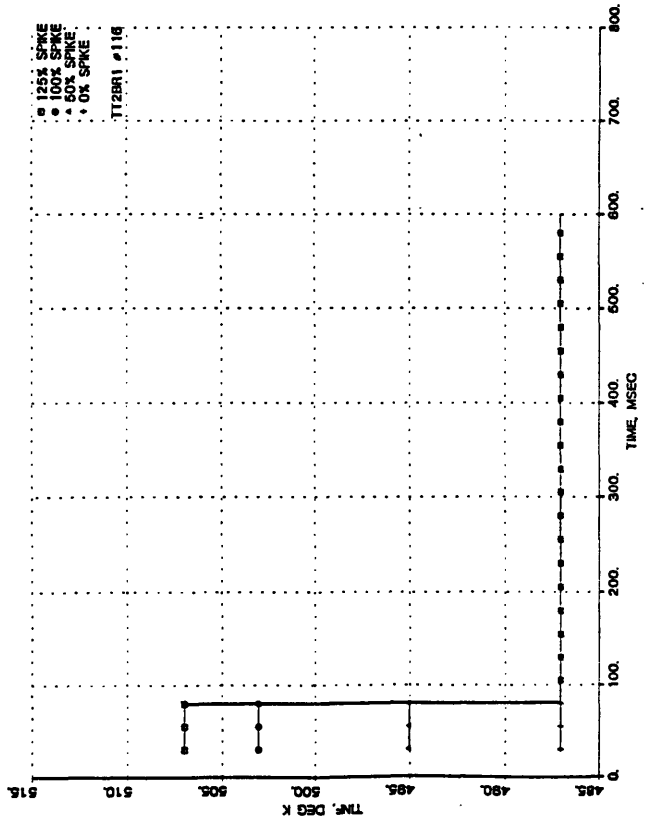

A

Figure 3.21 - Inputs (a) and responses (b) predicted by the temperature probe model for upstream sensor #1 (TEST116) show negligible difference between the max impulses and no impulse at 500 msec.

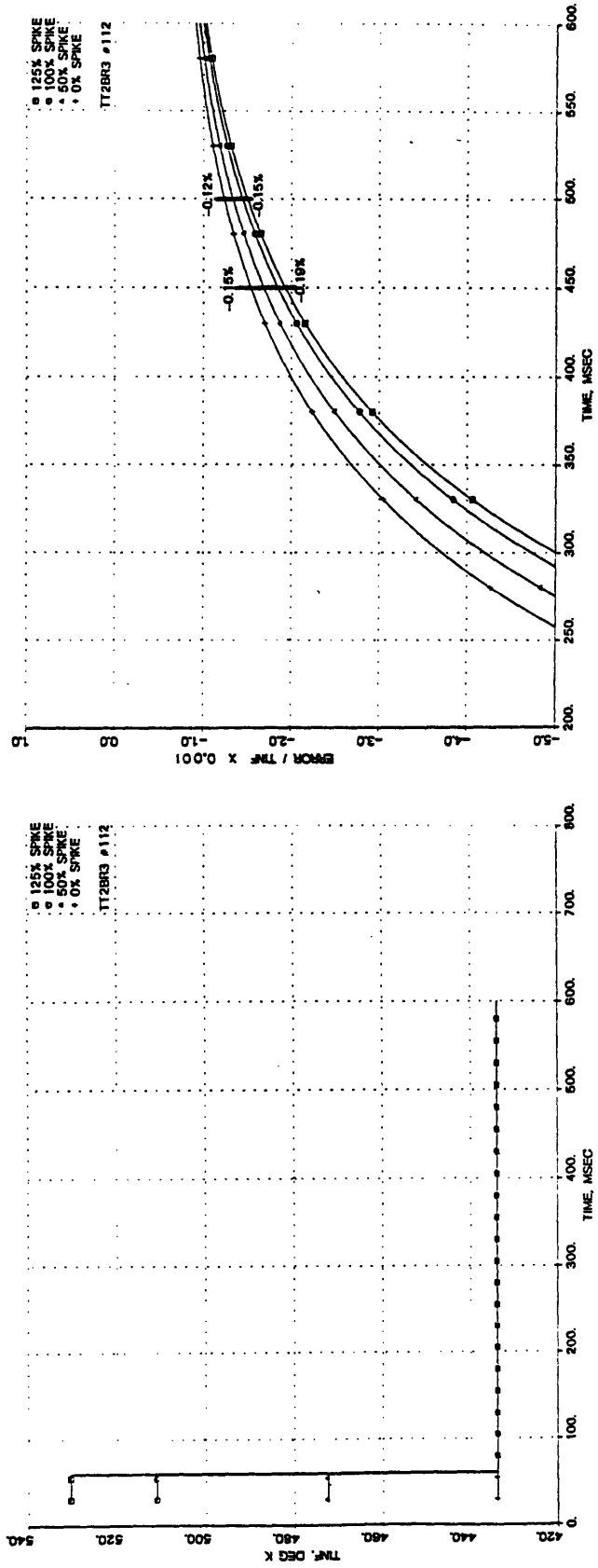

Figure 3.22 - Inputs (a) and responses (b) predicted by the temperature probe model for upstream sensor #3 (TEST112).

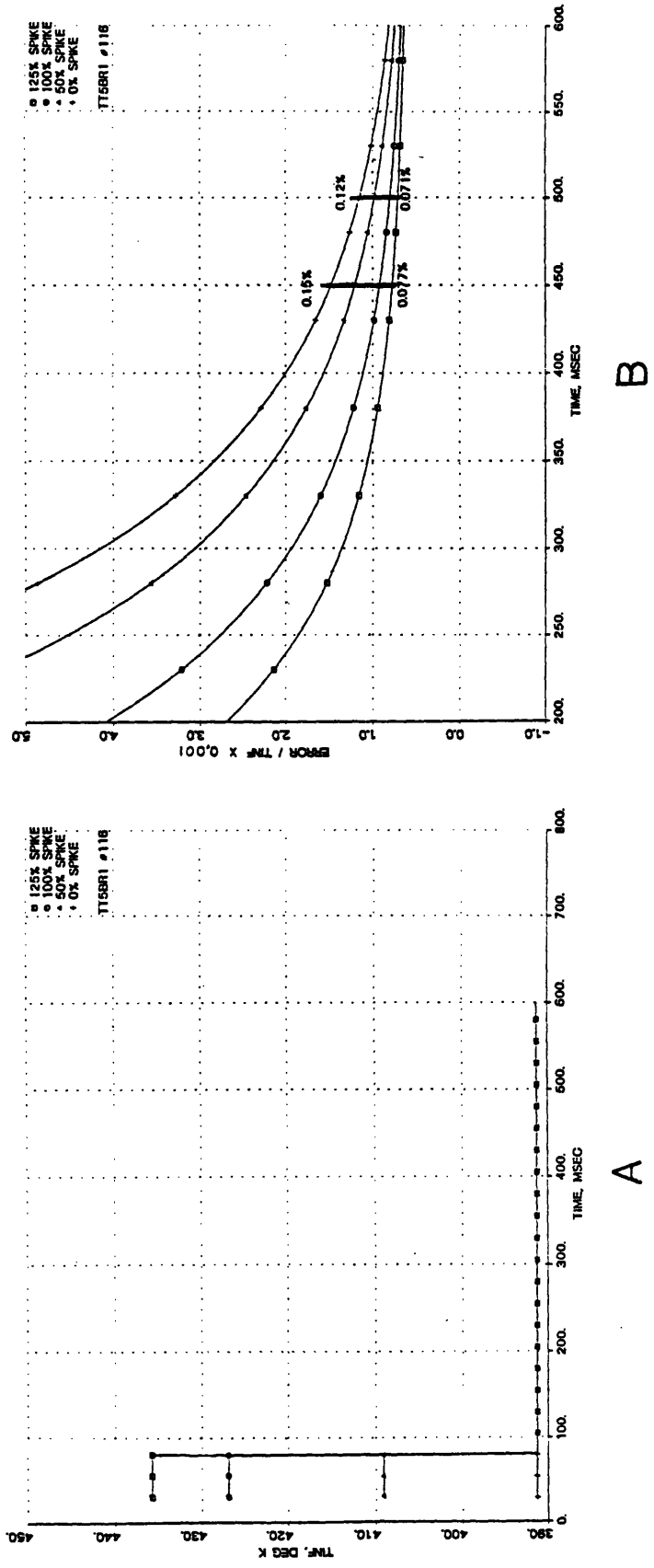

Figure 3.23 - Inputs (a) and responses (b) predicted by the temperature probe model for downstream sensor #1 (TEST116).

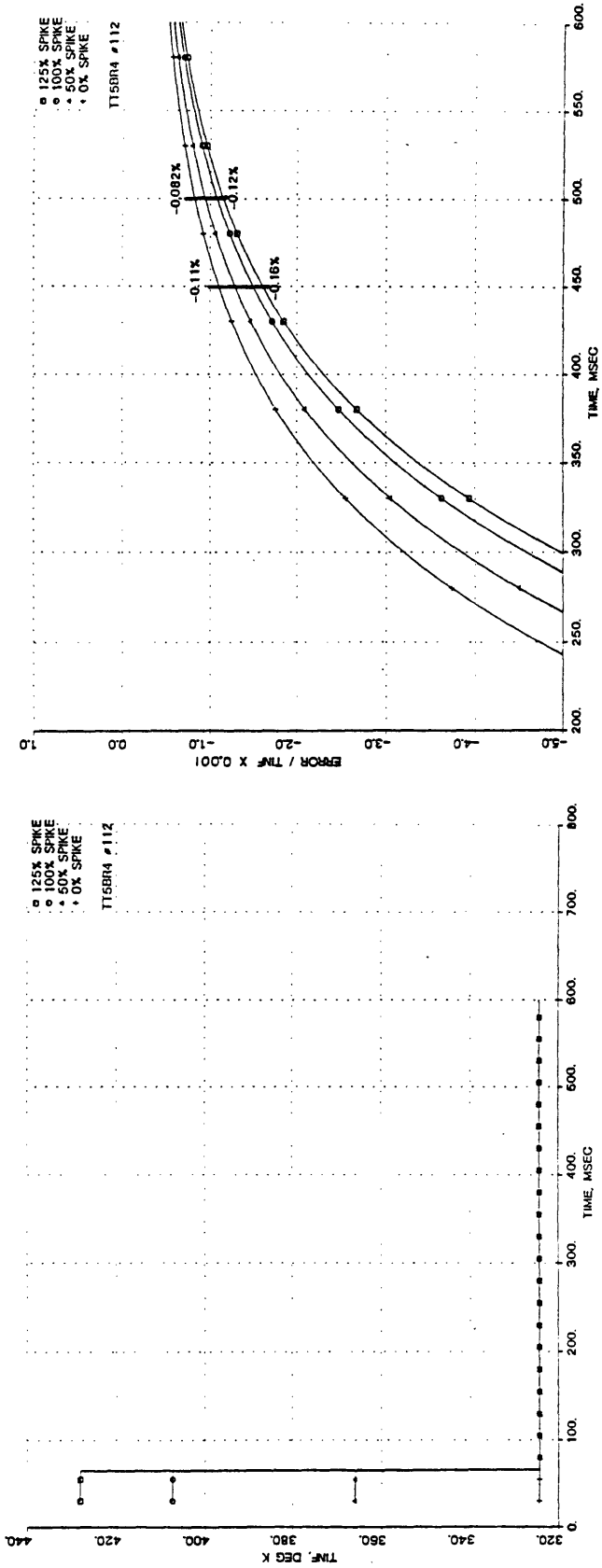

Figure 3.24 - Inputs (a) and responses (b) predicted by the temperature probe model for downstream sensor #4 (TEST112).

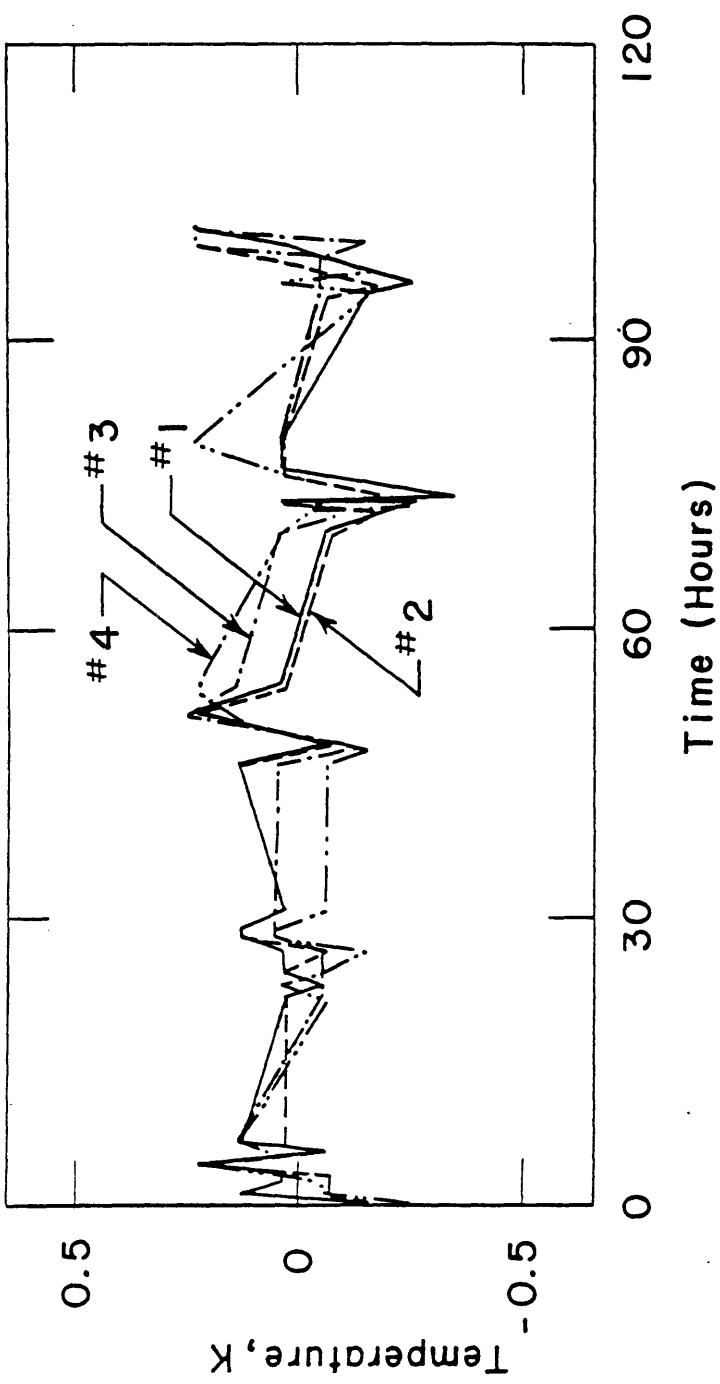

Figure 3.25 - Short term stability test results. The four designs were stable to within +/- 0.25 K in an uncontrolled environment.

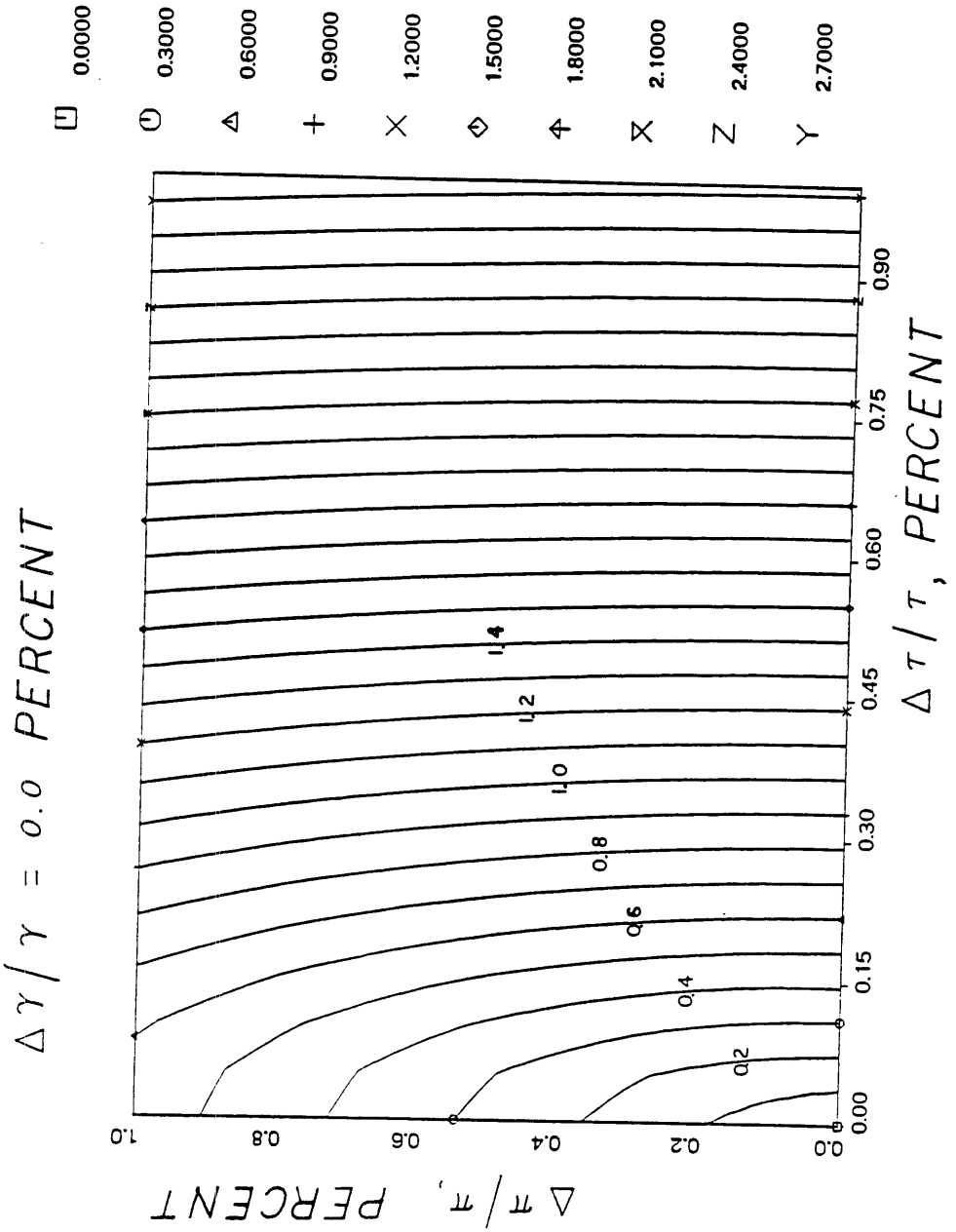

Figure 4.1 - Efficiency contours for zero uncertainty in γ.

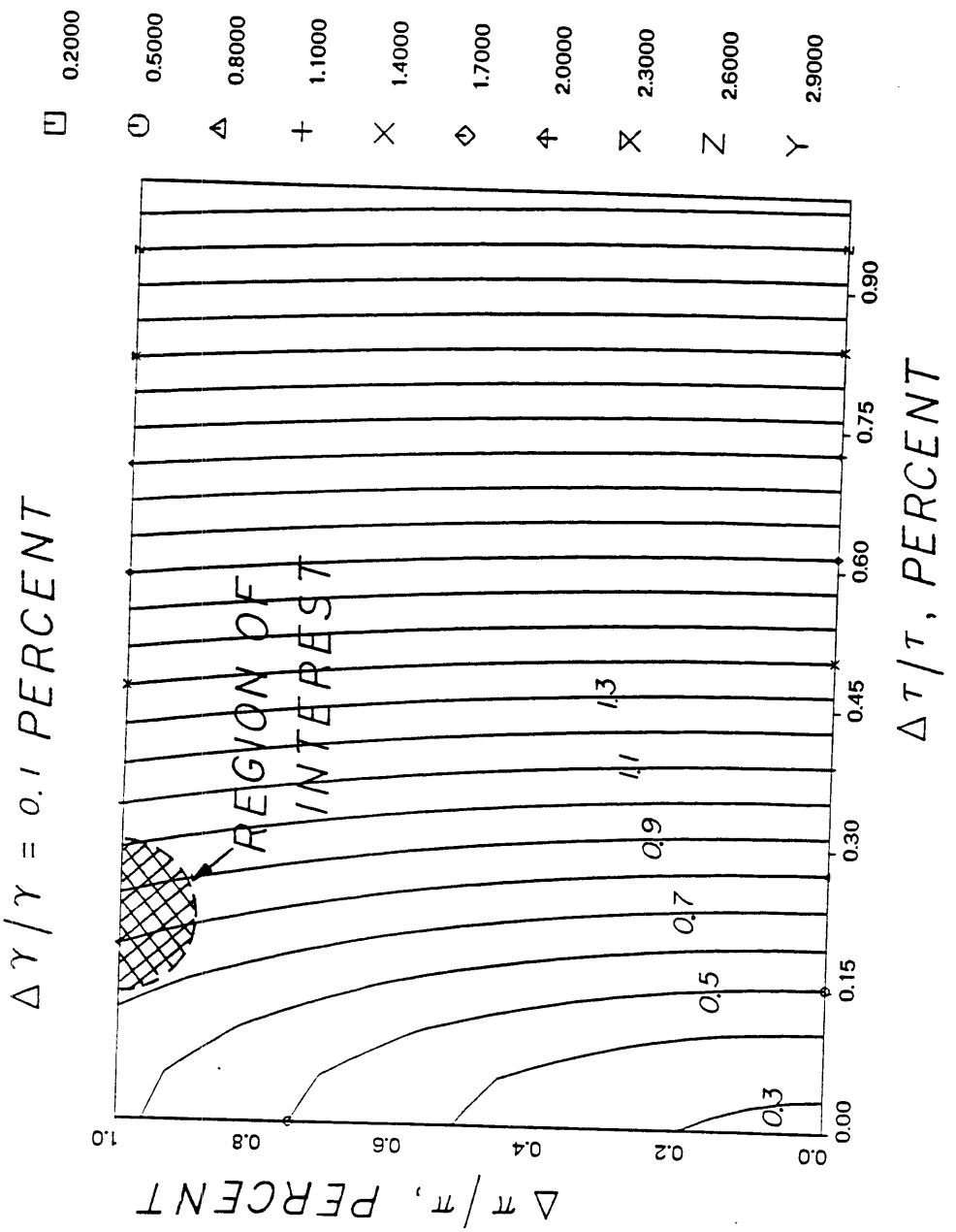

Figure 4.2 - Efficiency contours for 0.1% uncertainty in γ.

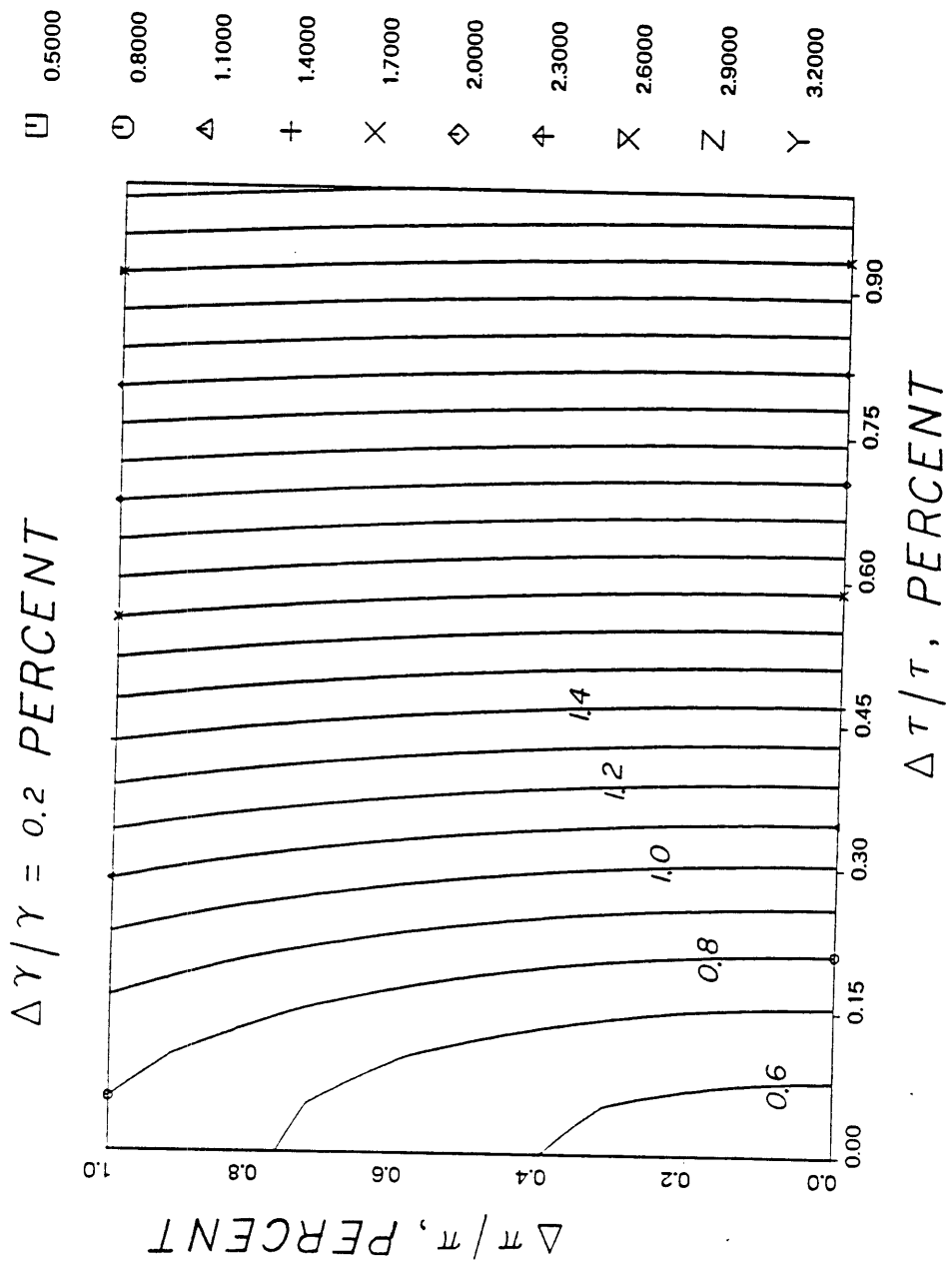

Figure 4.3 - Efficiency contours for 0.2% uncertainty in γ.

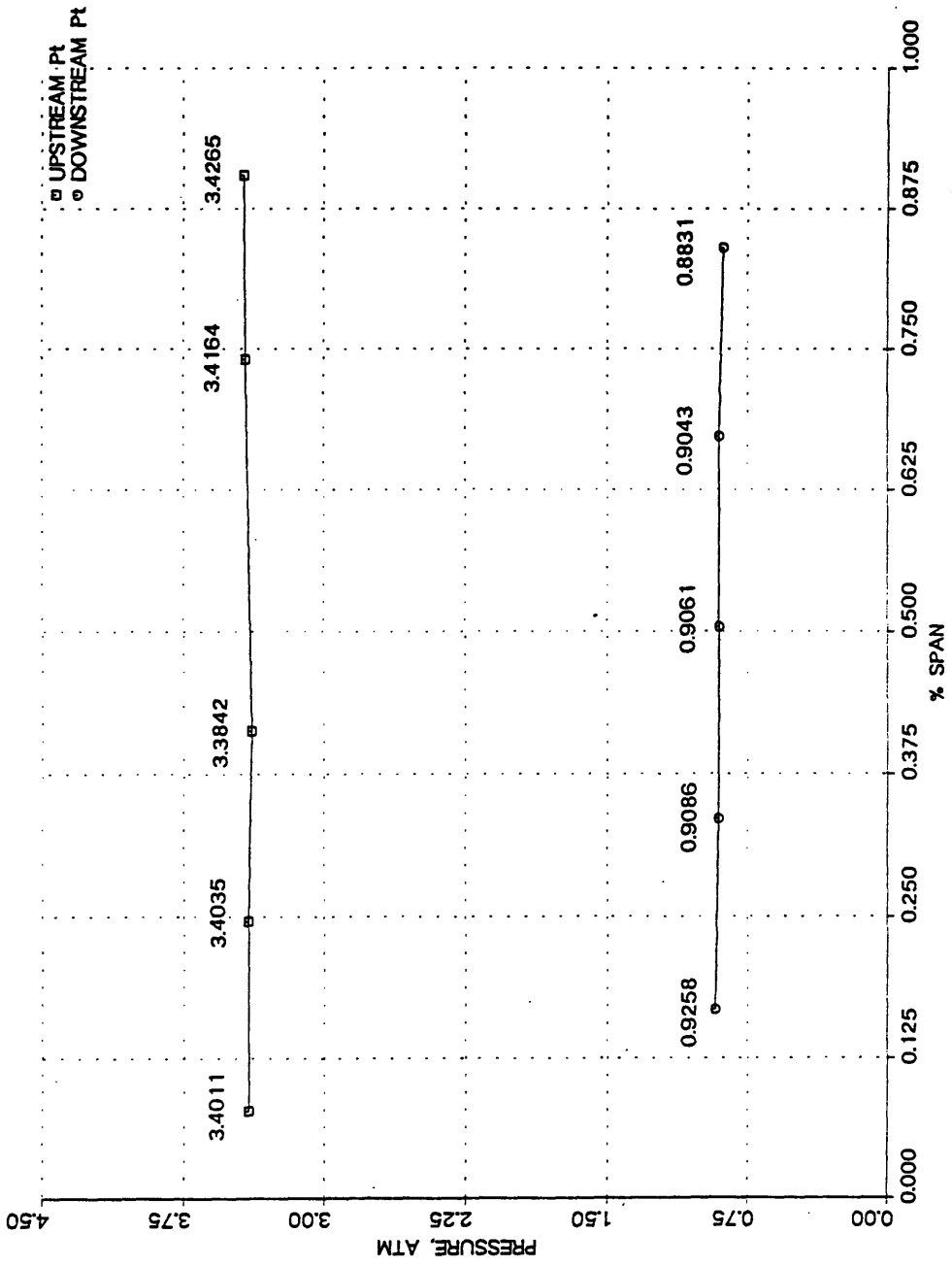

Figure 5.1 - Upstream and downstream total pressure profiles for TEST110.

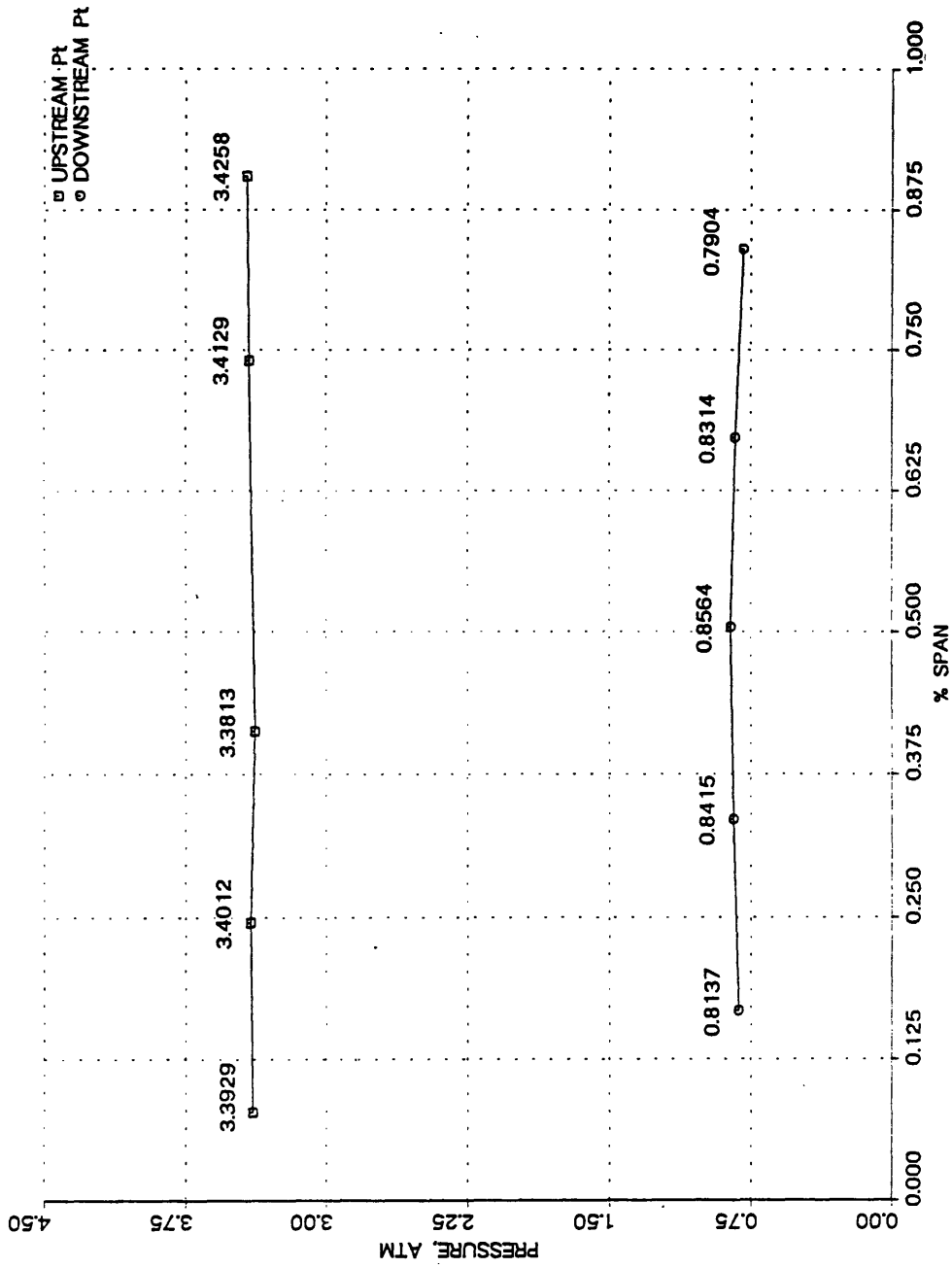

Figure 5.2 – Upstream and downstream total pressure profiles for TEST111.

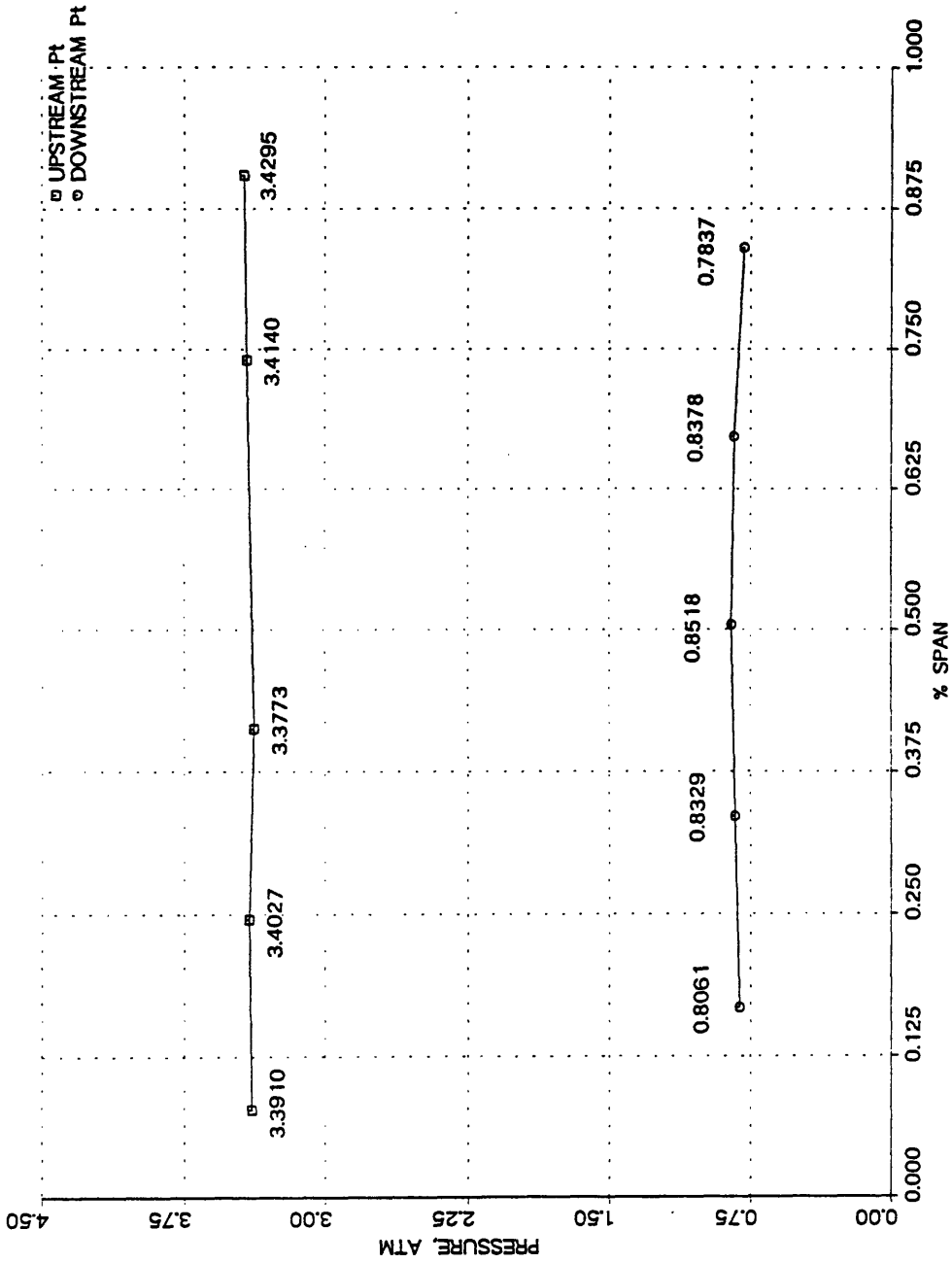

Figure 5.3 - Upstream and downstream total pressure profiles for TEST112.

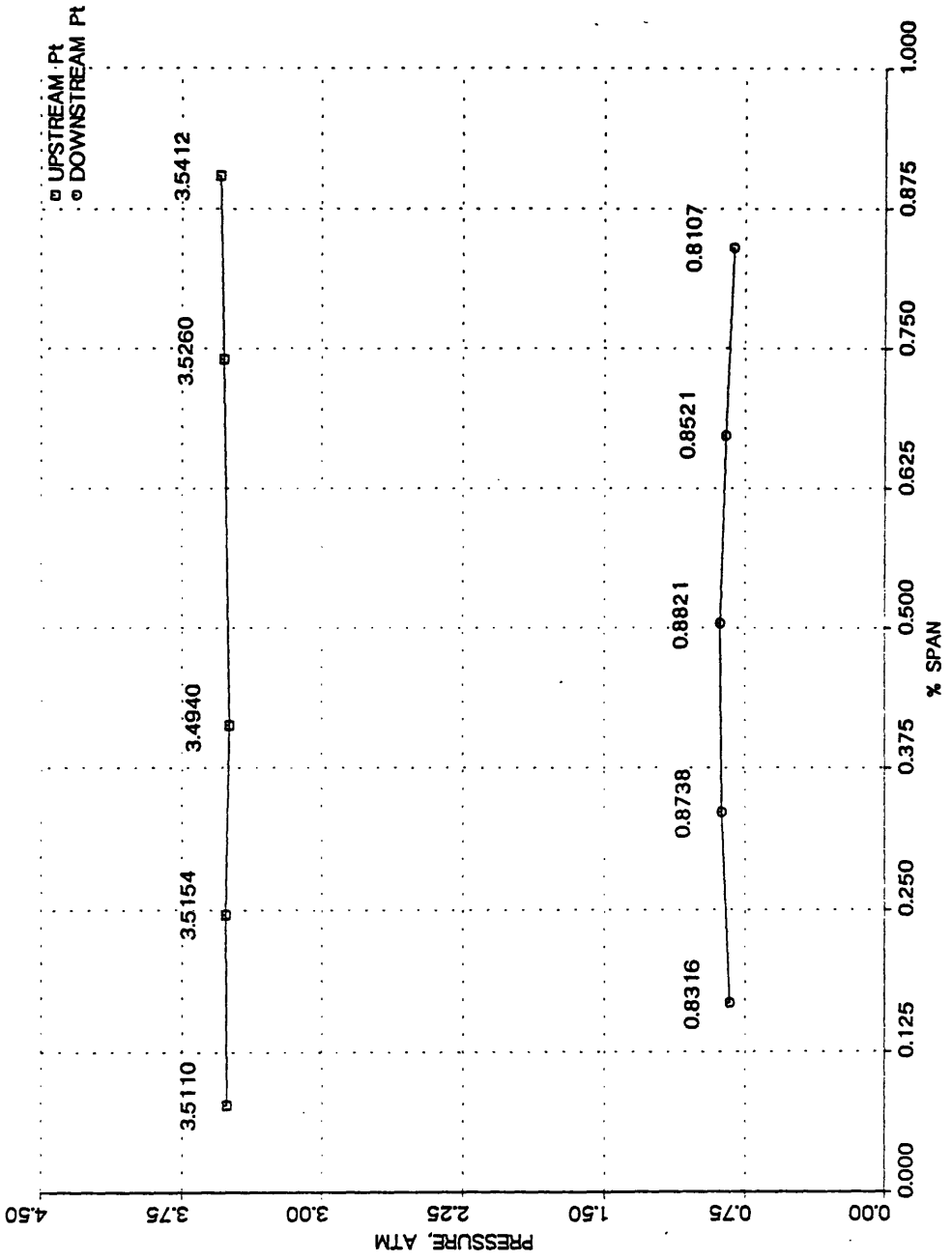

Figure 5.4 - Upstream and downstream total pressure profiles for TEST113.

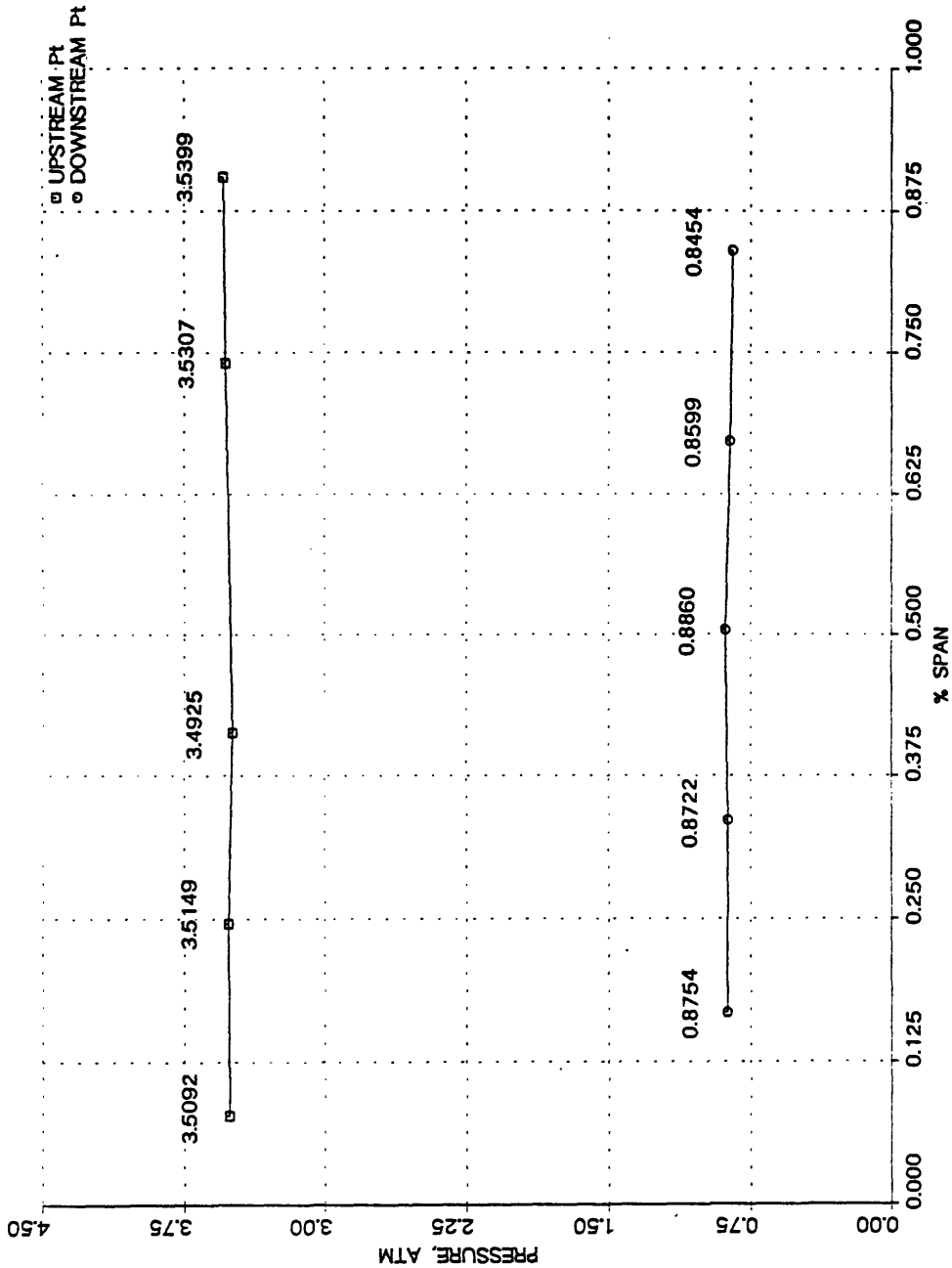

Figure 5.5 - Upstream and downstream total pressure profiles for TEST114.

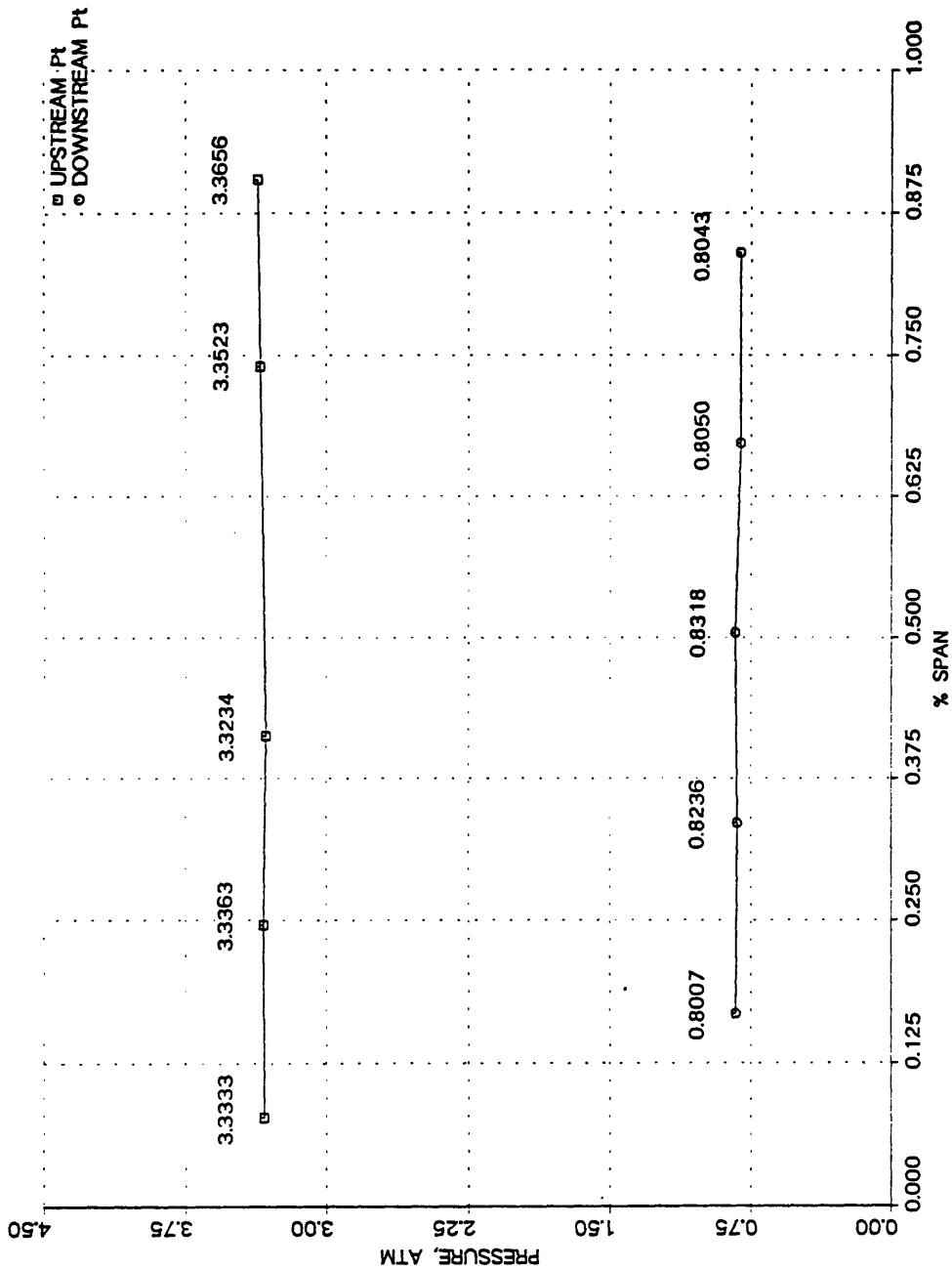

Figure 5.6 - Upstream and downstream total pressure profiles for TEST115.

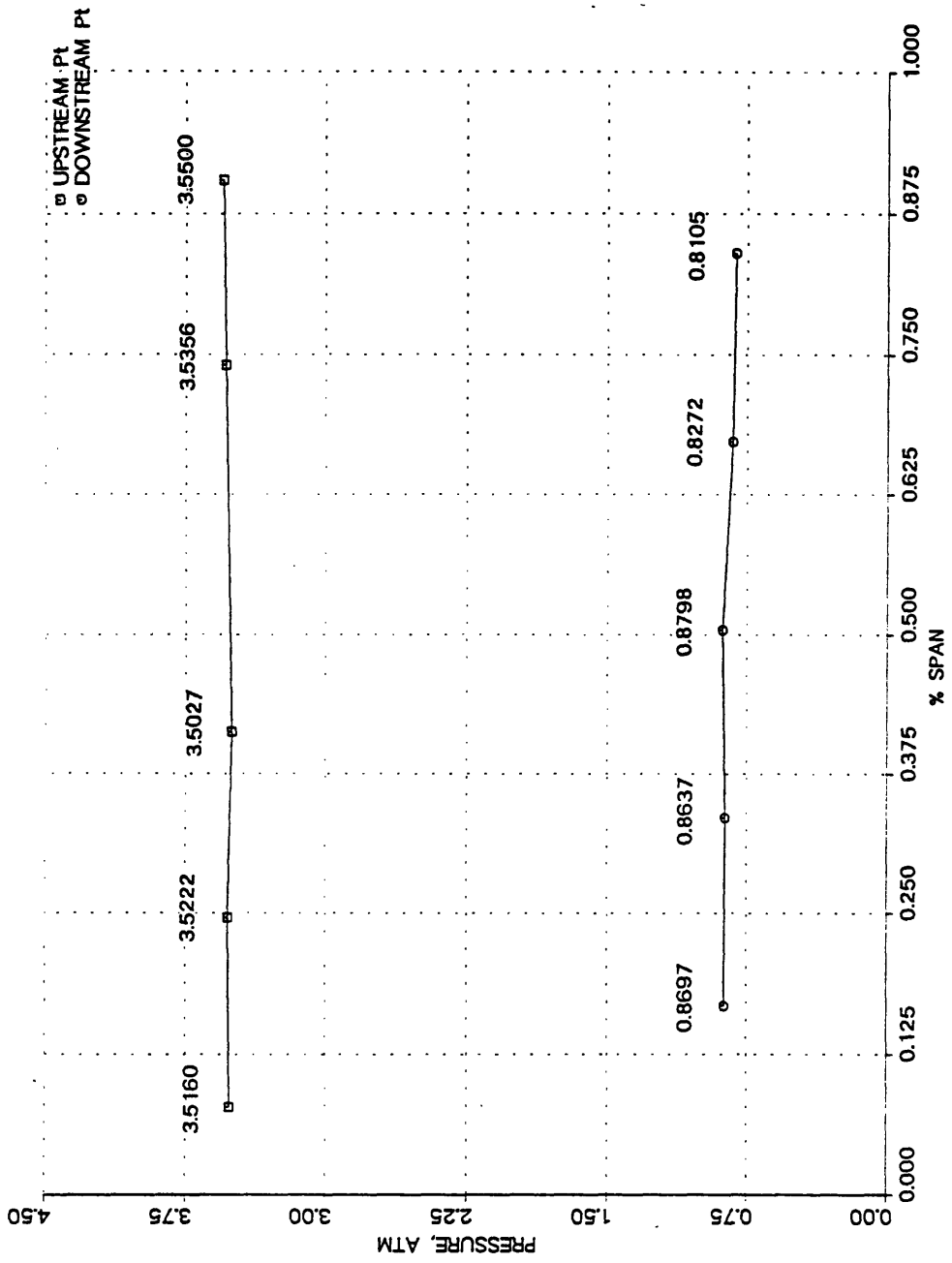

Figure 5.7 - Upstream and downstream total pressure profiles for TEST116.

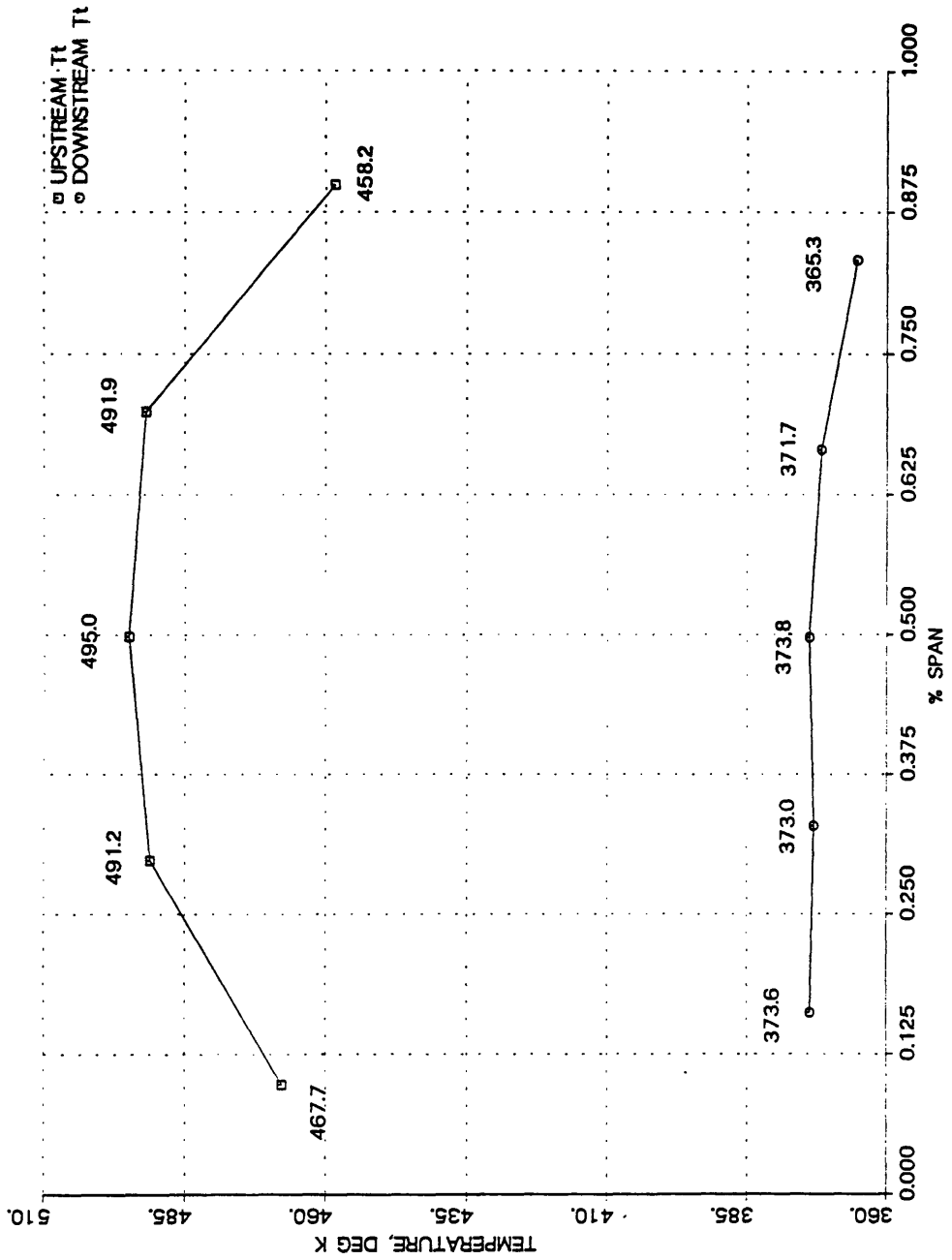

Figure 5.8 - Upstream and downstream total temperature profiles for TEST110.

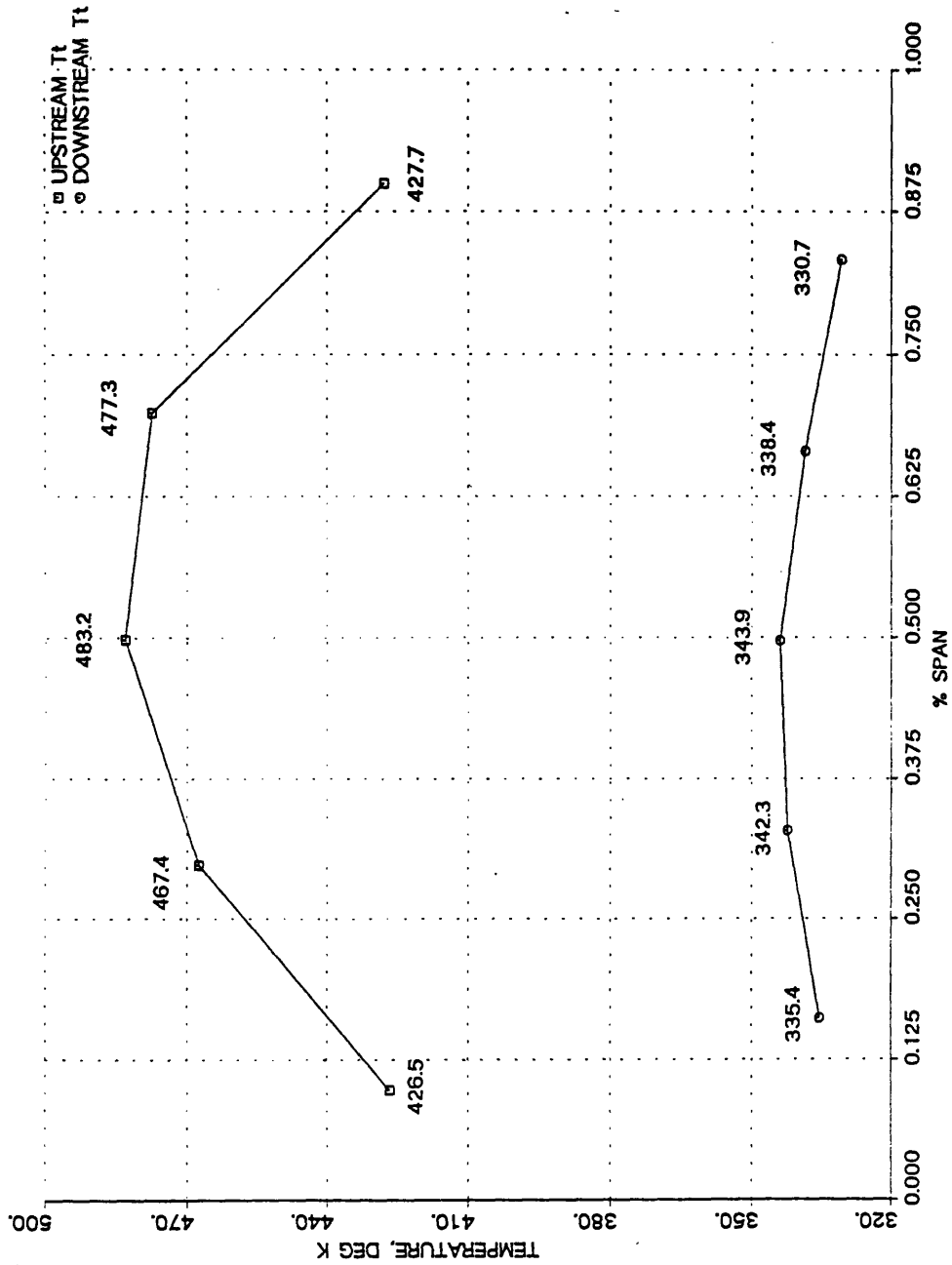

Figure 5.9 - Upstream and downstream total temperature profiles for TESTlll.

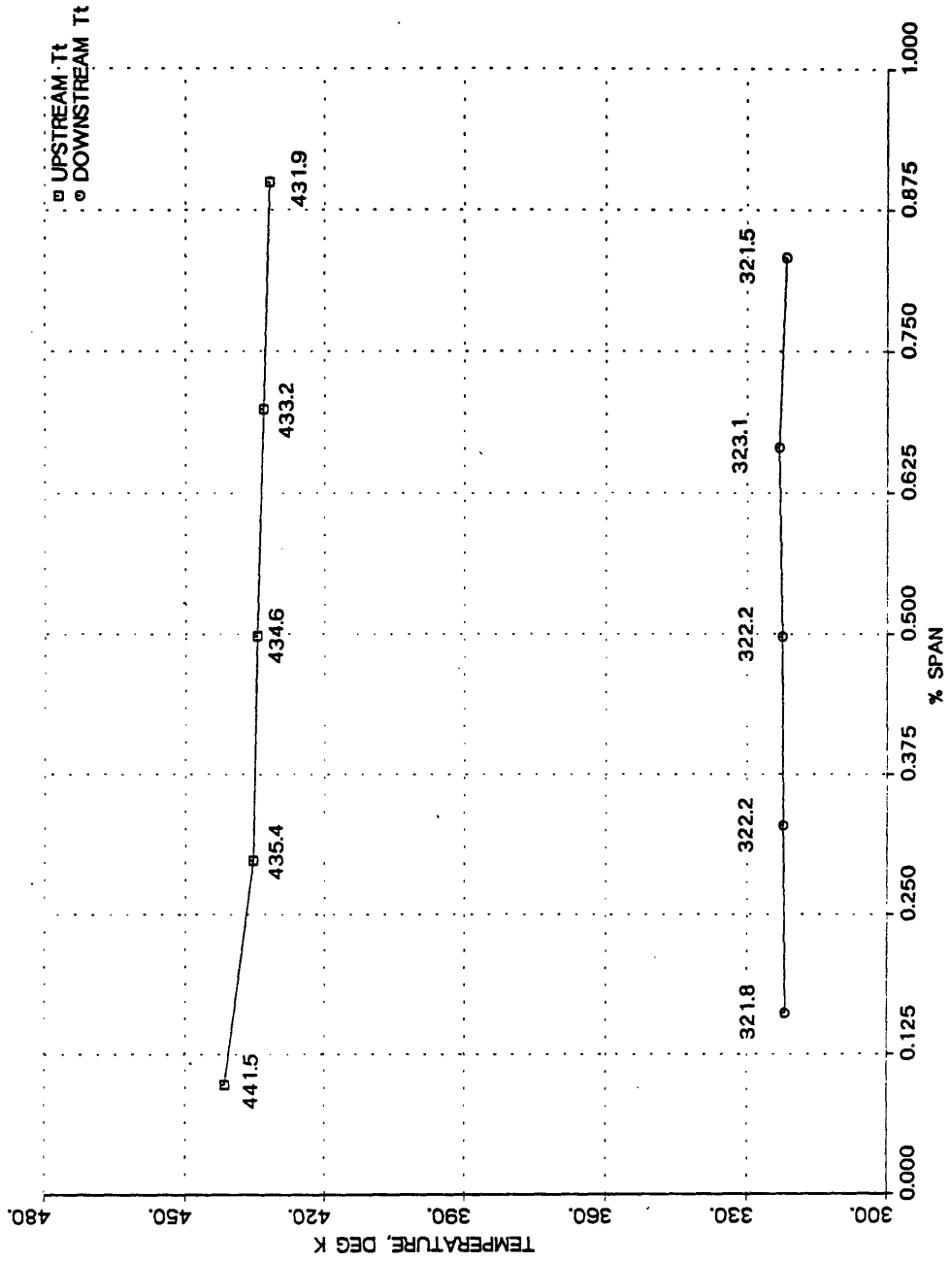

Figure 5.10 - Upstream and downstream total temperature profiles for TEST112.

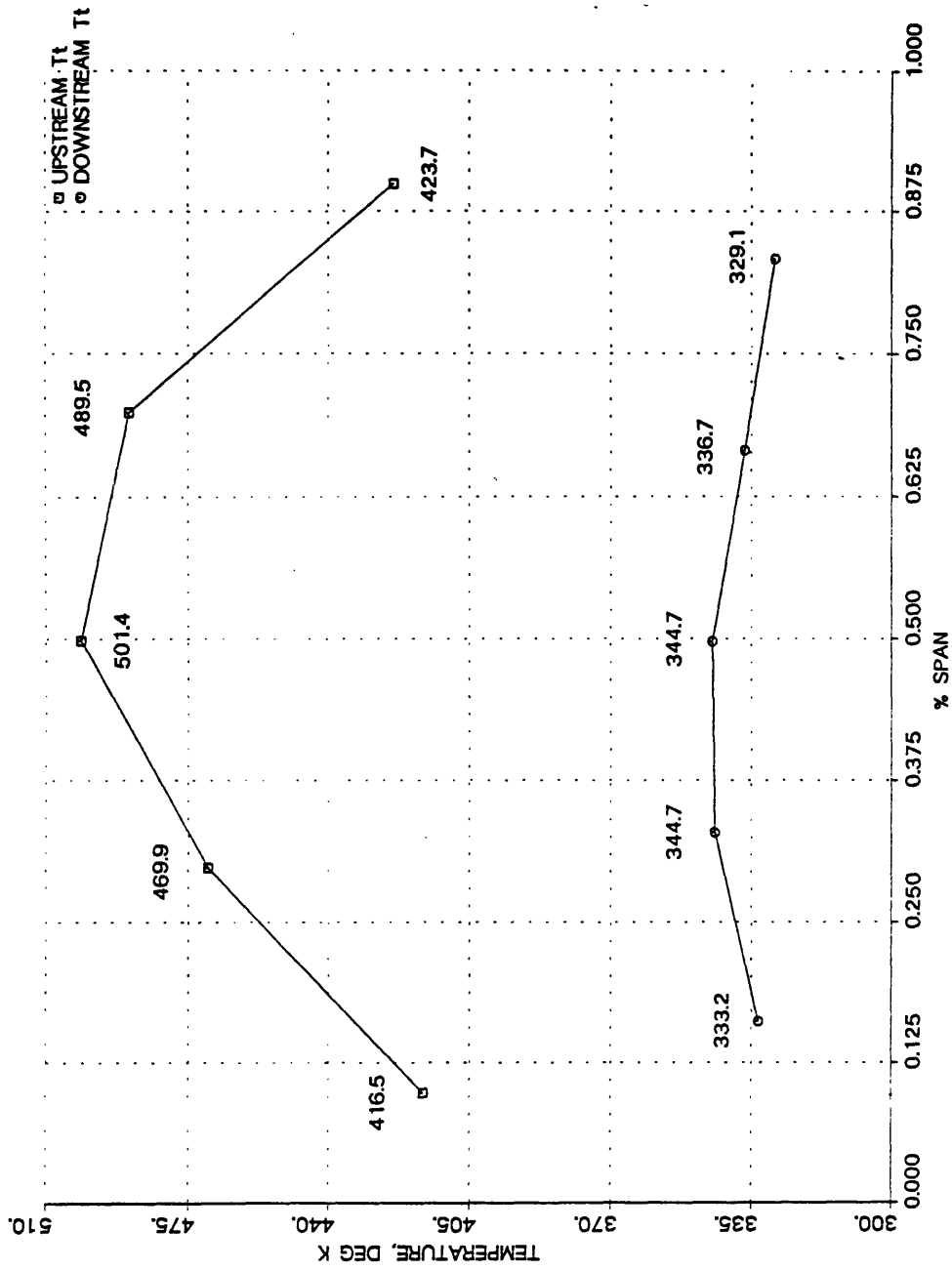

Figure 5.11 - Upstream and downstream total temperature profiles for TEST113.

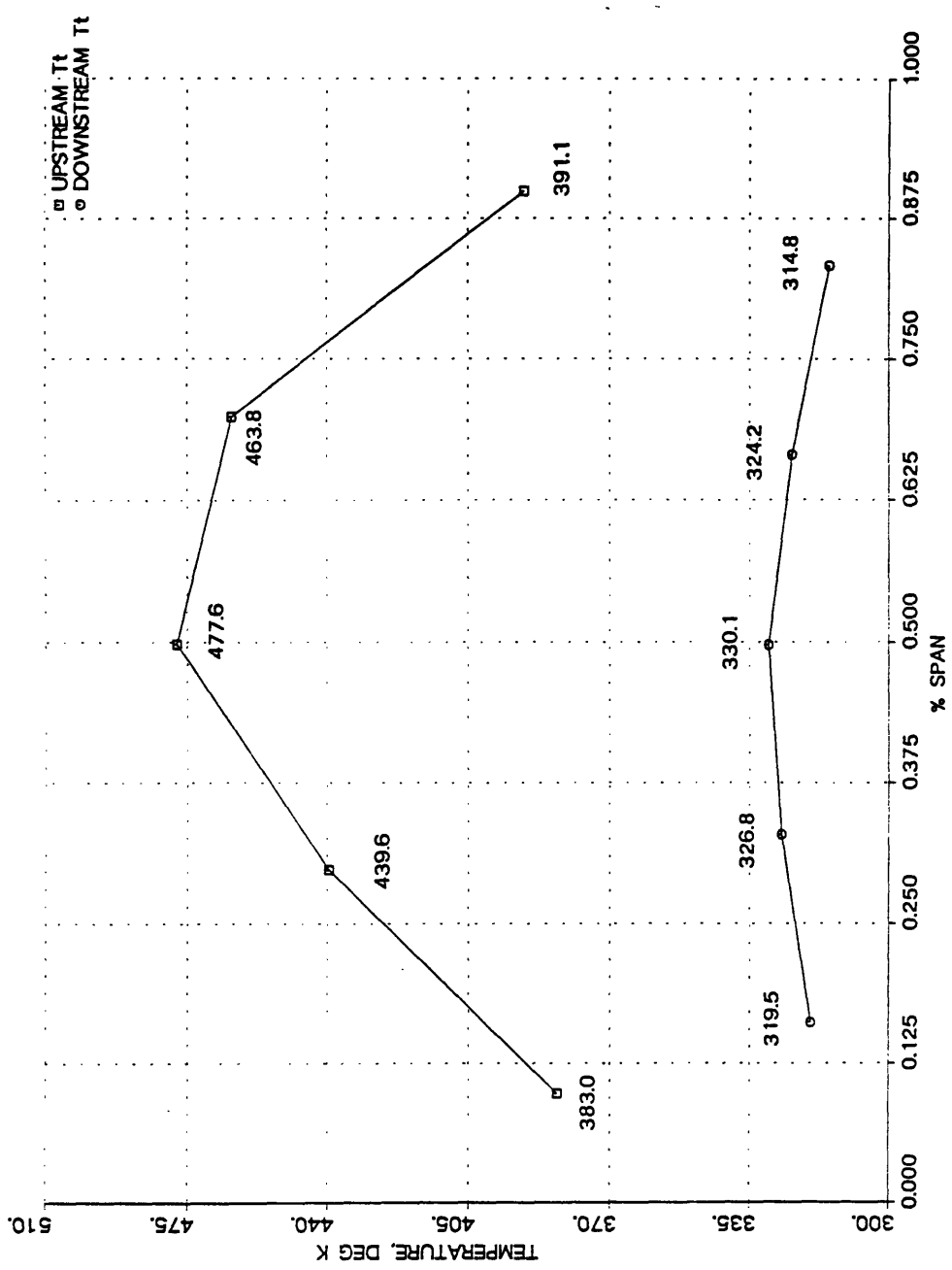

Figure 5.12 - Upstream and downstream total temperature profiles for TEST114.

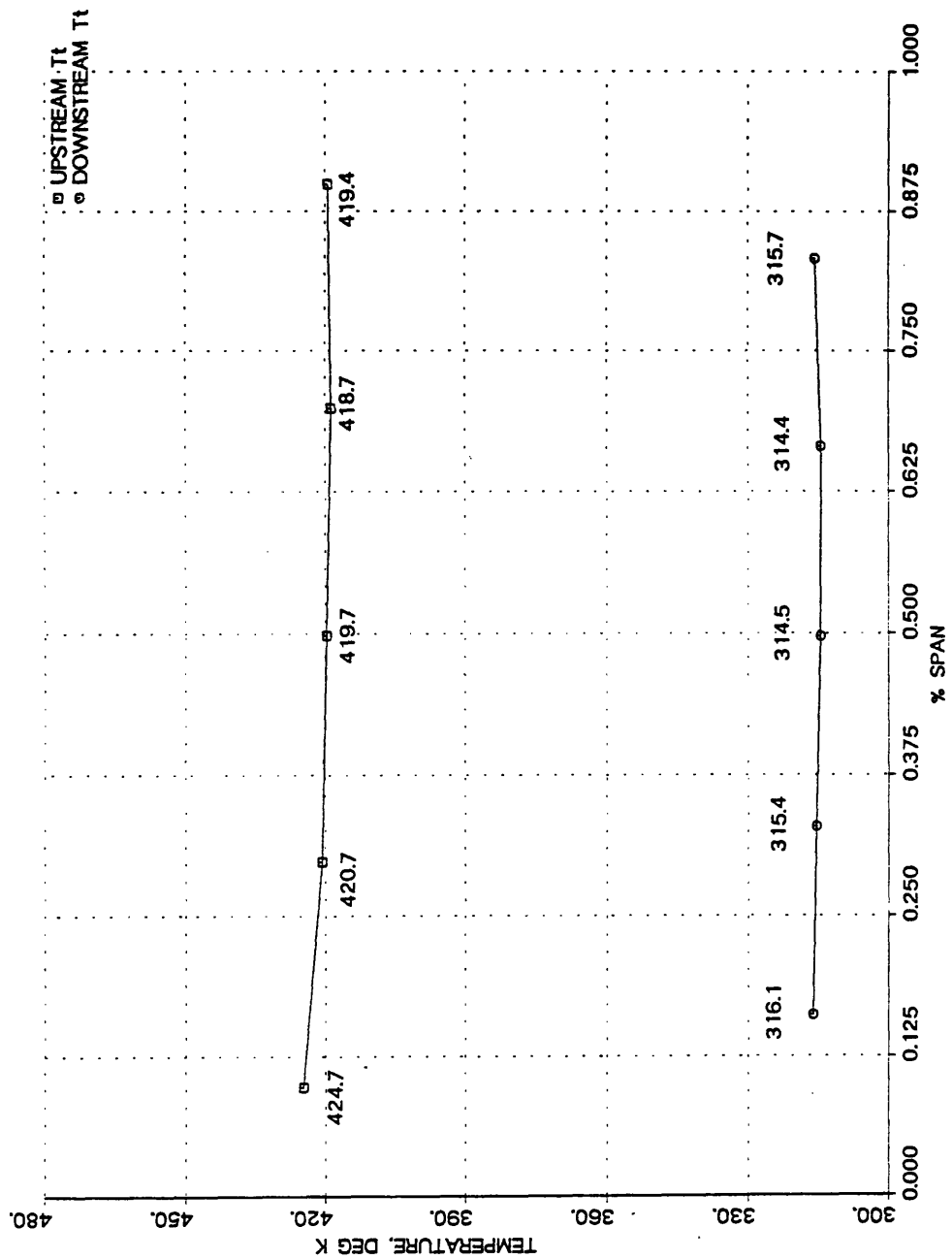

Figure 5.13 - Upstream and downstream total temperature profiles for TEST116.

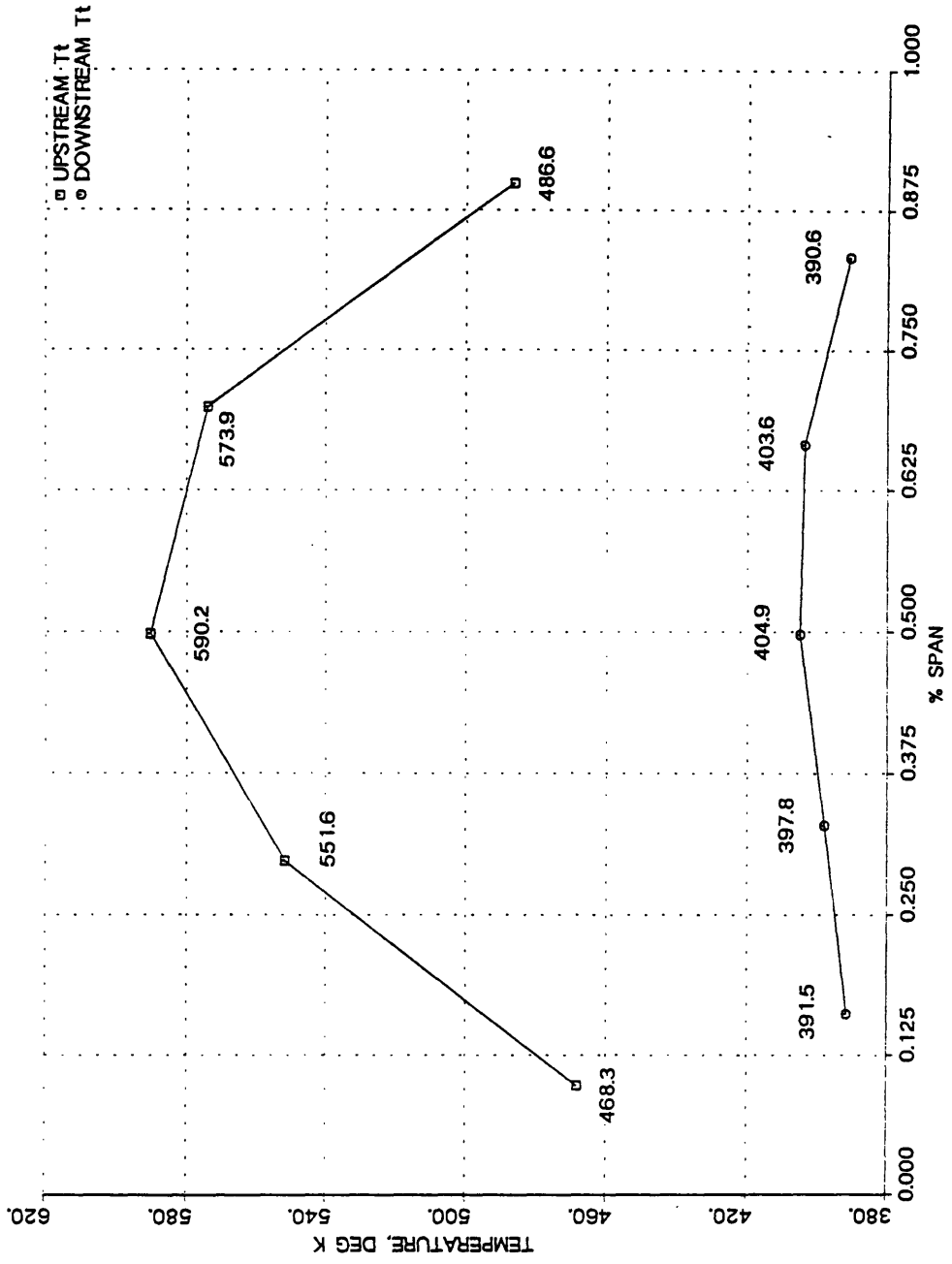

Figure 5.14 - Upstream and downstream total temperature profiles for TEST116.

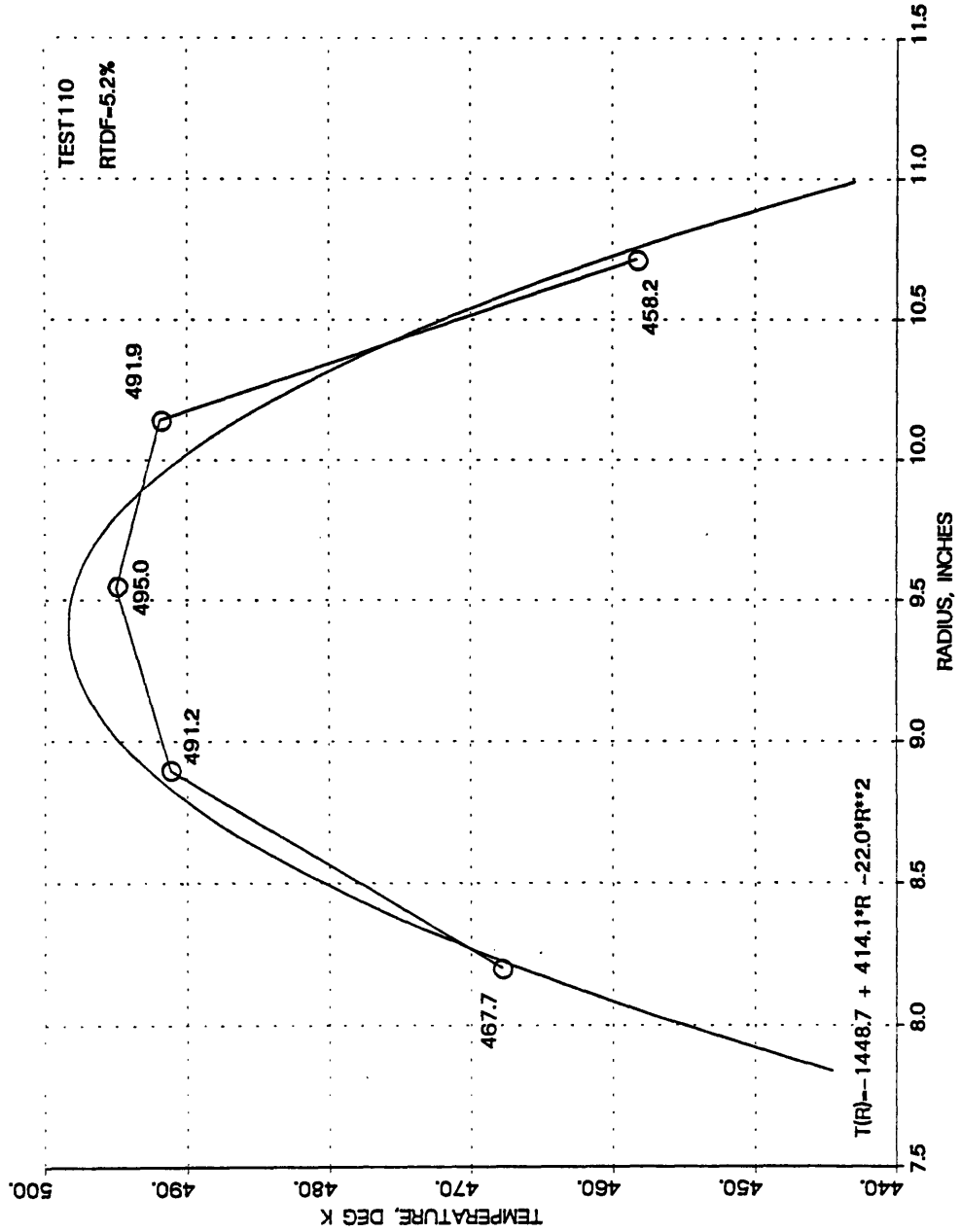

Figure 5.15 - Least Squares parabolic fit to the upstream temperature profile for TEST110

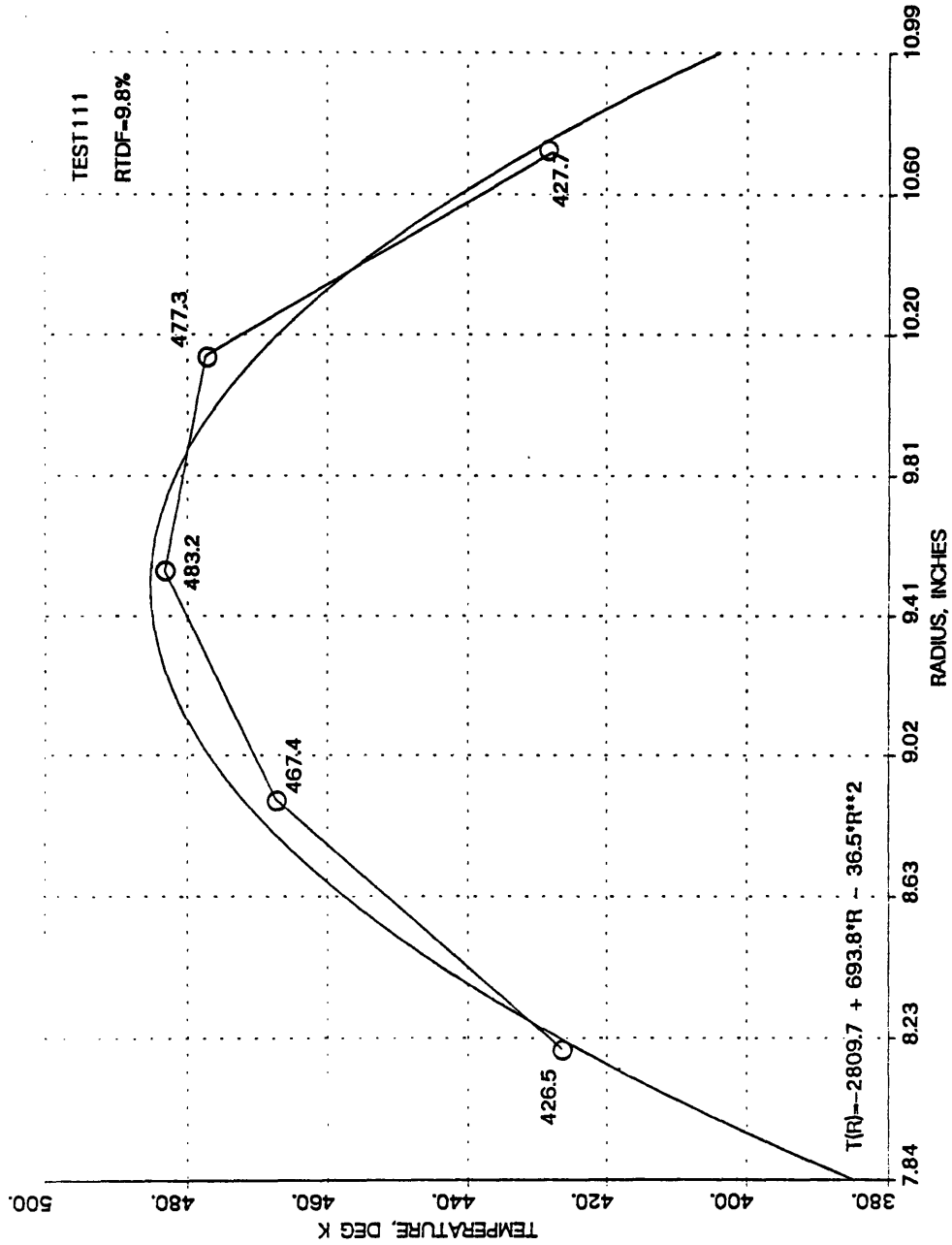

Figure 5.16 - Least Squares parabolic fit to the upstream temperature profile for TEST111

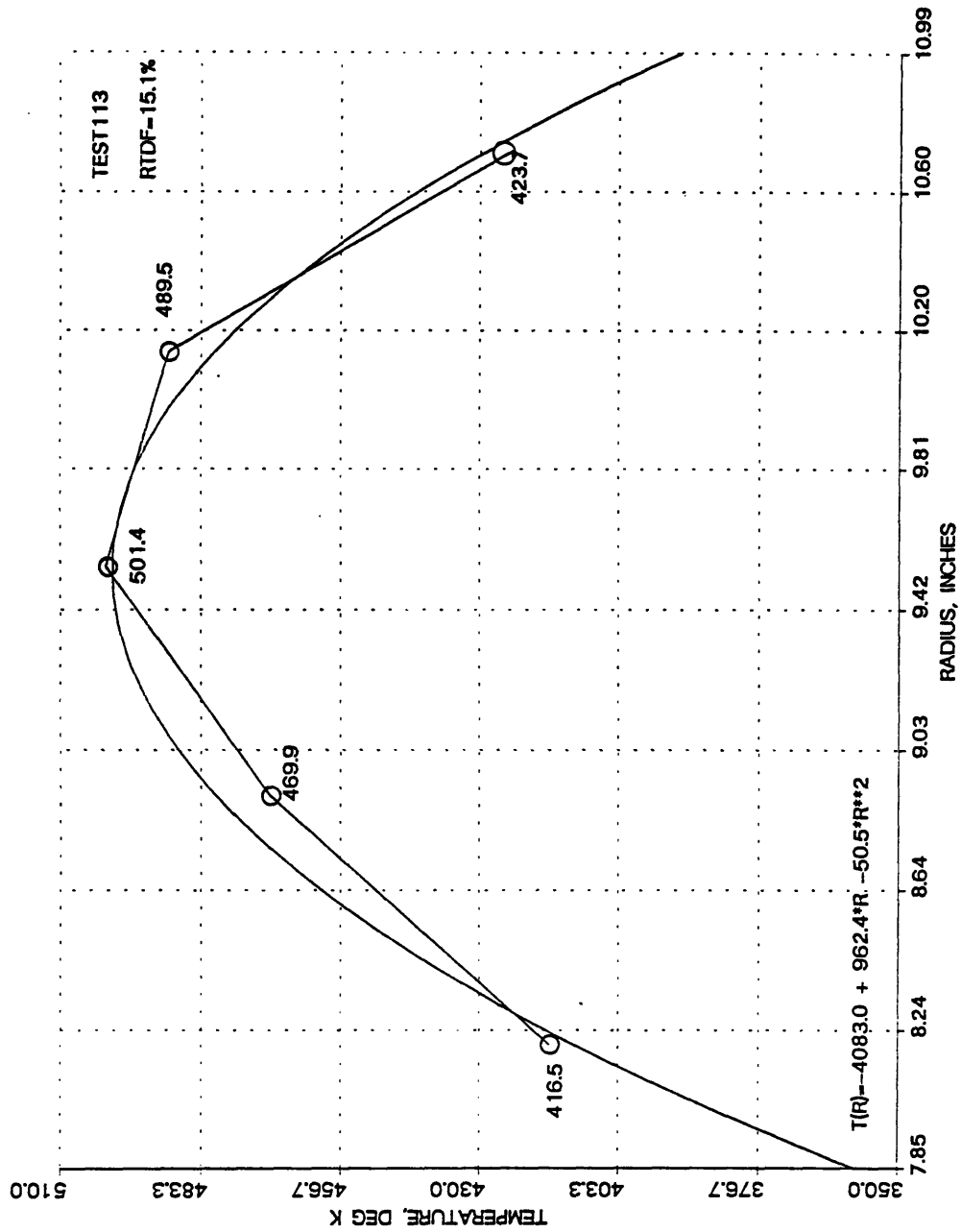

Figure 5.17 - Least Squares parabolic fit to the upstream temperature profile for TEST113

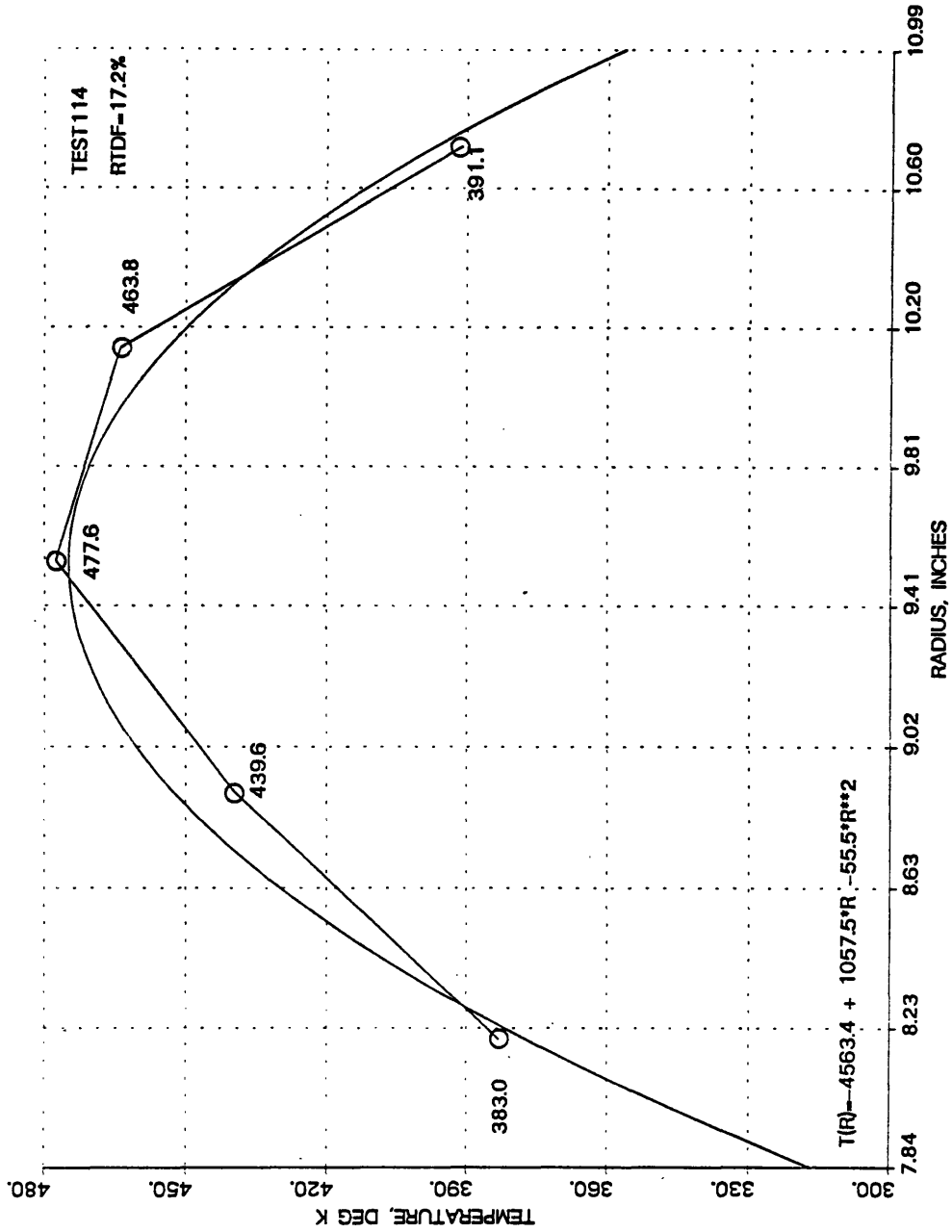

Figure 5.18 - Least Squares parabolic fit to the upstream temperature profile for TEST114

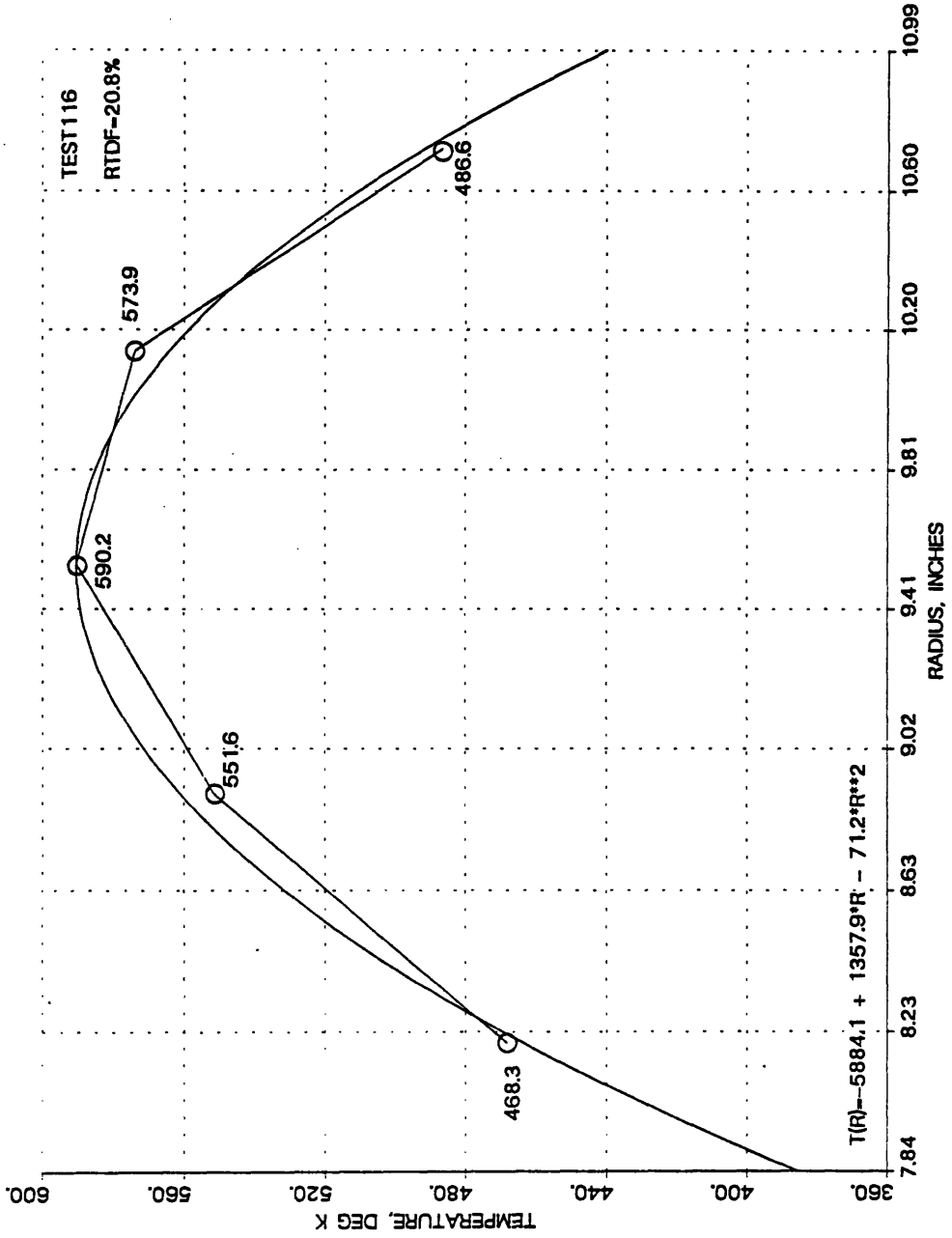

Figure 5.19 - Least Squares parabolic fit to the upstream temperature profile for TEST116

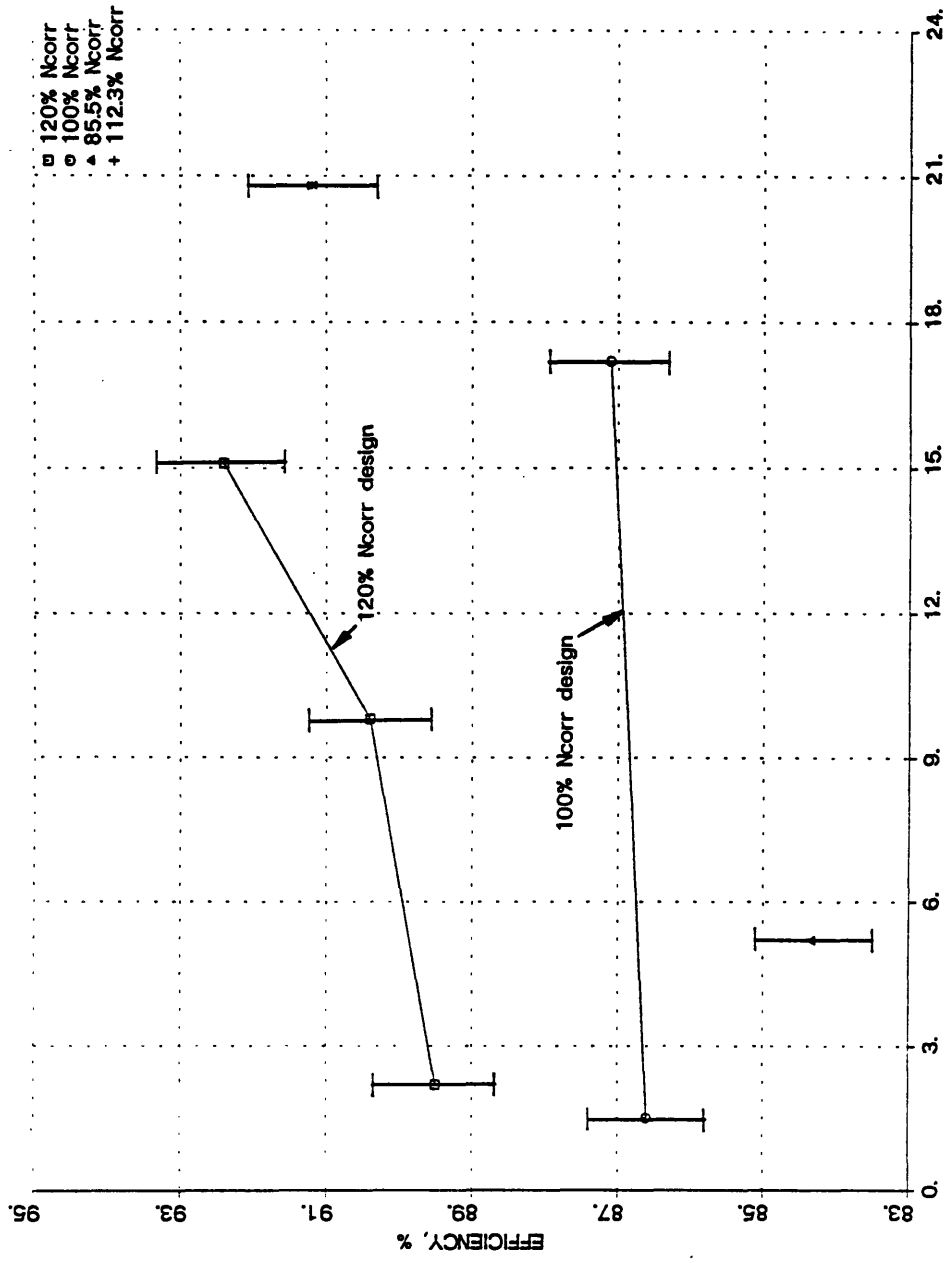

Figure 5.20 - The effect of the inlet temperature profile level (RTDF) on the stage efficiency for fixed corrected speed.

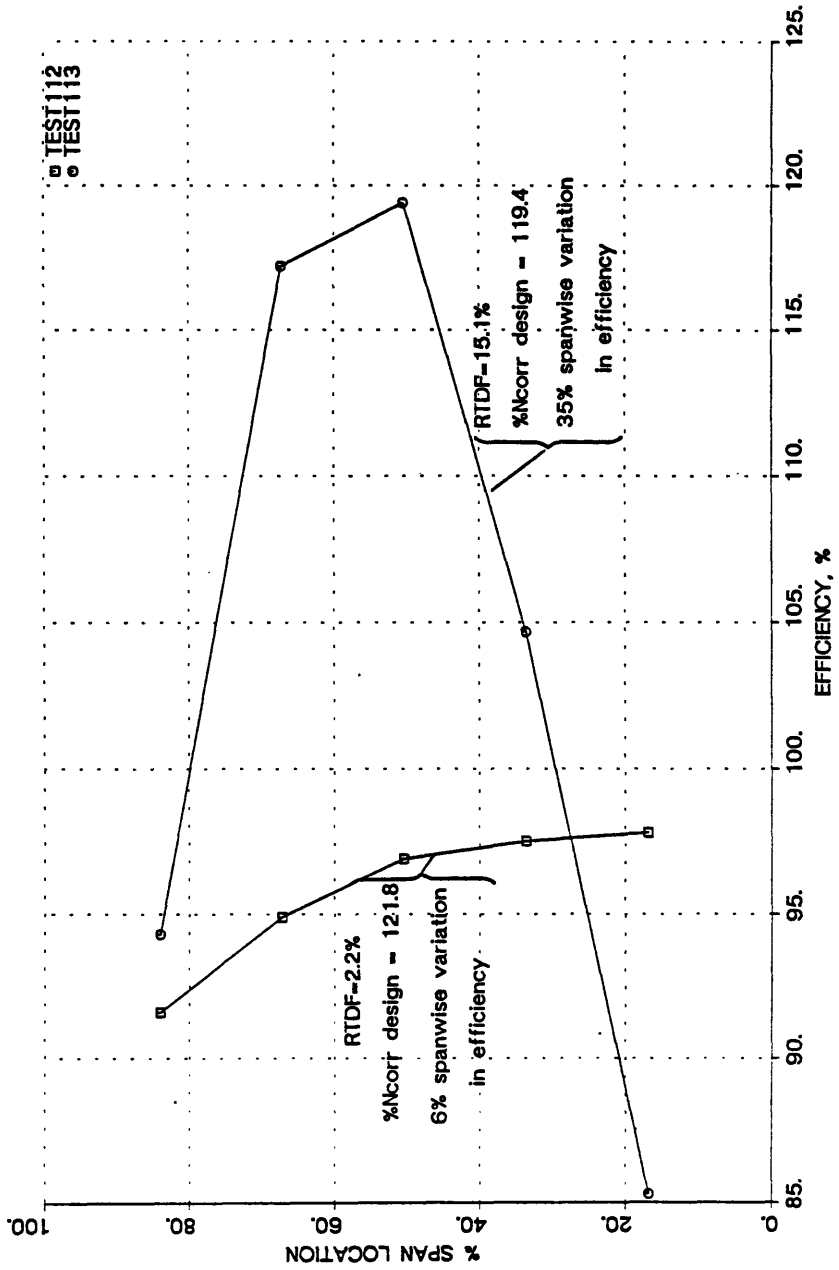

Figure 5.21 - Efficiency vs. % span location for two identical tests with different inlet temperature profiles.

References

1. Epstein, A.H., "Short Duration Testing For Turbomachinery Research and Development", 1988.

2. Epstein, A.H., Guenette, G.R., and Norton R.J.G., "The MIT Blowdown Turbine Facility", ASME Paper 84-GT-116, 1984.

3. Holt, J.L., "Time-Resolved Flowfield Measurements in a Turbine Stage", M.S. Thesis, MIT, June 1985.

4. Ng, W.F., Epstein, A.H., "High-Frequency Temperature and Pressure Probe for Unsteady Compressible Flows", Review of Scientific Instruments, Vol. 54, No. 12, December 1983, pp. 1678-1683.

5. Haldeman, C., M.S. Thesis, MIT, December 1988.

6. Rob Norton, Private Communication.

7. Weyer, H., "The Determination of Time-Weighted Pressures in Strongly Fluctuating Flows, Especially in Turbomachines", ESRO TT-161, May 1975.

8. Grant, H.P., "Measuring Time-Averaged Stagnation Pressure in Pulsatile Air Flow", ISA 23rd International Instrumentation Symposium, Las Vegas, NV, May 1977.

9. Ower, E., Pankhurst, R.C., "The Measurement of Airflow", Pergamon Press, 1977. pp. 57-61.

10. Doebelin, E.O., " Measurement Systems: Application and Design", McGraw-Hill Inc., 1975, p. 128 and p. 401.

11. Hougen, J.O., Martin, O.R., Walsh, R.A., "Dynamics of Pneumatic Transmission Lines, Control Engineering, p. 114, September, 1963.

12. Cattafesta, L.N., Epstein, A.H., "Gas Temperature Measurement in Short Duration Turbomachinery Test Facilities", AIAA-88-3039, July 1988.

13. Bontrager, P.J., "Development of Thermocouple Type Total Temperature Probes in the Hypersonic Flow Regime", AEDC-TR-69-25, January 1969.

14. Sanders, D.G., "Accuracy of Type K Thermocouple Wire below 500 F: A Statistical Analysis", ISA Transactions, Vol. 13, No. 3, pp. 202-211, 1974.

15. Scadron, M.D., "Time Response Characteristics of Temperature Sensors", SAE Transactions, Paper 158H, April 1960.

16. Haig, L.B., "Thermocouple Probe Design Method", SAE Transactions, Paper 158C, April 1960.

17. Meador, J.D., "Dynamic Testing of Gas Sampling Thermocouples", SAE Transactions, Paper 158G, April 1960.

18. Glawe, G.E., Holanda R., Krause, L.N., "Recovery and Radiation Corrections and Time Constants of Several Sizes of Shielded and Unshielded Thermocouple Probes For Measuring Gas Temperature", NASA Lewis Research Center, Paper 505-04, September 1977.

19. Caldwell, F.R., Olsen, L.O., Freeze P.D., "Intercomparison of Thermocouple Response Data", SAE Transactions, Paper 158F, April 1960.

20. Wormser, A.F., "Experimental Determination of Thermocouple Time Constants With Use of a Variable Turbulence, Variable Density Wind Tunnel, and the Analytical Evaluation of Conduction, Radiation, and Other Secondary Effects", SAE Transactions, Paper 158D, April 1960.

21. Paul Beckman Co., Elkins Park, PA.

22. Incropera, F.P., DeWitt, D.P., "Fundamentals of Heat and Mass Transfer", Wiley & Sons, New York, NY, 2nd edition, 1985.

23. "Manual on the Use of Thermocouples in Temperature Measurement", ASTM Special Technical Publication 470B, American Society for Testing and Materials, Philadelphia, PA., 1981.

24. Epstein, A.H., Private Communication.

25. Kline, S.J., McClintock, F.A., "Describing Uncertainties in Single-Sample Experiments, Mechanical Engineering, January 1953.

26. Kline, S.J., "The Purposes of Uncertainty Analysis", Journal of Fluids Engineering, Vol. 107, pp. 153-160, June 1985.

27. Abernathy, R.B., Benedict, R.P., Dowdell, R.B., "ASME Measurement Uncertianty", Journal of Fluids Engineering, Vol. 107, pp. 161-164, June 1985.

28. Smith, R.E., Wehofer, S., "From Measurement Uncertainty to Measurement Communications, Credibility, and Cost Control in Propulsion Ground Test Facilities", Journal

of Fluids Engineering, Vol. 107, pp. 165-172, June 1985.

29. Moffat, R.J., "Using Uncertainty Analysis in the Planning of an Experiment", Journal of Fluids Engineering, Vol. 107, pp. 173-178, June 1985.

30. Lassahn, G.D., "Uncertainty Definition", Journal of Fluids Engineering, Vol. 107, June 1985.

31. Moffat, R.J., "Contributions to the Theory of Single-Sample Uncertainty Analysis", Transactions of the ASME, Vol. 104, pp. 250-260, June 1982.

32. Kerrebrock, J.L., "Aircraft Engines and Gas Turbines", The MIT Press, Cambridge, MA, 1977.

33. Butler, T.L., Sharma, O.P., Joslyn, H.D., Dring, R.P., "Redistribution of an Inlet Temperature Distortion in an Axial Flow Turbine Stage", AIAA-86-1468, June 1986.

34. Schwab, J.R., Stabe, R.G., Whitney, W.J., "Analytical and Experimental Study of Flow Through an Axial Turbine Stage With a Nonuniform Inlet Radial Temperature Profile", AIAA-83-1175 or NASA Technical Memorandum 83431, June 1983.

35. Kerrebrock, J.L., and Mikolajczak, A.A., "Intra-Stator Transport of Rotor Wakes and Its Effect on Compressor Performance", ASME Journal of Engineering for Power, Vol. 92., pp. 359-368, October 1970.

36. Epstein, A.H., Guenette, G.R., Norton, R.J.G., Yuzhang, Cao, "Time Resolved Measurements of a Turbine Rotor Stationary Tip Casing Pressure & Heat Transfer Field", AIAA-85-1220, July, 1985.